Remote Dynamic Triggering across Canada and Hydraulic Fracturing-Induced Seismicity in British Columbia

A dissertation presented
by

Bei Wang

to
The Department of Earth and Planetary Sciences
in partial fulfillment of the requirements
for the degree of
Doctor of Philosophy
in the subject of

Earth and Planetary Science

McGill University
Montréal, Quebec

May, 2019

Author
Bei Wang

Remote Dynamic Triggering across Canada and Hydraulic Fracturing-Induced Seismicity in British Columbia

Abstract

This work investigates the characteristics of dynamically triggered earthquakes across Canada by teleseismic events and seismicity induced by fluid injection in the Montney Basin, northeastern British Columbia.

We first look for dynamic triggering of earthquakes through the Natural Resources Canada catalog (NRCan) across Canada following global mainshocks from 2004 to 2014 with surface magnitudes > 6, depths < 100 km. Statistical analysis of the Natural Resources Canada Catalog suggests several regions are capable of dynamic triggering, including Vancouver Island, the border of Yukon and Northwest Territories, western Alberta, western Ontario, and St. Lawrence paleorift system in eastern Canada. Among these regions, much of the observed propensity for triggering occurs near active faults, but in some cases, triggering occurs outside of active seismic zones, such as eastern British Columbia and western Alberta undergoing active oil and gas production, which suggests the propensity for remote dynamic triggering may be correlated with the propensity for locally inducing earthquakes by fluid injection.

Based on the results of the catalog approach, we first look for triggering near injection sites in western Alberta. We find remote triggering associated with three mainshocks using a matched-filter

approach on continuous waveform data. We observe two clear directly triggered events in the Rayleigh wave train of the 2014/10/14 El Salvador earthquake, but with a relatively small transient stresses compared to previous studies on dynamic triggering (< 1 kPa). The triggering sensitivity to such low strain and stress perturbations suggests pre-existing faults in the study area may be critically stressed，which could be possibly due to the continuous fluid injection. The waveform study of triggered events suggests long-period shaking below 20 s may be more important for triggering than the cumulative shaking or cumulative energy.

Next, we investigate the occurrence of remote dynamic triggering in three unconventional Canadian hydrocarbon regions where recent fluid injection activity is correlated with increasing numbers of earthquakes between 2013 and 2015. These include northeastern British Columbia and western Alberta (BCAB), Northwest Territories (NWT), and New Brunswick (NB), where station coverage has been increased to monitor injection related seismic activity. We use a two-fold approach, 1) search from waveforms directly following teleseismic events to look for evidence of immediate triggering, and 2) use a MMF detection enhanced catalog with statistical analysis to test if dynamic triggering occurs. Results suggest both direct and delayed triggering occur in all three regions.

The occurrence of triggering following transient stress perturbations of < 10 kPa in all the above three regions suggests that local faults may remain critically stressed over periods similar to the time frame of our study (~2 years) or longer, potentially due to high pore pressures maintained in tight shale formations following injection. After investigating the possible physical factors which may influence the triggering, we found 1) the amplitude of low-frequency shaking acts as a dominant factor for dynamic triggering, probably due to the dilatational strain generated from seismic waves

altering pore pressure, flow velocities, and permeability at low frequencies, and 2) a trans-tensional or extensional tectonic regime is not a prerequisite for dynamic triggering as other studies suggest, at least in injection environments. Finally, BCAB also experiences a delayed seismicity increase (up to 10-day) compared to NWT and NB, which only show relatively immediate dynamic triggering. Longer fluid injection history at BCAB suggests that immediate versus delayed seismicity increases from transient stresses may result from stress transfer via the rock matrix and pore pressure perturbations, respectively, and could provide a unifying mechanism that explains both types of triggering.

With the observed dynamic triggering cases at these injection sites, we found that the injected fluid plays an important role in changing stress state of local faults. Meanwhile, the injected fluid could also be one of the most important triggering factors for induced earthquakes. In the following, we first focus on the seismicity in the Montney Basin, northeastern British Columbia, which is closely tied to the Hydraulic Fracturing (HF) activities, to investigate characteristics for the elevated seismic rate after the year 2011. We installed 8 broadband seismic stations in northwest Fort St. John (FSJ) during May 13th to October 7th 2015. On 17 August 2015, a M_w 4.6 earthquake occurred nearby. We detected more than 300 earthquakes between 08/11/2015 and 10/07/2015 proximal to this M_w 4.6 earthquake using a MMF method. Then we estimated their seismic moments, corner frequencies by fitting a Brune spectral model to individual event spectra, and spectral ratios respectively, which are used to estimate stress drop values. The stress drop values range from 0.9 to 33.8 MPa and fall within the typical range observed for tectonic events, and are relatively smaller compared to other stress drop estimates of HF induced earthquakes in the Western Canadian Sedimentary Basin (WCSB). We also find there is a ~5-day delay between HF injection and this M_w

4.6 earthquake, and a small *b*-value of 0.78 for the aftershock sequence. In addition, the M_w 4.6 event falls above the predicted maximum magnitude-maximum injected volume relation of McGarr (2014). All of the above factors suggest that the induced sequence occurred on a pre-existing fault, and the maximum magnitude is controlled by tectonic conditions rather than cumulative injection volume.

Next, we investigate the triggering mechanisms for this M_w 4.6 earthquake by calculating the change of Coulomb failure stress (ΔCFS) on the specific pre-existing receiver fault due to both fracture openings and numerical poroelastic stress changes, with the fault orientation determined from the mainshock focal mechanism solution. The results suggest that pore-fluid pressure diffusion through a hypothetical highly-permeable conduit could be the dominant factor for the triggering when compared to the small elastic stress changes by fracture openings and negative ΔCFS by sole poroelastic stress transfer.

In addition, we focus on the immediate seismic response (1-day) at another two injection sites using the same approaches compared to the ~5-day delay response of the M_w 4.6 earthquake. Positive ΔCFS results do suggest nearby injection activities could alter the stress field and encourage the local earthquakes to occur. In general, the various time scales of the triggering response at different injection sites could be due to 1) the fault's initial stress state, which is related to stress accumulation history and tectonic stress field, and 2) the level of stress perturbations (i.e., the amplitude of ΔCFS generated from nearby earthquakes and HF activities), which is related to the magnitude, hypocentral distance, and orientation of nearby induced earthquakes, the HF activities at nearby injection sites (e.g., cumulative volume of injected fluids), and possible existence of subsurface hydraulic conduits acting as pathways which could accelerate fluid and pore pressure diffusion.

In conclusion, we can use the dynamic triggering as the natural probe to test the stress state of

faults, it can help the industry figure out whether a fault system is in a ‘dangerous zone’ for productions or not, so the operators can adjust the production strategy to avoid the occurrences of destructive induced earthquakes. In addition, a detailed interpretation of the subsurface formations (e.g., possible hydraulic conduits), a better understanding of the triggering mechanisms, a thorough investigation and recognition on the characteristics of pre-existing faults, and a valuable forecast of injected fluid migration pattern could all help to assess the risks of triggering potential destructive induced earthquakes more precisely. All the above points need the collaboration among academic, industry, and regulator communities, so we can elucidate the dominating factors behind the HF-induced earthquakes more efficiently.

Déclenchement dynamique à distance au Canada et sismicité induite par la fracturation hydraulique en Colombie-Britannique

Résumé

Ce travail examine les caractéristiques des séismes déclenchés dynamiquement par des événements télésismiques au Canada et la sismicité induite par injection de fluide dans le bassin du Monteny, dans le nord-est de la Colombie-Britannique.

Nous examinons d'abord le déclenchement dynamique des tremblements de terre dans le catalogue de Ressources naturelles Canada (RNCan) pour l'ensemble du Canada, à la suite des chocs principaux qui ont eu lieu de 2004 à 2014 avec une magnitude de surface > 6 et des profondeurs < 100 km. L'analyse statistique du catalogue suggère que plusieurs régions du Canada sont capables d'un déclenchement dynamique, y compris l'île de Vancouver, le long de la frontière du Yukon et des Territoires du Nord-Ouest, dans l'ouest de l'Alberta, l'ouest de l'Ontario et la zone sismique de Charlevoix. Parmi ces régions, une grande partie de la propension observée au déclenchement se produit près des failles actives, mais dans certains cas, le déclenchement se produit en dehors des zones sismiques actives, ce qui suggère que la propension au déclenchement peut être corrélée à la propension à induire des séismes.

À partir des résultats de l'étude decatalogue, nous examinons d'abord le déclenchement près des sites d'injection dans l'ouest de l'Alberta, puis nous trouvons un déclenchement à distance associé à trois chocs principaux en utilisant une approche de filtre apparié sur des données de forme d'onde continue. Nous observons deux événements clairement déclenchés directement dans le train d'ondes de Rayleigh du tremblement de terre du 14/10/2014 de Salvador, mais avec des contraintes transitoires relativement faibles comparées aux études précédentes sur le déclenchement dynamique (< 1 kPa). La sensibilité de déclenchement à des perturbations de déformation et de contrainte aussi faibles suggère que des failles préexistantes dans la zone d'étude pourraient être soumises à une contrainte critique, ce qui pourrait être dû à l'injection continue de fluide. L'étude de la forme d'onde des événements déclenchés suggère qu'une longue période de secousse en dessous de 20 s pourrait être plus important pour le déclenchement que l'agitation cumulative ou l'énergie cumulative.

Ensuite, nous étudions la possibilité de déclenchement dynamique à distance dans trois autres régions canadiennes d'hydrocarbures non conventionnels, où l'activité récente d'injection de fluide est corrélée à un nombre croissant de tremblements de terre entre 2013 et 2015, notamment dans le

nord-est de la Colombie-Britannique et l'ouest de l'Alberta (CBA), Territoires du Nord-Ouest (TNO) et au Nouveau-Brunswick (NB), lorsque la couverture des stations a été augmentée pour surveiller l'activité des injections. Une approche double: 1) Recherche dans les formes d'onde directement après des événements télésismiques pour trouver des preuves d'un déclenchement immédiat et 2) Utilisation d'un catalogue amélioré de détection de MMF avec une analyse statistique pour vérifier si un déclenchement dynamique se produit. Les résultats suggèrent que les déclenchements directs et retardés se produisent dans les trois régions.

L'apparition de déclenchements consécutifs à des perturbations de contrainte transitoires inférieures à 10 kPa dans les trois régions susmentionnées suggère que les failles locales pourraient rester gravement sollicitées pendant des périodes similaires à celles de notre étude (environ 2 ans) ou plus longues, potentiellement en raison du maintien de fortes pressions interstitielles dans des formations de schiste étanches après l'injection. Après avoir étudié les facteurs physiques susceptibles d'influencer le déclenchement, nous avons constaté que 1) l'amplitude des secousses à basse fréquence constituait le facteur dominant du déclenchement dynamique, probablement en raison de la dilatation générée par les ondes sismiques modifiant la pression interstitielle, les vitesses de flux, et la perméabilité aux basses fréquences, et 2) un régime tectonique trans-tensionnel ou d'extension n'est pas une condition préalable au déclenchement dynamique, comme le suggèrent d'autres études, au moins dans les environnements d'injection. Enfin, BCAB connaît également une augmentation retardée de la sismicité (jusqu'à 10 jours) par rapport à NT et NB, qui montrent seulementun déclenchement dynamique immédiat. En raison de sa longue histoire en matière d'injection de fluide, BCAB suggère une augmentation de la sismicité immédiate par rapport à une sismicité retardée due à des contraintes transitoires qui peut résulter d'un transfert de contraintes via les perturbations de la matrice rocheuse et de la pression interstitielle, et pourrait fournir un mécanisme unificateur expliquant les deux types de déclenchement.

Outre le déclenchement dynamique, l'injection de fluide pourrait également être un facteur de déclenchement important pour les séismes induits. Ci-après, nous nous intéresserons tout d'abord à la sismicité dans le bassin de Montney, dans le nord-est de la Colombie-Britannique, étroitement liée aux activités HF, afin d'examiner les caractéristiques du taux sismique élevé après l'année 2011. Nous avons installé 8 stations sismiques à large bande au nord-ouest de Fort Saint-Jean (FSJ) du 13 mai au 7 octobre 2015. Le 17 août 2015, un séisme de M_w 4,6 s'est produit au nord-ouest de FSJ. Nous avons détecté plus de 300 séismes entre le 08/11/2015 et le 10/07/2015 à proximité de ce séisme de Mw 4.6 à l'aide d'une méthode MMF. Nous avons ensuite estimé leur moment sismique et leur fréquence de coupure en ajustant un modèle spectral de Brune aux spectres d'événements

individuels et aux rapports spectraux, respectivement, qui sont utilisés pour estimer la chute de contrainte. Les valeurs de chute de contrainte vont de 0,9 à 33,8 MPa et se situent dans la plage typique observée pour les événements tectoniques. Elles sont relativement plus petites que les autres estimations de chute de contrainte de séismes induits par HF dans le BSOC. Nous trouvons aussi qu'il y a un délai de 5 jours entre l'injection de HF et le séisme M_w 4,6, et une petite valeur b = 0,78 pour la séquence de réplique, de plus, l'événement M_w 4.6 est supérieur à la relation prévue entre le volume injecté en magnitude maximale et maximale de McGarr 2014. Tous les facteurs ci-dessus suggèrent que la séquence induite s'est produite sur une faille préexistante et que la magnitude maximale est contrôlée par des conditions tectoniques plutôt que par le volume d'injection cumulé.

Ensuite, nous étudions les mécanismes de déclenchement de ce séisme de M_w 4.6 en calculant le changement de la contrainte de Coulomb (ΔCFS) sur le récepteur de faille préexistant spécifique avec un modèle à ouverture de fracture et un modèle poroélastique numérique, avec une orientation de défaut calculée. Les résultats suggèrent que la diffusion de la pression interstitielle à travers un conduit hypothétique hautement perméable pourrait être le facteur dominant du déclenchement par rapport au faible changement de contrainte élastique par les ouvertures de fracture et de ΔCFS négatif par transfert de contrainte poroélastique unique.

Enfin, nous nous concentrons sur la réponse sismique immédiate (un jour) sur deux autres sites d'injection en utilisant les mêmes approches par rapport au délai de réponse de 5 jours du séisme M_w 4.6. Les résultats ΔCFS positifs suggèrent que les activités d'injection à proximité pourraient modifier le champ de contraintes et encourager les tremblements de terre locaux, mais les valeurs sont trop faibles pour permettre un lien solide entre les résultats. En général, les différentes échelles de temps de la réponse de déclenchement sur différents sites d'injection pourraient être dues à 1) l'état de contrainte initial de la faille et 2) le niveau de perturbations de contrainte.

En conclusion, nous pouvons utiliser le déclenchement dynamique comme sonde naturelle pour tester l'état de tension des pannes, aider l'industrie à déterminer si un système de pannes est dans une "zone dangereuse" pour les productions ou non En outre, une interprétation détaillée des formations souterraines, une meilleure compréhension des mécanismes de déclenchement, une enquête approfondie des caractéristiques des défauts préexistants, ainsi qu'une prévision intéressante du modèle de migration de fluide injecté pourraient: aident également à évaluer plus précisément les risques de déclenchement de séismes potentiellement destructeurs induits. Tous les points ci-dessus nécessitent la collaboration des milieux universitaires, industriels et des régulateurs afin d'élucider plus efficacement les facteurs dominants à l'origine des tremblements de terre induits par les HF.

Contents

List of Figures

List of Tables

Citations to Previously Published and in Preparation Work

Chapter 2 is mainly based on the following paper:

"Wang, B., Harrington, R. M., Liu, Y., Yu, H., Carey, A., & Elst, N. J. (2015). Isolated cases of remote dynamic triggering in Canada detected using cataloged earthquakes combined with a matched-filter approach. *Geophysical Research Letters, 42*(13), 5187-5196."

Chapter 3 refers to the following paper:

"Wang, B., Harrington, R. M., Liu, Y., Kao, H., & Yu, H. (2018). Remote Dynamic Triggering of Earthquakes in Three Unconventional Canadian Hydrocarbon Regions Based on a Multiple-Station Matched-Filter Approach. *Bulletin of the Seismological Society of America, 109*(1), 372-386. "

Chapter 4 is a paper in preparation for submission:

"Wang, B., Harrington, R. M., Liu, Y., Kao, H., & Yu, H. Static stress drop of the induced seismicity in the northern Montney Play, British Columbia, Canada. *In preparation for submission to Geophysical Research Letters*"

Chapter 5 is a paper in preparation for submission:

"Wang, B., Verdecchia, A., Harrington, R. M., Liu, Y., Kao, H., & Yu, H. Investigating the roles of Coulomb stress changes caused by fracture opening and poroelastic stress transfer associated with the induced earthquakes in the Montney Basin, British Columbia, Canada. *In preparation for submission to Geophysical Research Letters*"

Contribution of Authors

In Chapter 2, I did the data preparation and processing, code writing, some calculations, and chapter writing. The co-authors also contributed to the code and chapter writing, chapter modifying and reviewing, data processing.

In Chapter 3, I wrote the code, did the data processing, conceived and designed the analysis and wrote the chapter. The co-authors contributed to the data preparation and collection, data analysis, content reviewing and also the chapter writing.

In Chapter 4, I collected the data, wrote the most part of the code, designed and performed the analysis and wrote the chapter. The co-authors wrote part of the code, designed, conceived and performed part of the analysis and reviewed the chapter.

In Chapter 5, I collected the data, built the models, wrote the most part of the code, designed and performed the analysis and wrote the chapter. The co-authors helped designed, conceived and performed the analysis, and reviewed the chapter.

Acknowledgments

The completion of the thesis is attributed to many people's support and encouragement.

First and foremost, I want to extend my heartfelt gratitude to my co-supervisors, Prof. Rebecca M. Harrington and Prof. Yajing Liu, whose patient guidance, vast knowledge, great enthusiasm, valuable suggestions and constant encouragement accompanied me throughout my five years at McGill. Without their dedication guidance and encouragement to my research, it would not happen that I could successfully complete this thesis. Their conscientious academic spirit and modest, open-minded personality inspire me both in academic study and daily life. They give me much help and advice during the whole process of my research, which has made my accomplishments possible.

I would like to express my thanks to the committee members, Professors James Kirkpatrick, Olivia Jansen, Fiona Ann Darbyshire and Hongfeng Yang for following my progress and reviewing this thesis. I also want to thank Professor Christie Rowe for the 4-year's progress meeting to help me tracking my path to the finish of this dissertation.

I also want to thank the professors who have taught me in this university. Their instructions have helped broaden my horizon and their enlightening teaching has provided me with a solid foundation to accomplish this thesis and will always be of great value for my future career and academic research.

The members at earthquake process group at both McGill and Ruhr-Unvieristy Bochum, form a fantastic research family. I want to express all my thanks to Dr. Duo Li, Ge Li, John Onwuemeka,

Andres Felipe Peña Castro, Dr. Kai Deng, Dr. Alessandro Verdecchia, Marco Roth, Kilian Kemna, Lise Alalouf. The five year's companionship as colleagues really enlighten the path of scientific research.

I am very grateful to Dr. Honn Kao, Dr. Nicholas van der Elst, and others as the co-authors of my papers, their thoughts, data and code contribute enormous to the papers. I also want to thank Conan Drummond for his professional help in the fieldwork, so that we can set up our instruments much more easily.

My thanks also go to the sectaries and technicians at McGill and RUB, Ms Anne Kosowski, Ms Angela Di Ninno, Ms Kristy Thornton, Ms Agnes Otto, Ms Brigitte Dionne. Without all of your efficiently work, all of the issues related to graduation, VISA, traveling and technical instruments will not be solved so smoothly.

I would like to express my special thanks to my parents, whose care and support motivate me to move on and make me want to be a better person.

Last but not least, I want to thank my wife Hongyu Yu and my daughter Yiyi Wang. Five years are not long since we first met at McGill, but I know we still have our life long time to share our joys and tears in the future. Her support and love is my strongest shield facing the difficulties in my life.

Chapter 1

1.1 Introduction

An earthquake is the shaking of the Earth, as a consequence of global plate motion, and with a sudden release of energy. However, can we view the earthquakes as such a simple picture? The answer is obviously 'No'. The plate tectonic theories developed in the last century may answer some of the questions like why earthquakes occur between two rigid plates when they pass each other, how the accumulated strain from relative plate motions exceeds the fault's strength and causes the earthquake, but this simple interpretation is far from thorough for the cause of earthquakes. For example, could nearby earthquakes interact with each other? If so, how does this interaction work? Does it encourage or discourage the faulting? Is there any threshold on the distance for the interaction? Why do we sometimes observe a local seismicity rate increase after a large earthquake thousands of kilometers away, but sometimes we do not see the increase? Why do people experience more and more earthquakes in some of the intraplate tectonic regions without active plate motions? Could these earthquakes be triggered by human activities? If so, is there a threshold for the magnitude of the human induced earthquakes?

In this work, to investigate and answer some of the above questions, we will look into the earthquake-earthquake far field interaction (dynamic triggering) and human activity induced earthquakes in Canada, and use this work as a probe to get some insights into the earthquake triggering mechanisms.

1.2 Introduction to dynamic triggering

There are a lot of relatively critically stressed faults across the Earth's brittle crust (Zoback and Zoback, 2002). One of the mysterious questions in seismology is whether nearby or remote earthquakes from nature influence the slip occurrence on these local stressed faults, which is referred to dynamic triggering. Earthquakes occur when the accumulated shear stress on the fault driven by long-term motion exceeds the shear resistance of faults. However, measuring the rate of this long-term motion or the stress state on the fault may not be realistic (especially for intraplate regions), due to, for example, the complex local lithology, unknown subsurface formations, and the lack of access to the fault (a borehole can help to test the stress on the fault, but it is not that practical considering the expense and the limitation of drilling instruments). Thus, dynamic triggering can be used as a natural probe, by using the fault's response to the far field perturbations from the teleseismic events, to measure their proximity to failure.

1.2.1 Dynamic triggering examples

In North America, dynamic triggering is first documented for the 1992 M_w 7.3 Landers earthquake in southern California by Hill et al. (1993). After this Landers earthquake, the seismicity rates had increased throughout the western United States in a few hours, with a distance up to 1500 km, to the Yellowstone National Park. Fig.1.1 shows the increase of seismicity in 11 regions after the Landers earthquake in the United States.

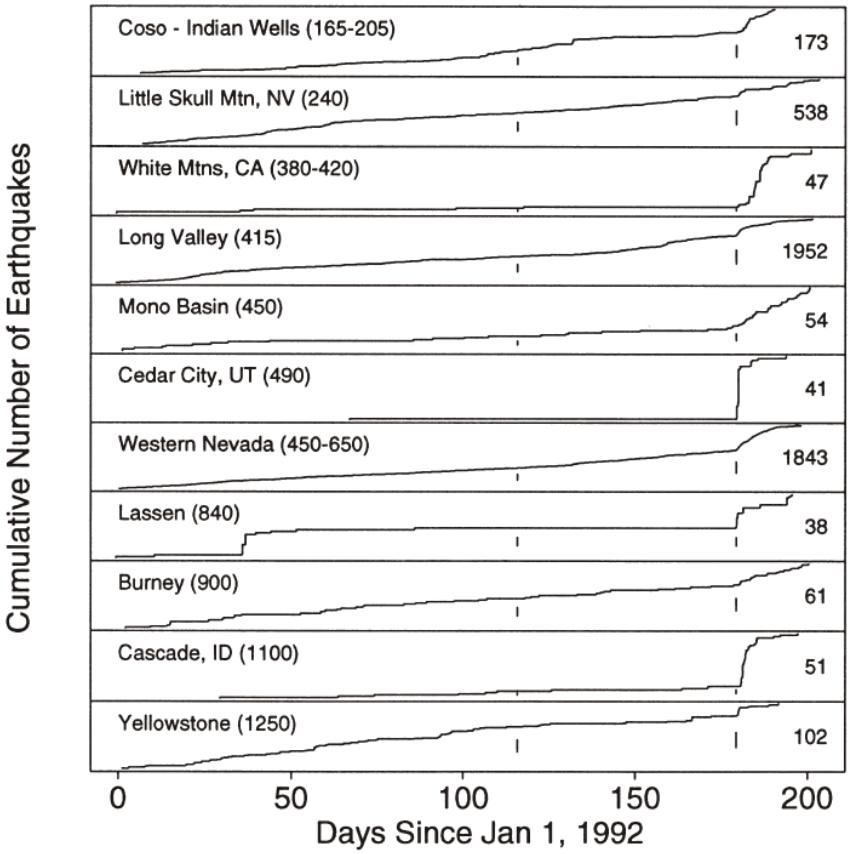

Fig.1.1 Cumulative number of locatable earthquakes at 11 sites in the western United States for 211 days beginning with 1 January 1992, after M_w 7.4 Landers, CA, earthquake (from Hill et al. 1993).

Then on October 1999, the M 7.1 Hector Mine Earthquake located 20 km east of the Landers rupture, triggered earthquakes up to ~750 km at Geysers geothermal field (Gomberg et al. 2001). The M 7.9 Denali Fault earthquake 2002, located at 65 km east of Denali National Park Alaska, generated dynamic stresses directed across western North America, triggered earthquakes at Mount Rainer, Long Valley caldera, and Yellowstone (e.g., Prejean et al., 2004; Husen et al., 2004b).

In Europe and Asia, dynamic triggering has also been investigated. For example, earthquakes have been triggered 40 km south of the M_w 5.4 earthquake at Roer Valley

Graben, Netherlands (Cambelbeek et al., 1994). Brodsky et al. (2000) investigated dynamic triggering in Greece for the M_w 7.4 Izmit, Turkey earthquake, and they found an increase in seismicity across the country. In Taiwan, dynamic triggering was studied by Wen et al. (1996), and they found the delay time for the dynamic triggering response could be up to 15 days. While in Japan, the dynamic triggering effect is relatively uncommon, which may be related to the compressional tectonics suggested by Harrington and Brodsky, 2006.

The dynamic triggering cases are mostly observed at volcano systems, Enhanced Geothermal Systems, and other extensional tectonic regions, where high-level historical seismicity rate have been observed. However, recent studies also show that the dynamic triggering could occur at regions with low historical seismicity rate. For example, Van der Elst et al. (2013) suggest that in several regions of United States with relatively low historical seismicity rate do experience dynamic triggering, and the common points for these regions are that they located near fluid injection sites, and they are experiencing an unusual increase of seismicity rate for the past decade related to fluid injection, suggesting human activities can alter the stress state of local faults, making them more susceptible to the remote stress perturbation.

1.2.2 Potential mechanisms of dynamic triggering

Most of the direct-triggered earthquakes are in the surface wave train, especially within the Raleigh wave, which could be due to the relatively large amplitude. Numerous studies investigate the potential dynamic triggering mechanism, for example, Coulomb failure under dynamic stresses (Hill, 2012), subcritical crack growth (Gomberg et al 2001; Brodsky and Prejean, 2006), permeability and pore pressure change caused by passing seismic waves

(Hough and Kanamori, 2002; Brodsky and Prejean, 2005), and bubble excitation (Brodsky et al. 1998). Fig.1.2 illustrates how the Coulomb failure model works (Hill, 2012).

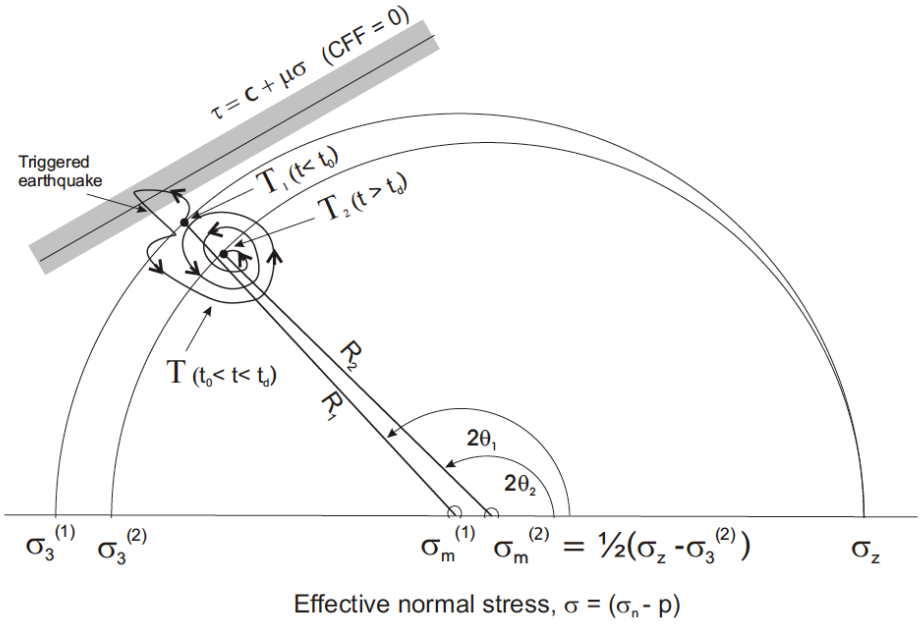

Fig.1.2 Schematic illustration of dynamic triggering in the Coulomb failure model in an extensional regime (from Hill 2012). The point $T_1 = T(R_1, \theta_1)$ denotes a stable stress state slightly below the failure threshold on a fault at an angle θ_1 with respect to the local least principal stress direction, σ_3. At $t = t_0$, dynamic stresses from a teleseismic event produce an oscillatory perturbation $T(R(t), \theta(t))$ in both the orientation and magnitude of the local stress field. Slip occurs whenever $T(R(t), \theta(t)$ touches the Coulomb failure zone.

For this Coulomb failure model, when the seismic waves arrive, the fault starts to oscillate; if the oscillatory trajectory reaches the failure zone, an earthquake can be triggered. In general, this model should be more viable for the critically stressed state and favorably orientated faults, but may not be suitable to explain the delayed dynamic triggering, due to the relatively small stress perturbation imposed from teleseismic events. The subcritical crack growth is well known in material science, that when a crack has a sudden change in loading, it could grow as the crack's tip is weakened by chemical corrosion (e.g., Anderson

and Grew, 1977). For the permeability and pore pressure change model, Elkhoury et al. (2006) suggest that the seismic waves can increase subsurface permeability, thus leading to a pore pressure change which may decrease the effective normal stress on the fault surface. The bubble excitation triggering mechanism is used to explain the triggered volcanic earthquakes, that the creation of new bubbles associated with dynamic stress in a supersaturated magma can lead to a pressure increase, which is responsible for the dynamic triggering of magmatic systems.

1.3 Introduction to induced seismicity

Compared to dynamic triggering which is a nature triggering process, induced seismicity refers to the earthquakes triggered by anthropogenic activities, due to the subsurface stress perturbations from processes including disposal water injection, hydraulic fracturing, oil and gas extraction, mining, enhanced geothermal energy exploitation, CO_2 sequestration and reservoir impoundment. For example, stress perturbations from disposal water injection, hydraulic fracturing and enhanced geothermal energy exploitation are from the injected fluids, which can increase the pore pressure; mining, oil and gas extraction introduce stress perturbations by compaction of the reservoir rock due to extensive depletion of fluid and gas, and the reservoir impoundment can affect the stability of the fault by 1) the static load due to the weight of water changing the shear and normal stresses on the fault plane and 2) pore pressure change in the rocks below the reservoir due to fluid diffusion.

1.3.1 Induced earthquake studies across the world

Two cases of induced earthquakes first drew people's attention in the 1960s in Colorado. A M 4.8 earthquake and many other small earthquakes occurred for the following

18 months after the disposal well ceased at Rocky Mountain Arsenal (e.g., Bardwell, 1966; Healy et al., 1968). Later, Raleigh et al. (1976) developed an experiment to investigate earthquake triggering by fluid injection at the Rangely oil field, Colorado. They found that the seismicity response time to the fluid injection can be less than one day, and the seismicity rate can be influenced by varying the reservoir pressure above or below the critical pressure threshold.

For the following 30 years, the area of induced earthquakes had become relatively quiet, as not a lot of earthquakes were related to human activities. However, after entering the 21st century, the earthquake rate has increased dramatically in North America. For instance, the number of M > 3 earthquake rose rapidly after the year 2008 in the central and eastern United States, as shown in Fig.1.3. In 2015, Oklahoma had almost 900 times more M > 3 earthquakes compared to the rate before 2009 (Langenbruch and Zoback, 2016). Yeck et al. (2016) suggest the M 5.1 earthquake at Fairview, Oklahoma could be triggered by a reactivation of basement fault due to the far field pressurization caused by saltwater injection. The largest recorded M 5.8 earthquake at Pawnee, Oklahoma may also be related to saltwater injection, which also influences local stream discharge (Langenbruch and Zoback, 2016; Manga et al., 2016; Barbour et al., 2017). Johann et al. (2018) built a new model to explain the induced earthquake at Oklahoma, and their result suggests the induced fluid above the crystalline basement may act similar to a water reservoir impoundment. Compared to Oklahoma, where nearly 90% of injected waste water comes from oil production (less than 10% of the water is used HF fluid), the earthquake sequences occurring in Youngstown, Ohio and Guy, Arkansas are largely related to the wastewater

generated from HF (e.g., Horton, 2012; Kim et al., 2013).

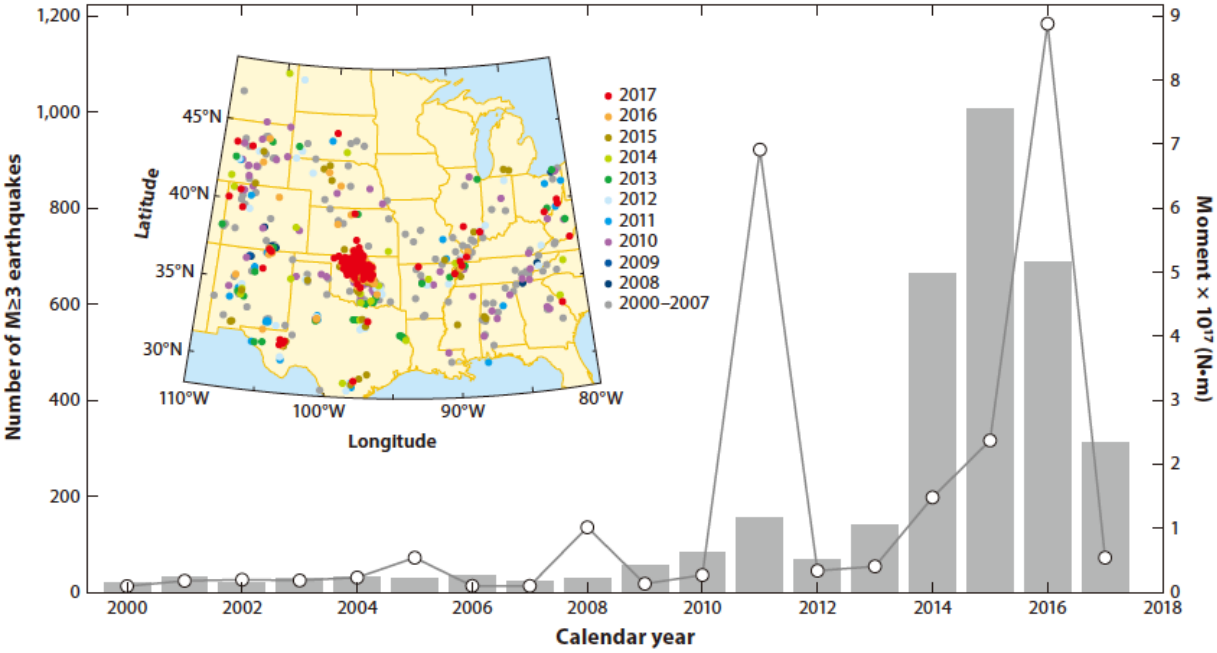

Fig.1.3 Number of M ≥ 3 earthquakes in the central United States from January 2000 to November 2017, together with the released seismic moment for each year (from Keranen and Weingarten, 2018). The gray bars denote the number of earthquakes and the solid line denotes the cumulated seismic moments.

Unlike in the United States, where most of the induced earthquakes are thought to be triggered by fluid injection, HF is regarded as the dominant triggering factor in the WCSB. Atkinson et al. (2016) suggest that recent seismic activity in the WCSB could be caused by HF operations, and they found that the maximum observed magnitude of induced events may exceed the predictions between the volume of injected fluid and the maximum expected magnitude. Schultz et al. (2017) investigate the characteristics of the 1/12/2016 M 4.1 earthquake and its aftershock sequence at Fox Creek, Alberta, which is one of the largest HF induced earthquakes in Canada; they suggest that sequences were triggered by pore pressure

increases caused by HF stimulations along previously existing faults, while results from numerical models by Deng et al. (2016) suggest that the poroelastic stress transfer is the dominant factor compared to pore pressure migration. Clerc et al. (2016) estimated the stress drops for the induced seismicity near Crooked Lake, Alberta, and they suggest the stress drop for the induced sequence falls at the high side of the typical range of tectonic events (~100MPa). Zhang et al. (2016) studied the focal mechanisms of HF induced earthquakes in the WCSB, in order to distinguish between tectonic events and induced earthquakes, they found that most of the induced events exhibit significant non-double-couple components. Bao and Eaton (2016) suggest the 01/23/2015 M_w 3.9 earthquake occurred on a pre-existing fault in the crystalline basement after several weeks' HF injection along the fault. After investigating the relationship between industry HF operation parameters and induced earthquakes. Schultz et al. (2018) suggest that the number of induced earthquakes is most plausibly related to the cumulative volume of injected fluids.

Europe and Asia also experience induced seismicity. Dost et al. (2012) study the induced seismicity by gas extraction operation in the Groningen between 1991 and 2002, northern Netherlands, where no historical earthquake has been recorded thus regarded as a tectonically stable region. Most of the earthquakes were located within the Groningen field, accompanied by ground surface subsidence due to gas extraction. Postma and Jansen (2018) investigate an idealized Groningen-like geometry to explore how the controllable and uncontrollable variables in the production process could affect the induced seismicity. In Basel, Switzerland, induced seismicity was connected to the Enhanced Geothermal Systems project (EGS), as the EGS uses hydraulic stimulation to enhance the reservoir permeability,

and pumping cold water into the subsurface formations to generate heat changes. Bachmann et al. (2012) found the EGS pore pressure relates to induced event size distribution by calculating *b*-values at different distances. In South Korea, in November 2017, a M 5.5 earthquake occurred, as one of the largest and most damaging events for this country over the last century, this earthquake located proximate to an EGS site, Grigoli et al. (2018) and Kim et al. (2018) both found that the EGS operation is the most plausible triggering factor, that the high-pressured fluid activates nearby unknown large faults. In China, Ge et al. (2008) suggest that the devastating 2008 M_w 7.9 Wenchuan earthquake could be triggered by the impoundment of Zipingpu Water Reservoir after calculating the Coulomb Stress perturbation, although some studies disagree with this conclusion (e.g., Deng et al., 2010). Lei et al., (2017) regard the 01/28/2017 M_w 4.7 earthquake induced by shale-gas HF in Sichuan Basin as a pre-existing fault reactivation in the Precambrian basement after calculation of the Coulomb Stress perturbation from a poroelastic model. Lei et al. (2019) suggest the recent two large earthquakes in South Sichuan Basin, the 12/16/2018 M 5.7 earthquake and the 01/03/2019 M 5.3 earthquake, are induced by shale gas HF after they investigate the spatiotemporal correlations between the earthquakes and HF zones, the statistic parameters of the seismicity and the estimated overpressure required to activate the unfavorably oriented source faults.

1.3.2 Potential triggering mechanisms for induced seismicity

The widely accepted triggering mechanism for induced seismicity is based on the Coulomb Failure Function, that if a fault reaches the Coulomb Failure criterion, the slip will occur. The Mohr-Coulomb fracture criterion can be expressed as the equation below,

$$\Delta CFS = \Delta\tau + \mu(\Delta\sigma + \Delta p) \quad (1.1)$$

where $\Delta\tau$ is the change in shear stress, ΔCFS is the change of Coulomb failure stress, $\Delta\sigma$ is the change of normal stress on the fault plane, μ is the friction coefficient and Δp is the pore pressure change (Reasenberg and Simpson, 1992). Positive ΔCFS indicates that the plane was brought closer to failure, while negative ΔCFS indicates that the plane of interest was moved away from failure. Fig.1.4 schematically shows how the fault failure is affected by the pore pressure and normal stresses change. Briefly, the increase of pore pressure from fluid diffusion could reduce the effective normal stress, and move the Mohr circle to the left, closer to the failure criterion; compared to the fluid diffusion, the poroelastic coupling between pore pressure and rock matrix could alter the normal and shear stresses of the solid. Poroelasticity is the interaction between fluid flow and solid deformation, that the deformation of the medium influences the fluid flow and vice versa. Instead of moving the Mohr circle to the left, it helps broadening the size of the Mohr circle, thus decreasing the gap between the current stress state and the failure criterion, and bringing the fault to failure (e.g., Healy et al., 1968; Segal and Lu, 2015).

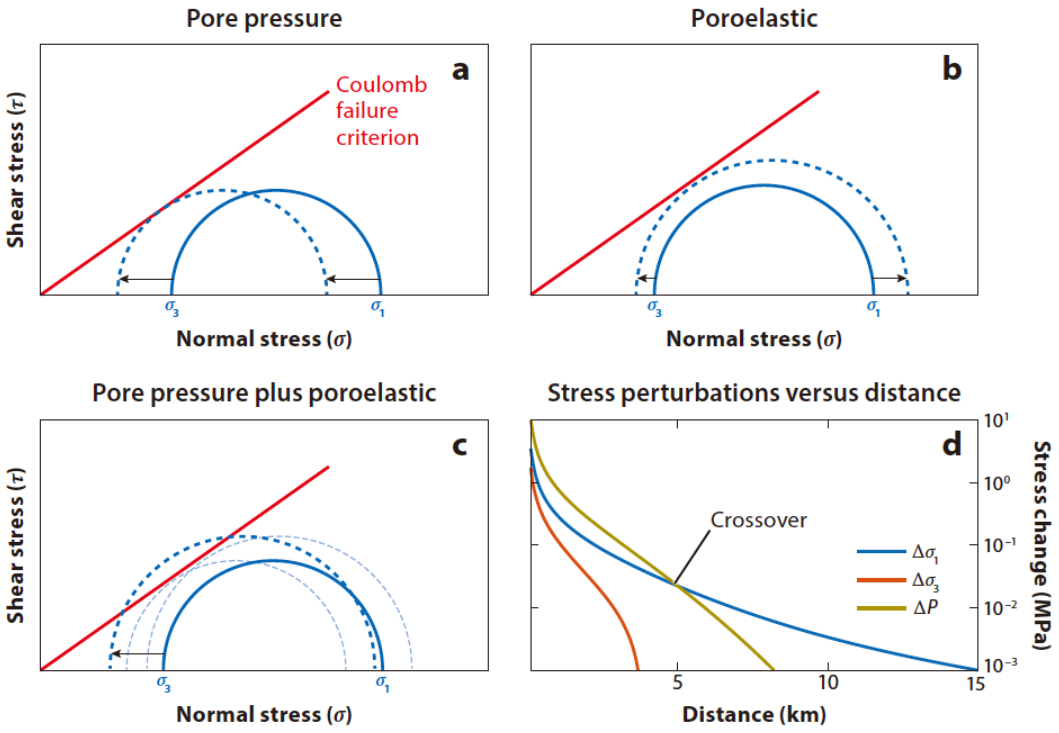

Fig.1.4 The schematic plots of the effects of pore pressure perturbation and poroelastic stress changes on fault failure (from Keranen and Weingarten, 2018). (a) The increased pore pressure decreases the normal stress on the fault. (b) Poroelastic stresses increase differential stress. (c) The combined effects of the pore pressure and poroelastic stress change. (d) Example of pore pressure and poroelastic stresses changes with increasing distance from a well.

1.4 Remaining problems related to dynamic triggering and induced seismicity, especially in Canada

As introduced above, cases of dynamic triggering have been documented across the world, but are rarely investigated in Canada. So, is Canada also capable of dynamic triggering? If the answer is yes, where do the triggered earthquakes prefer to occur, what will be the specific characteristics of the dynamic triggering in Canada, and what physical factors could be related to the triggering mechanism?

If we regard the dynamic triggering as a probe from nature, we can probably use this tool

to assess risks related to induced seismicity, but which also require a better understanding of the characteristics of induced seismicity. Studies suggest that the static stress drop for HF induced earthquakes in Alberta is relatively high, but do we expect to see the same stress drop range for the induced earthquakes in British Columbia? And what will be the characteristics of the stress drop for the induced earthquake sequences? In addition, although Canada has experienced a lot of HF induced earthquakes, the most plausible triggering mechanism for the HF induced earthquake sequences is still under debate, while understanding the triggering mechanisms could be the key factor to help the well operators to avoid the trigger of destructive earthquakes.

In the following first two chapters, we will focus on the dynamic triggering phenomena across Canada, including searching for regions prone to dynamic triggering, determining the controlling elements on why the specific regions are susceptible to dynamic triggering, the potential physical factors controlling the dynamic triggering, and the potential triggering mechanisms for the earthquakes with various responding time at different regions. Then in the next two chapters, we will investigate the properties of the HF induced earthquakes in British Columbia, including their spatiotemporal relationships to the proximal drilling wells, the source parameters (e.g., static stress drop) estimations and triggering mechanisms for the induced earthquakes. After answering the remaining questions mentioned above, we would discuss how people could use dynamic triggering as a tool to help assess the risks from induced earthquakes.

1.5 References for Chapter 1

Anderson, O. L., & Grew, P. C. (1977). Stress corrosion theory of crack propagation with applications to geophysics. *Reviews of Geophysics, 15*(1), 77-104.

Atkinson, G. M., Eaton, D. W., Ghofrani, H., Walker, D., Cheadle, B., Schultz, R., Shcherbakov, R., Tiampo, K., Gu, J., Harrington, R. M., Liu, Y. J., van der Baan, M., & Kao, H. (2016). Hydraulic Fracturing and Seismicity in the Western Canada Sedimentary Basin. *Seismological Research Letters, 87*(3), 631-647. doi: 10.1785/0220150263

Bachmann, C. E., Wiemer, S., Goertz-Allmann, B., & Woessner, J. (2012). Influence of pore-pressure on the event-size distribution of induced earthquakes. *Geophysical Research Letters, 39*(9), L09302, doi: 10.1029/2012GL051480.

Bao, X., & Eaton, D. W. (2016). Fault activation by hydraulic fracturing in western Canada. *Science, 354*(6318), 1406-1409.

Barbour, A. J., Norbeck, J. H., & Rubinstein, J. L. (2017). The effects of varying injection rates in Osage County, Oklahoma, on the 2016 M w 5.8 Pawnee earthquake. *Seismological Research Letters, 88*(4), 1040-1053.

Bardwell, G. E. (1966). Some statistical features of the relationship between Rocky Mountain Arsenal waste disposal and frequency of earthquakes. *The mountain geologist*.

Brodsky, E. E. (2006). Long-range triggered earthquakes that continue after the wave train passes. *Geophysical Research Letters, 33*(15), L15313, doi:10.1029/2006GL026605.

Brodsky, E. E., Karakostas, V., & Kanamori, H. (2000). A new observation of dynamically triggered regional seismicity: Earthquakes in Greece following the August, 1999 Izmit, Turkey earthquake. *Geophysical Research Letters, 27*(17), 2741-2744. doi: 10.1029/2000gl011534

Brodsky, E. E., & Prejean, S. G. (2005). New constraints on mechanisms of remotely triggered seismicity at Long Valley Caldera. *Journal of Geophysical Research-Solid Earth, 110*(B4). Doi 10.1029/2004jb003211

Brodsky, E. E., Sturtevant, B., & Kanamori, H. (1998). Earthquakes, volcanoes, and rectified diffusion. *Journal of Geophysical Research: Solid Earth, 103*(B10), 23827-23838.

Camelbeeck, T., & Van Eck, T. (1994). The 1992 Roermond earthquake, the Netherlands, and its aftershocks. *Geologie en Mijnbouw, 73*, 181-197.

Clerc, F., Harrington, R. M., Liu, Y., & Gu, Y. J. (2016). Stress drop estimates and hypocenter relocations of induced seismicity near Crooked Lake, Alberta. *Geophysical Research Letters, 43*(13), 6942-6951. doi: 10.1002/2016GL069800

Deng, K., Zhou, S., Wang, R., Robinson, R., Zhao, C., & Cheng, W. (2010). Evidence that the 2008 M_w 7.9 Wenchuan earthquake could not have been induced by the Zipingpu

Reservoir. *Bulletin of the Seismological Society of America, 100*(5B), 2805-2814.

Dost, B., Goutbeek, F., van Eck, T., & Kraaijpoel, D. (2012). Monitoring induced seismicity in the North of the Netherlands: status report 2010. *KNMI Scientific report, 2003*.

Elkhoury, J. E., Brodsky, E. E., & Agnew, D. C. (2006). Seismic waves increase permeability. *Nature, 441*(7097), 1135-1138.

Ge, S., Liu, M., Lu, N., Godt, J. W., & Luo, G. (2009). Did the Zipingpu reservoir trigger the 2008 Wenchuan earthquake? *Geophysical Research Letters, 36*(20), L20315, doi:10.1029/2009GL040349.

Gomberg, J., Reasenberg, P. A., Bodin, P., & Harris, R. A. (2001). Earthquake triggering by seismic waves following the Landers and Hector Mine earthquakes. *Nature, 411*(6836), 462-466. doi: 10.1038/35078053

Grigoli, F., Cesca, S., Rinaldi, A., Manconi, A., López-Comino, J., Clinton, J., Westaway, R., Cauzzi, C., Dahm, T., & Wiemer, S. (2018). The November 2017 Mw 5.5 Pohang earthquake: A possible case of induced seismicity in South Korea. *Science, 360*(6392), 1003-1006.

Harrington, R. M., & Brodsky, E. E. (2006). The absence of remotely triggered seismicity in Japan. *Bulletin of the Seismological Society of America, 96*(3), 871-878. doi: 10.1785/0120050076

Healy, J. H., Rubey, W. W., Griggs, D. T., & Raleigh, C. B. (1968). The Denver Earthquakes. *Science, 161*(3848), 1301-1310. doi: 10.1126/science.161.3848.1301

Hill, D. P. (2012). Dynamic stresses, Coulomb failure, and remote triggering—Corrected. *Bulletin of the Seismological Society of America, 102*(6), 2313-2336.

Hill, D. P., Reasenberg, P. A., Michael, A., Arabaz, W. J., Beroza, G., Brumbaugh, D., Brune, J. N., Castro, R., Davis, S., Depolo, D., Ellsworth, W. L., Gomberg, J., Harmsen, S., House, L., Jackson, S. M., Johnston, M. J., Jones, L., Keller, R., Malone, S., Munguia, L., Nava, S., Pechmann, J. C., Sanford, A., Simpson, R. W., Smith, R. B., Stark, M., Stickney, M., Vidal, A., Walter, S., Wong, V., & Zollweg, J. (1993). Seismicity remotely triggered by the magnitude 7.3 Landers, california, earthquake. *Science, 260*(5114), 1617-1623. doi: 10.1126/science.260.5114.1617

Horton, S. (2012). Disposal of hydrofracking waste fluid by injection into subsurface aquifers triggers earthquake swarm in central Arkansas with potential for damaging earthquake. *Seismological Research Letters, 83*(2), 250-260.

Hough, S. E., & Kanamori, H. (2002). Source properties of earthquakes near the Salton Sea

triggered by the 16 October 1999 M 7.1 Hector Mine, California, earthquake. *Bulletin of the Seismological Society of America, 92*(4), 1281-1289.

Husen, S., Wiemer, S., & Smith, R. B. (2004). Remotely triggered seismicity in the Yellowstone National Park region by the 2002 M_w 7.9 Denali fault earthquake, Alaska. *Bulletin of the Seismological Society of America, 94*(6B), S317-S331.

Johann, L., Shapiro, S. A., & Dinske, C. (2018). The surge of earthquakes in Central Oklahoma has features of reservoir-induced seismicity. *Scientific reports, 8*(1), 11505.

Keranen, K. M., & Weingarten, M. (2018). Induced seismicity. *Annual Review of Earth and Planetary Sciences, 46*, 149-174.

Kim, W. Y. (2013). Induced seismicity associated with fluid injection into a deep well in Youngstown, Ohio. *Journal of Geophysical Research-Solid Earth, 118*(7), 3506-3518. doi: 10.1002/Jgrb.50247

Kim, K.-H., Ree, J.-H., Kim, Y., Kim, S., Kang, S. Y., & Seo, W. (2018). Assessing whether the 2017 Mw 5.4 Pohang earthquake in South Korea was an induced event. *Science, 360*(6392), 1007-1009.

Langenbruch, C., & Zoback, M. D. (2016). How will induced seismicity in Oklahoma respond to decreased saltwater injection rates? *Science Advances, 2*(11), e1601542.

Lei, X., Huang, D., Su, J., Jiang, G., Wang, X., Wang, H., Guo, X., & Fu, H. (2017). Fault reactivation and earthquakes with magnitudes of up to M_w 4.7 induced by shale-gas hydraulic fracturing in Sichuan Basin, China. *Scientific reports, 7*(1), 7971.

Lei, X., Wang, Z., & Su, J. (2019). The December 2018 ML 5.7 and January 2019 ML 5.3 Earthquakes in South Sichuan Basin Induced by Shale Gas Hydraulic Fracturing. *Seismological Research Letters, 90*(3), 1099-1110.

Manga, M., Wang, C. Y., & Shirzaei, M. (2016). Increased stream discharge after the 3 September 2016 Mw 5.8 Pawnee, Oklahoma earthquake. *Geophysical Research Letters, 43*(22), 11,588-511,594.

Postma, T., & Jansen, J. D. (2018). The small effect of poroelastic pressure transients on triggering of production-induced earthquakes in the Groningen natural gas field. *Journal of Geophysical Research: Solid Earth, 123*(1), 401-417.

Prejean, S., Hill, D., Brodsky, E. E., Hough, S., Johnston, M., Malone, S., Oppenheimer, D., Pitt, A., & Richards-Dinger, K. (2004). Remotely triggered seismicity on the United States west coast following the Mw 7.9 Denali Fault earthquake. *Bulletin of the Seismological Society of America, 94*(6B), S348-S359.

Raleigh, C., Healy, J., & Bredehoeft, J. (1976). An experiment in earthquake control at Rangely, Colorado. *Science, 191*(4233), 1230-1237.

Reasenberg, P. A., & Simpson, R. W. (1992). Response of regional seismicity to the static stress change produced by the Loma Prieta earthquake. *Science, 255*(5052), 1687-1690. doi: 10.1126/science.255.5052.1687

Schultz, R., Atkinson, G., Eaton, D., Gu, Y., & Kao, H. (2018). Hydraulic fracturing volume is associated with induced earthquake productivity in the Duvernay play. *Science, 359*(6373), 304-308.

Schultz, R., Wang, R., Gu, Y. J., Haug, K., & Atkinson, G. (2017). A seismological overview of the induced earthquakes in the Duvernay play near Fox Creek, Alberta. *Journal of Geophysical Research: Solid Earth, 122*(1), 492-505.

Segall, P., & Lu, S. (2015). Injection-induced seismicity: Poroelastic and earthquake nucleation effects. *Journal of Geophysical Research: Solid Earth, 120*(7), 5082-5103.

Wen, K.-L., Beresnev, I. A., & Cheng, S.-N. (1996). Moderate-magnitude seismicity remotely triggered in the Taiwan region by large earthquakes around the Philippine Sea plate. *Bulletin of the Seismological Society of America, 86*(3), 843-847.

Yeck, W. L., Weingarten, M., Benz, H. M., McNamara, D. E., Bergman, E., Herrmann, R., Rubinstein, J. L., & Earle, P. (2016). Far-field pressurization likely caused one of the largest injection induced earthquakes by reactivating a large preexisting basement fault structure. *Geophysical Research Letters, 43*(19), 10,198-110,207.

Zhang, H., Eaton, D. W., Li, G., Liu, Y., & Harrington, R. M. (2016). Discriminating induced seismicity from natural earthquakes using moment tensors and source spectra. *Journal of Geophysical Research: Solid Earth*, 121,972– 993, doi:10.1002/2015JB012603.

Zoback, M. D., & Zoback, M. L. (2002). 34 State of stress in the Earth's lithosphere. International Geophysics, 81, 559.

Chapter 2

Isolated cases of remote dynamic triggering in Canada detected using cataloged earthquakes combined with a matched-filter approach

2.1 Introduction

Earthquake triggering by transient stresses from seismic waves of distant mainshocks has been documented in many studies (Hill et al., 1993; Gomberg et al., 2001; Prejean et al., 2004; Brodsky and van der Elst, 2014). Triggering propensity may be correlated with conditions such as volcanic or geothermal activity, and extensional tectonics (e.g., Brodsky and Prejean, 2005, Moran et al. 2004, Harrington and Brodsky, 2006). Most cases of observed remote dynamic triggering are where natural earthquakes tend to occur, but recent studies show triggering in regions with low levels of historical seismicity, such as near active fluid injection sites. Locations where triggering occurs may therefore reveal regions of critical ambient stress conditions, independent of proximity to plate-boundary faults (van der Elst et al., 2013). In the following, the term induced seismicity refers to events that nucleate as the result of anthropogenic activity (e.g., fluid injection), whereas triggered seismicity refers to events triggered by natural stress perturbations (e.g., from passing of seismic waves), regardless of how the seismogenic faults were brought to a critically stressed state.

Here we perform a broad search for triggering in Canada using earthquake catalog data, followed by a more detailed search in Alberta, where denser seismic station coverage monitors seismic activity associated with fluid injection related to oil and gas production

(Wetmiller, 1986; Stern et al., 2013; Schultz et al., 2014; Schultz et al., 2015b). Our statistical tests of triggering using catalog data suggest various locations throughout Canada have a propensity for triggering, particularly in western Canada (e.g., Cascadia Subduction Zone, along the border of the Northwest Territories and the Yukon), eastern British Columbia and western Alberta near regions of oil and gas production, southwest Ontario, and along the St. Lawrence rift system in eastern Canada.

Following the Canada-wide catalog study, we perform a more detailed catalog search combined with a matched-filter approach in Alberta. The reason for focusing on Alberta is that station coverage has become denser in the last five years, and the area is known to experience a significant amount of induced seismicity. The relative abundance of waveform data also means that the earthquake catalog is more complete. Waveform data analysis reveals evidence of both direct triggering in the surface-wave train of one mainshock in 2014, and evidence of delayed triggering within 12 hours of the local arrival times of three mainshocks. We first describe the catalog study for Canada, followed by the waveform study for Alberta and the results, followed by a discussion and conclusion section.

2.2 Investigation of dynamic triggering through NRCan catalog

We begin our search for triggering in Canada by identifying potential triggering mainshocks between 2004 and 2014 with depths < 100 km and surface wave magnitude M_S > 6 in the International Seismological Center catalog (ISC). We use the M_S scale as surface wave shaking is the dominant factor for dynamic triggering (Hill et al., 1993; Brodsky et al., 2000; Hill and Prejean, 2007). We further restrict the list of mainshocks to earthquakes that produced an estimated peak ground velocity (PGV) shaking > 0.2 cm/s in any part of Canada,

where PGV values over much of the country could be well below that threshold. The 0.2 cm/s cutoff is based on documented cases of dynamic triggering in a variety of geologic and tectonic settings (Brodsky et al., 2000; Gomberg et al., 2001; Harrington and Brodsky, 2006; Peng et al., 2009). Using a lower threshold would likely not cause the rate of triggering to vary significantly given the sparse station coverage in Canada, and a higher triggering threshold may result in too few mainshocks and thus too few events for a statistical analysis. PGV is estimated using the following empirical ground motion regression (Lay and Wallace, 1995):

$$\mathrm{Log}A_{20} = M_s - 1.66\mathrm{Log}_{10}\delta - 2 \tag{2.1}$$

$$\mathrm{PGV} \approx \frac{2\pi A_{20}}{T} \tag{2.2}$$

where δ is epicenter-station distance in degrees, T is surface wave period (T = 20 s), and A_{20} is peak waveform amplitude filtered at 20 s. Tab.2.1 lists the 19 mainshocks satisfying the above criteria.

1	2004/12/26 10:02:08	M_s 8.9	Off W Coast of Northern Indonesia
2	2005/03/28 16:10:31	M_s 8.4	Northern Sumatra, Indonesia
3	2005/06/15 02:50:93	M_s 7.4	Off coast of Northern California
4	2006/04/20 23:24:59	M_s 8.3	Eastern Siberia, Russia
5	2006/05/03 15:27:33	M_s 7.9	Tonga Islands
6	2006/11/15 11:15:18	M_s 8.3	Kuril Islands
7	2008/01/05 11:01:00	M_s 6.7	Vancouver Island Region
8	2008/01/09 14:40:03	M_s 6.1	Queen Charlotte Islands Region
9	2009/11/17 15:30:35	M_s 6.8	West of Vancouver Island
10	2011/03/11 05:46:19	M_s 8.7	Near East coast of Hongshu, Japan
11	2011/09/09 19:41:28	M_s 6.6	Vancouver Island Region
12	2012/10/28 18:54:20	M_s 6.2	Queen Charlotte Islands Region
13	2012/10/30 02:49:02	M_s 6.0	Queen Charlotte Islands Region

14	2012/11/08 02:01:05	M_s 6.1	Vancouver Island Region
15	2013/01/05 08:58:19	M_s 7.7	Southeastern Alaska
16	2013/09/03 20:19:06	M_s 6.1	Queen Charlotte Islands Region
17	2013/09/04 00:23:09	M_s 6.2	Queen Charlotte Islands Region
18	2014/07/17 11:49:33	M_s 6.0	Southeastern Alaska
19	2014/07/25 10:54:49	M_s 6.0	Southeastern Alaska

Tab.2.1 19 mainshocks that have generated shaking exceeding 0.2 cm/s in Canada over the last decade.

We then count earthquakes in Canada using the NRCan catalog (completeness threshold of ~ 3) (Fig.2.2) in 10-day windows before and after each mainshock. Events are then grouped into 1° × 1° spatial bins. The 10-day window is chosen to maximize the number of recorded earthquakes temporally associated with the mainshock. Ideally, the size of the spatial bin should be smaller than the wavelength of the dominant triggering phase. However, we need to choose the 1° × 1° bins to contain more than just a few earthquakes due to the low level of recorded seismicity (van der Elst and Brodsky, 2010).

The β statistic is a widely accepted quantitative measure of the level of dynamic triggering, representing the standard deviation in the background seismicity rate following a remote dynamic stressing event (Matthews and Reasenberg, 1988; Reasenberg and Simpson, 1992; Hill and Prejean, 2007). The β statistic is given by the following equation for each 1°-bin (Matthews and Reasenberg, 1988):

$$\beta(N_1, N_2, t_1, t_2) = \frac{N_2 - E(N_2)}{\sqrt{var(N_2)}} \quad (2.3)$$

where N_1, N_2 are numbers of earthquakes, and t_1, t_2 are time windows lengths before and after the mainshock. For a Poisson process, $var(N_2) = N_2 \times t_1/t_2$, where $t_1 = t_2$ is assumed here. $E(N_2) = N_1 \times t_2/t_1$ represents the expected number of earthquakes after the mainshock based on the pre-mainshock seismicity rate. If no earthquakes occur in a given bin before the mainshock, N_1 is set to 0.25 based on the equivalent range of the probability density function (Matthews and Reasenberg, 1988; Hough, 2005). In general, a β statistic > 2 indicates a significant increase in seismic activity at a 95% confidence level (Hill and Prejean, 2007).

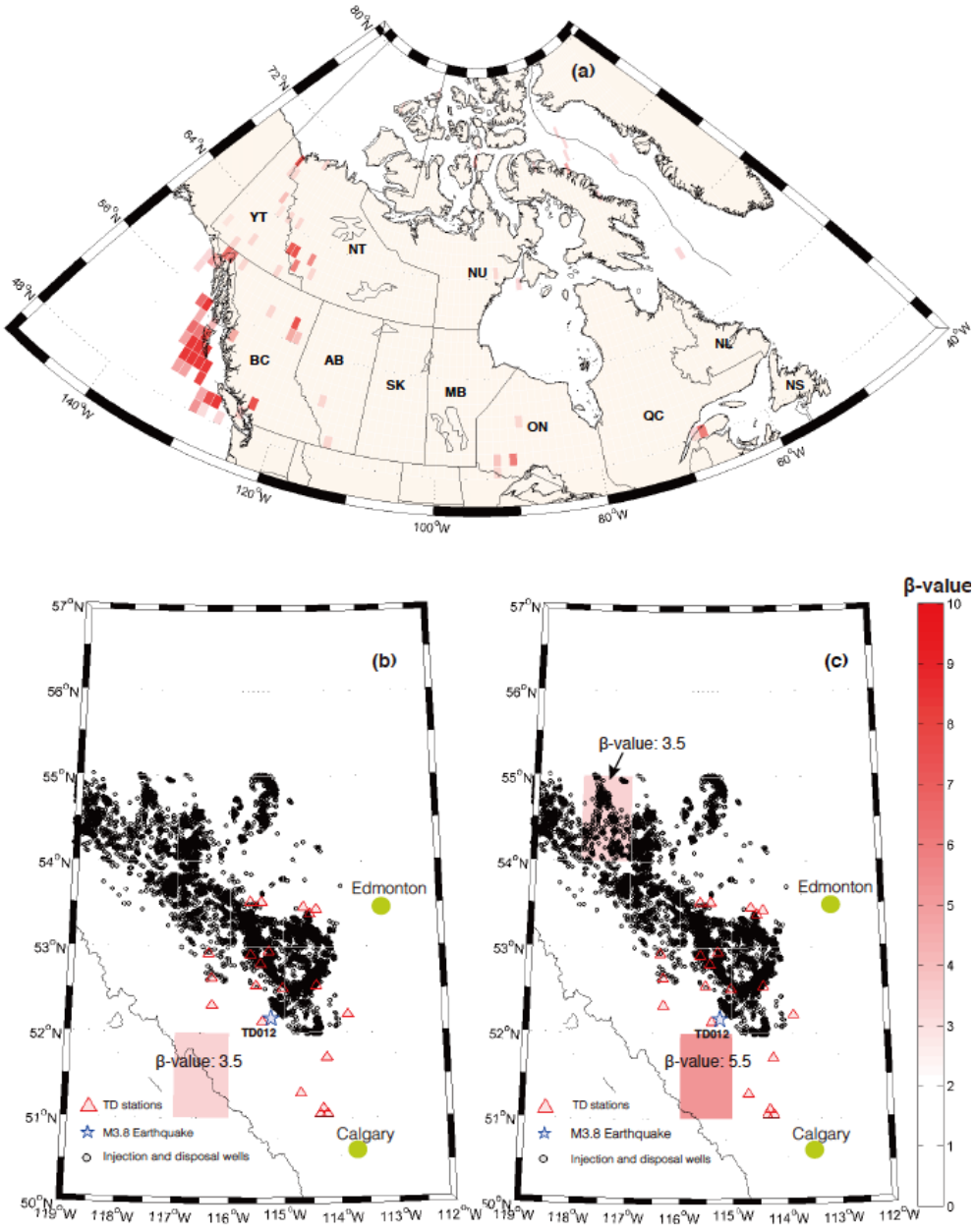

Fig.2.1 β statistic calculated in 1° X 1° bins for (a) all of Canada using seismicity from NRCan catalog before and after 19 mainshocks listed in Tab.2.1, (b) for Alberta using seismicity from the AGS catalog from 04/2006 – 12/2010 before and after 4 mainshocks, and (c) for Alberta using seismicity from the AC catalog from 01/2014 – 11/2014 before and after 3 mainshocks in Tab.2.3. β statistic calculated using seismicity 10 days before and after each mainshock using equation 2.3 (see text). Colorbar is the same for (a) (b) and (c). Black dots in Figs.2.1 (b) and (c) denote injection wells between 52-55°N and 114-119°W (Gail Atkinson, personal communication).

Fig.2.1a shows the β statistic in Canada for all 19 mainshocks with all earthquakes stacked in each bin, to compensate for the low seismicity levels. The apparent increase in triggering propensity after 2007 is likely an artifact of the decrease in catalog completeness magnitude from approximately M_C 5 to M_C 3.5 after 2007.

We take caution not to place too much weight on the statistical robustness of the Canada-wide catalog study given the relatively low seismicity rates. However, the catalog results point to regions where further in-depth searches for triggering are warranted. We focus on Alberta as one such region, with high seismicity levels in proximity to injection wells and denser seismic station coverage.

Specifically, we use two regional earthquake catalogs covering two different periods of completeness magnitudes M_C lower than that from NRCan. We begin with the Alberta Geological Survey (AGS) catalog with a $M_C \sim 2.45$ for the period of September 2006 to December 2010 (Stern et al., 2013; Schultz et al., 2015a). Four mainshocks in Tab.2.2 satisfy the criteria for triggering mainshocks during the AGS catalog period. We also calculate the β statistic following mainshocks in 2014 using the Alberta Composite (AC) catalog running from January to November, 2014 ($M_C \sim 2.8$, Fig.2.2). Three potential triggering mainshocks occurred during the time period of the AC catalog: the 2014/07/25 M_S 6.0 Southeastern Alaska earthquake, the 2014/08/24 M_S 6.1 South Napa earthquake and the 2014/10/14 M_S 7.3 El Salvador earthquake. Note the three mainshocks in 2014 generated the largest PGVs (0.07 mm/s, 0.10 mm/s, and 0.05 mm/s, respectively) in Alberta during the AC catalog period, but all fall below our initial threshold cutoff of 0.2 cm/s. Figs.2.1b and 2.1c

show the stacked β statistic using the AGS and AC catalogs, respectively (β statistic for individual mainshocks are shown in the supplemental figures). Shaded areas are indicative of triggering in parts of western Alberta, which we discuss in more detail in Section 2.5.

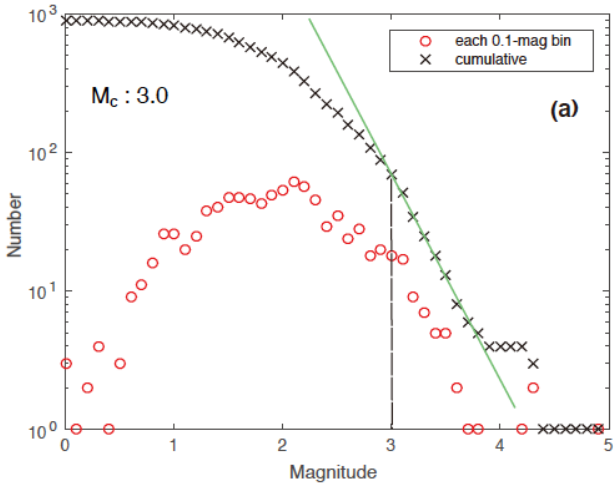

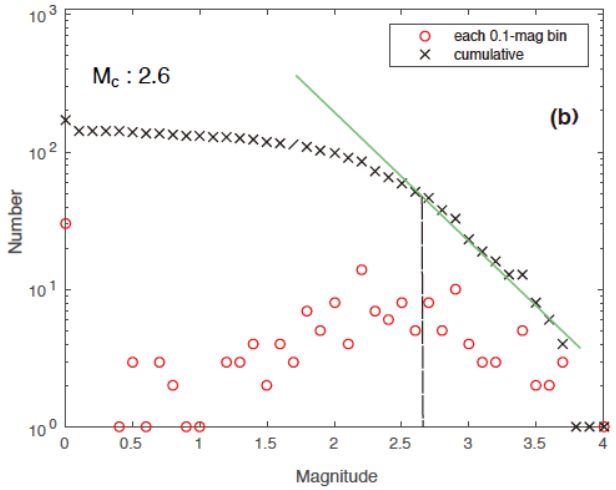

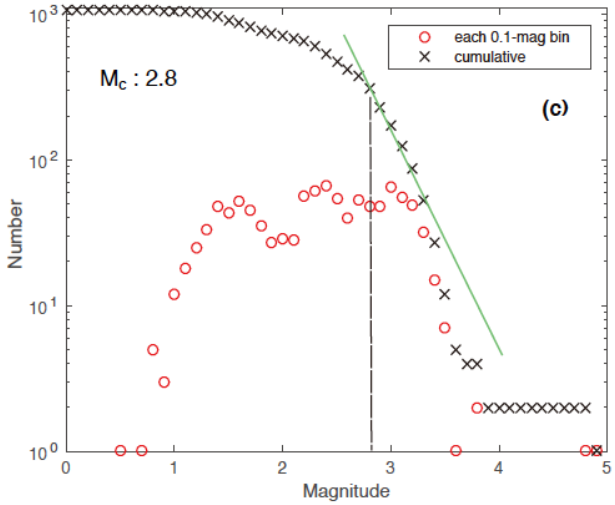

Fig.2.1 Catalog completeness (M_c) calculation from Gutenberg-Richter (GR) law. The green solid line represents the best fit from GR law using a maximum likelihood estimate. The dashed line indicates the catalog completeness value. (a) M_c for NRCan Catalog of Alberta from 2004-2014. (b) M_c for Alberta Geological Survey Catalog from Apr.2006-Dec.2010 (c) M_c for Alberta Composite Catalog from 2014/01/01-2014/11/01.

1	2006/11/15 11:15:18	M_s 8.3	Kuril Islands
2	2008/01/05 11:01:00	M_s 6.7	Vancouver Island Region
3	2008/01/09 14:40:03	M_s 6.1	Queen Charlotte Islands Region
4	2009/11/17 15:30:35	M_s 6.8	West of Vancouver Island

Tab.2.2 Four mainshocks used for calculating the β-value in Alberta using the Alberta Geological Survey catalog from September 2006 to December 2010.

2.3 Searching for potential uncataloged triggered earthquakes through waveforms

The TransAlta Dam Monitoring Network (network TD) became operational in 2014 in western Alberta. Given the high station density and the propensity for triggering near the TD network, we focus our waveform study around the TD array. Earthquake waveforms recorded at TD stations show station TD012 has the highest signal-to-noise ratio (SNR) for most events, therefore we use station TD012 in a matched-filter approach to detect uncataloged events.

2.3.1 Introduction to the matched-filter approach

We apply a single-station matched-filter approach using continuous waveform data recorded at station TD012 to search for uncataloged earthquakes based on similarity to known events. Similar methods have been used to identify tectonic tremor in Japan and

micro-earthquakes in the US (Shelly et al., 2007; van der Elst et al., 2013). The matched-filter approach searches for events by cross-correlating known events or event stacks, referred to as templates, with continuously recorded data. Detection is declared when the cross-correlation coefficient exceeds some pre-determined threshold set by the user.

Western Alberta experiences a large number of what are likely hydraulic fracturing related events, such as the M_L 4.4 earthquake near Fox Creek on 2015/01/23 (Schultz et al., 2015b). A M_L 3.8 earthquake southwest of Rocky Mountain House also occurred on 2014/08/09 near previously documented induced earthquakes (Wetmiller, 1986; Baranova et al., 1999; Stern et al., 2013), although the event was not spatially or temporally correlated with any reported hydraulic fracturing activity (Schultz, personal communication). We use the 2014/08/09 earthquake and seven other similar events recorded in the AC catalog, to construct five templates for each channel of station TD012 (Fig.2.3). (Note that some templates are stacks of events, while some are individual events). To create templates, we cut waveform data filtered between 5 and 12 Hz in 15-second time windows that include P and S-arrivals of the known events. Templates consisting of stacked events are aligned on the S-wave arrivals. Fig.2.4 shows three-component waveforms of the five templates created for this study. We then cross-correlate all templates with three components of the continuous data at station TD012 to search for uncataloged events surrounding the three mainshocks in 2014. We declare an event detection when the cross-correlation coefficient exceeds 5.5 standard deviations above the noise level. The 5.5 standard deviation cutoff value is determined by trial-and-error based on the tradeoff between detection sensitivity and the acceptable number of false detections. We then remove false detections by inspecting waveforms at all stations

high-pass filtered at 1 Hz. Only events that can be identified at more than one station are regarded legitimate detections.

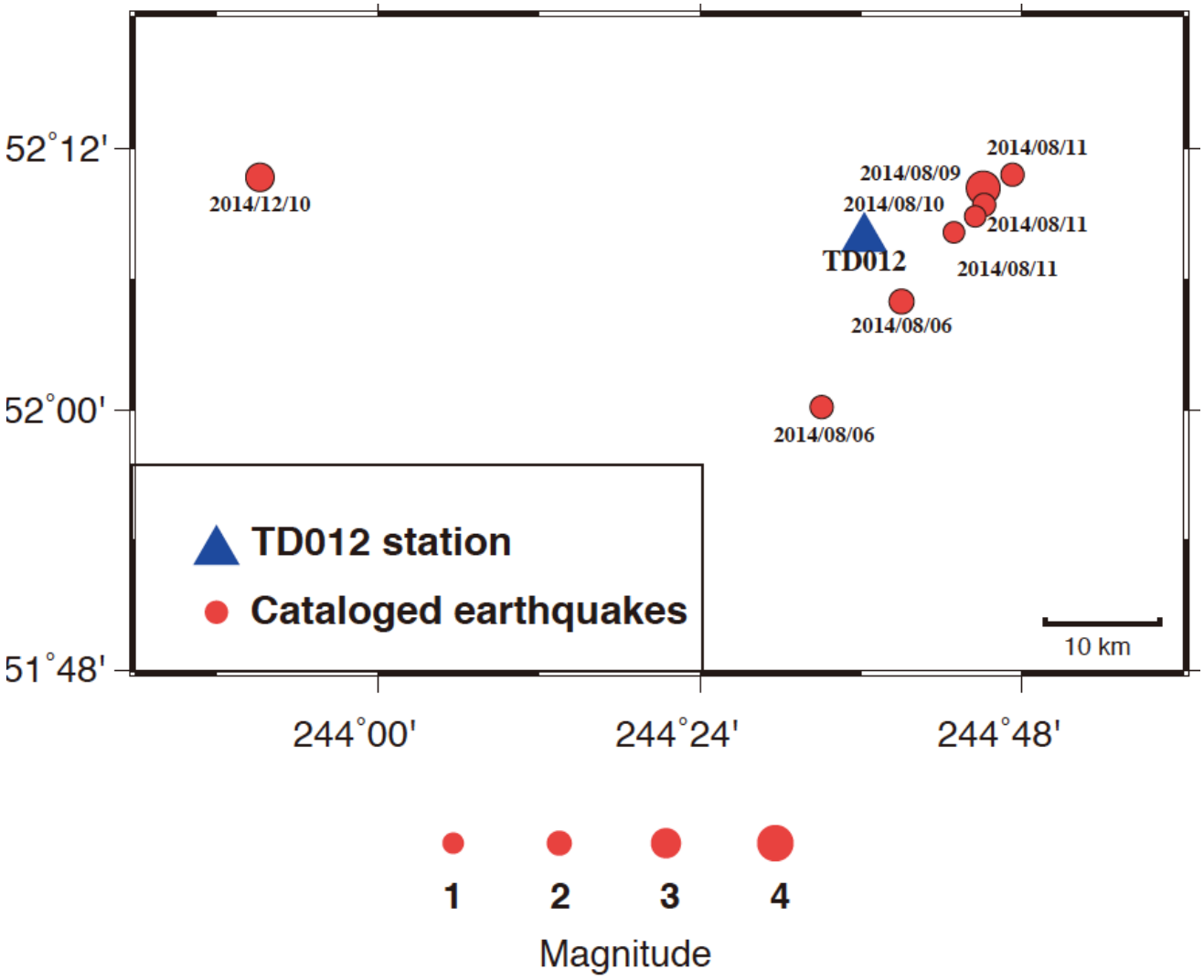

Fig.2.3 TD012 station and NRCan cataloged earthquakes in Alberta after the installation of TransAlta Network. These earthquakes are used to construct the templates. Symbol size corresponds to the earthquake magnitude.

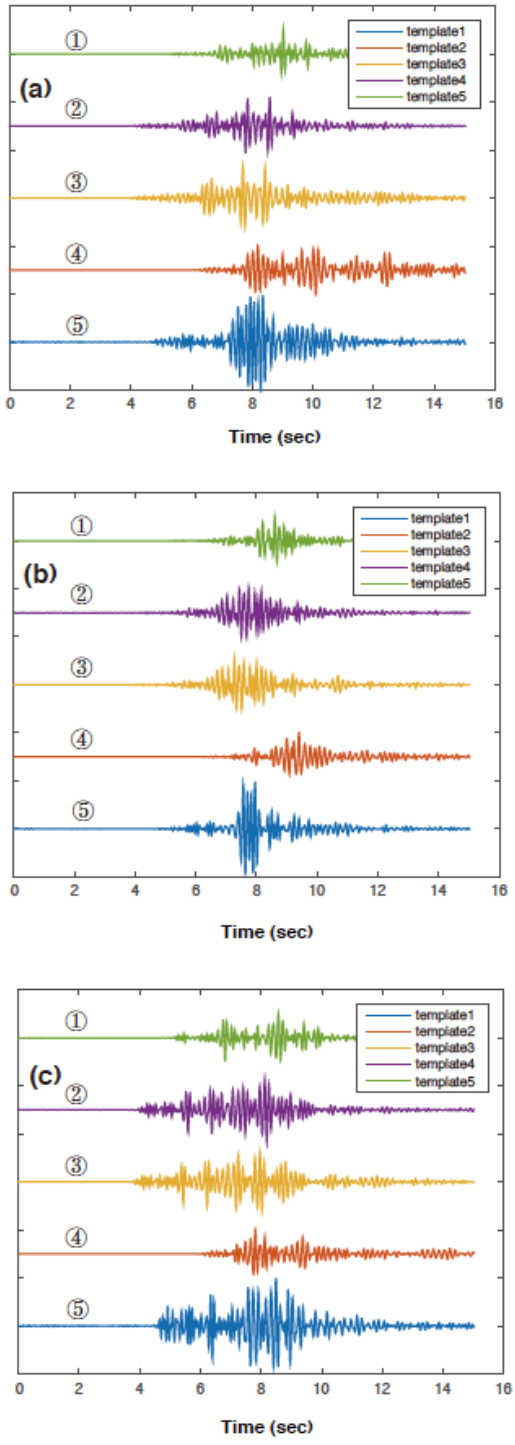

Fig.2.4 Normalized template waveforms used in match-filter detection on continuous waveforms to detect micro-earthquakes. Template locations are shown in Fig.2.3. Template ① and template ③ are stacked from multiple earthquakes with cross correlation value larger than 0.85, remaining templates are built with single events. (a) Templates built from channel HH1 (b) Templates built from channel HH2 (c) Templates built from channel HHZ.

The delay between the origin time of a dynamically triggered earthquake and the imposed transient stress could range from s to days (Beresnev et al., 1995; Prejean et al., 2004; Hill and Prejean, 2007). Therefore, we look at the changes in background seismicity in 12-hour time windows on either side of the mainshock for the waveform study. The primary reason for using the shorter time window compared with the catalog study is to avoid a tenuous causal link between dynamic stress and local seismicity rate with a longer time window (Hill and Prejean, 2007). Secondly, most of the TD stations began operation on 2014/07/23, collecting just two days of waveform data before the 2014/07/25 Southeastern Alaska Earthquake. The 12-hour window guarantees we compare seismicity levels for equal time periods before and after the Alaska mainshock.

Fig.2.5 shows the histograms of earthquakes detected with the matched-filter approach. After removing false detections, we observe 9 and 17 earthquakes in the 12-hour time windows before and after the 2014/07/25 Southeastern Alaska earthquake (β statistic of 2.67), 28 and 43 earthquakes before and after the 2014/08/24 South Napa earthquake (β statistic of 2.83), and 8 vs. 14 earthquakes before and after the 2014/10/14 El Salvador earthquake (β statistic of 2.12). The β statistic exceeding 2 suggest statistically significant triggering following all three mainshocks. We also calculate the Poissonian *p*-values for each event, assuming the null hypothesis of a large *p*-value is consistent with no triggering. We calculate *p*-values of 0.063, 0.039, and 0.11, suggesting triggering at the 94%, 96%, and 89% significance level.

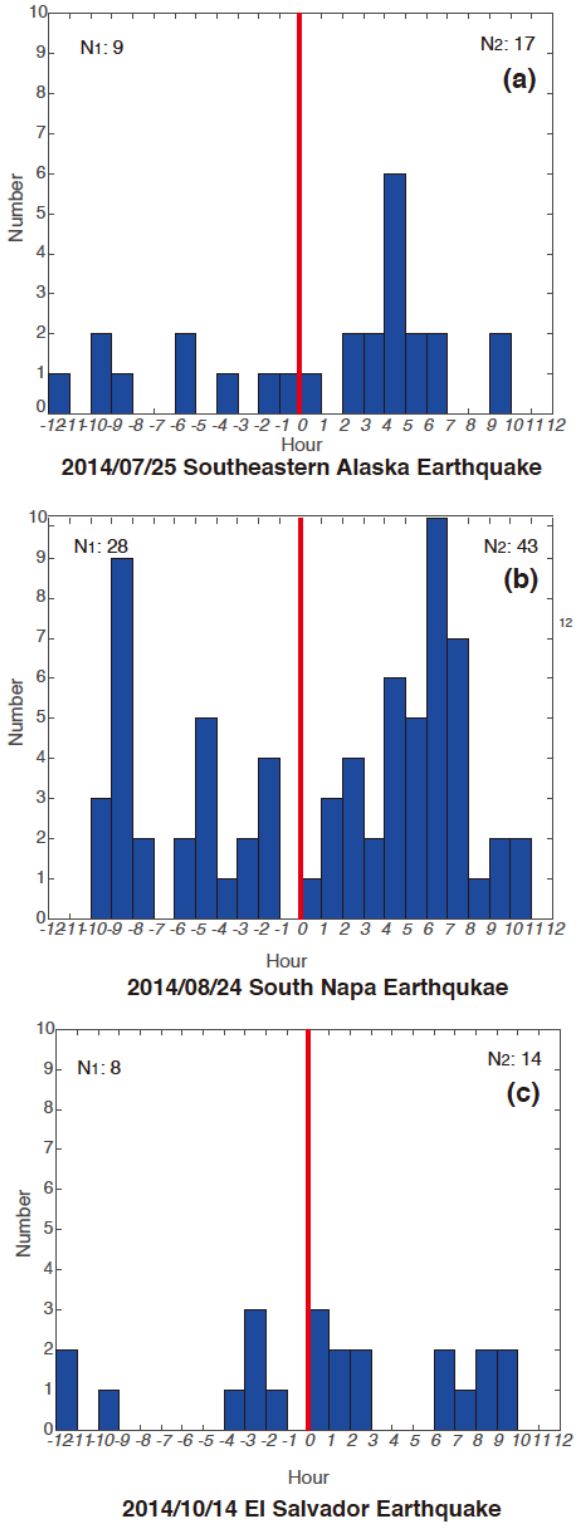

Fig.2.5 Histograms of earthquakes in Alberta detected near TD stations using a matched-filter approach 12 hours before and after mainshocks in Tab.2.3: (a) 2014/07/25 Southeastern Alaska earthquake, (b) 2014/08/24 South Napa earthquake, (c) 2014/10/14 El Salvador earthquake. N1 and N2 represent number of earthquakes before and after mainshocks, respectively. Red lines indicate local arrival time.

2.3.2 Dynamic stresses imposed locally by passing surface waves

In addition to the events detected with the matched-filter approach, the filtered mainshock waveforms show two events that were directly triggered in the Rayleigh wave train of the 2014/10/14 El Salvador mainshock (Events 1 and 2, Fig.2.6). We use the particle motion measured from the waveforms at the times of Events 1 and 2 to estimate the magnitude of triggering stresses (Lay and Wallace, 1995; Brodsky and Prejean, 2005; Peng et al., 2009; Peng et al., 2010; Hill, 2012). We remove the instrument response, and rotate the low-pass filtered waveforms (corner at 10 s) to a great circle path. Using particle velocity values and assuming a crustal shear modulus rigidity (μ) of 32 GPa and estimated Rayleigh wave velocity V_R of 2.85 km/s for Alberta (Gu and Shen, 2015), we calculate the dynamic stress (τ) and strain (ε) using the following equations (Love, 1927) :

$$\tau = \frac{PGV * \mu}{V} \tag{2.4}$$

$$\varepsilon = \frac{PGV}{V_R} \tag{2.5}$$

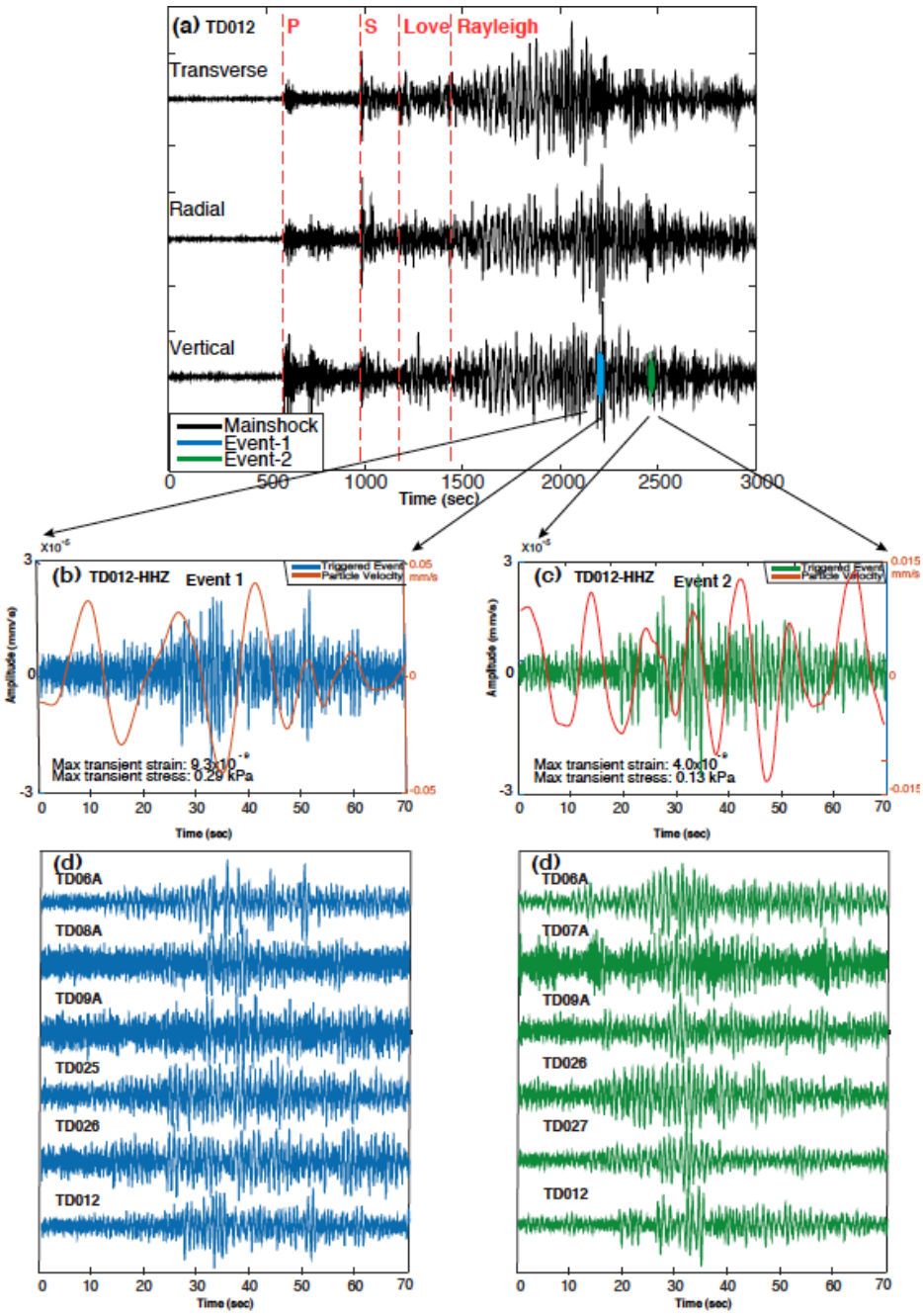

Fig.2.6 Two earthquakes directly triggered in the Rayleigh-wave train of the 2014/10/14 El Salvador mainshock. (a) Mainshock phase arrivals indicated with red dashed lines on original radial, transverse, and vertical waveforms. Blue and green waveforms represent directly triggered events. (b) Directly triggered Event 1 (blue) on station TD012 and mainshock surface wave particle velocities low-pass filtered at 10 s (red). Peak transient dynamic stress is 0.29 kPa. (c) Directly triggered Event 2 (green) on station TD012 and mainshock surface wave particle velocities low-pass filtered at 10 s (red). Peak transient dynamic stress is 0.13 kPa. (d) and (e) Event 1 and Event 2 normalized waveforms, band-pass filtered between 0.9 and 25 Hz, on all stations with visible signal. Red lines in (e) denote P-wave arrival time

picks.

The estimated peak transient stresses during Events 1 and 2 are 0.35 kPa and 0.16 kPa, respectively. Tab.2.3 includes a complete list of peak strains and stresses due to all three 2014 mainshocks. We discuss the particularly small values of peak stresses further in the discussion section.

Mainshocks	Maximum stress	Maximum strain
2014/10/14 M_S 7.3 El Salvador earthquake	0.37 kPa	1.14×10^{-8}
2014/08/24 M_S 6.1 South Napa earthquake	0.46 kPa	1.43×10^{-8}
2014/07/25 M_S 6.0 Southeastern Alaska earthquake	0.41 kPa	1.29×10^{-8}

Tab.2.3 Maximum stress and strain during Rayleigh waves for the three mainshocks in 2014, after the installation of TransAlta Network.

2.3.3 Location of a directly triggered event and focal mechanism solution of the potential induced earthquake

The directly triggered events following the 2014/10/14 El Salvador earthquake are too small to calculate focal mechanisms. Therefore we calculate the focal mechanism for the cataloged 2014/08/09 M_L 3.8 Rocky Mountain House earthquake and compare it to the ambient stress field (World Stress Map Project, GFZ, German Research Center for Geoscience) using the generalized Cut and Paste (gCAP) method, which is based on waveform inversion (Zhao and Helmberger, 1994; Zhu and Helmberger, 1996; Zhu and Ben-Zion, 2013). The moment tensor calculation models P- and/or S-waves in the frequency band of 0.01 – 0.5 Hz, showing a variance reduction of 61.1, with optimal source depth at 2.8

km. (A variance reduction value above 50 is considered a good fit). As shown in Fig.2.7, the 2014/08/09 Rocky Mountain House earthquake occurred on a thrust fault consistent with optimal faulting orientation determined by the regional ambient stress field (Fig.2.7). While preliminary studies of the earthquake suggest no spatial or temporal link to local hydraulic fracturing activity, the shallow focal depth of 2.8 km and history of induced earthquakes in close proximity makes it difficult to definitively rule out.

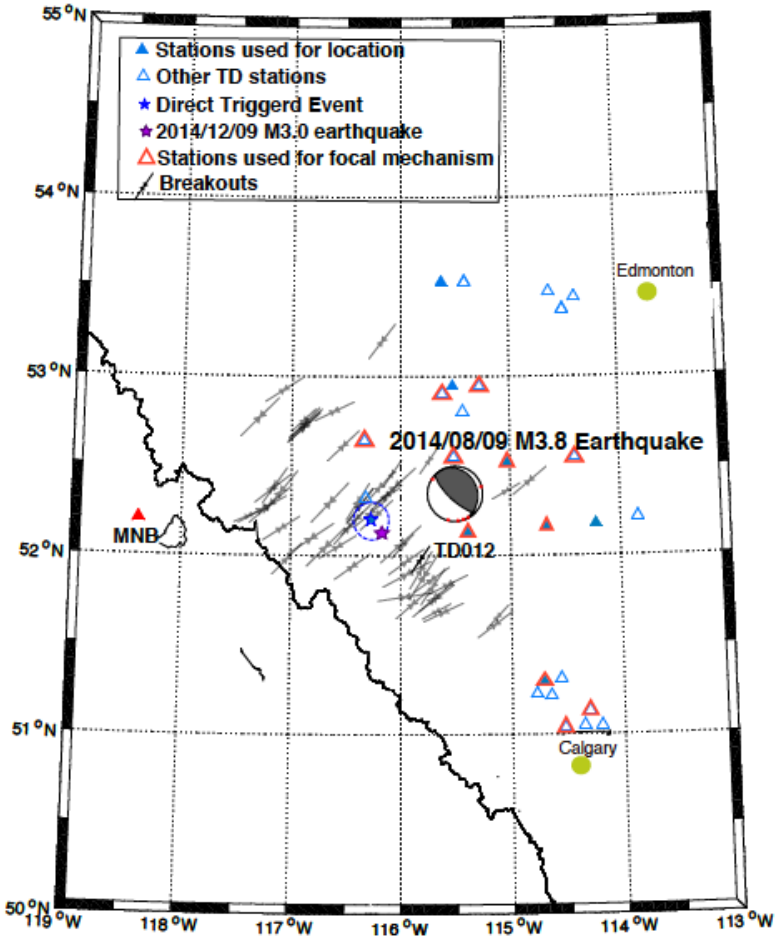

Fig.2.7 Event 2 location (blue star) and error (dashed circle radius 13 km), calculated using select TD stations (blue filled triangles) and NRCan station MNB (red filled triangle). Empty blue triangles are remaining TD stations. M 3.0 earthquake used to estimate Event 1 magnitude shown as a purple star. Triangles outlined in red indicate stations used in gCAP focal mechanism analysis for the 2014/08/09 M 3.8 earthquake. Ambient stress field values

from the World Stress Map project, German Research Centre for Geosciences (Wetmiller, 1986).

Of the two directly triggered events, only Event 2 was large enough to determine a location. We locate Event 2 using the open-source program Hypoinverse and manually picked P-wave arrivals at eight stations with the velocity model for Alberta (Klein, 1978; Chen et al., 2014)(Tab.2.4). Due to the low SNR at many stations, we refine our P-phase picks using cross-correlation lag times relative to the arrival recorded at station TD012 (Fig.2.8). The blue star in Fig.2.7 indicates the epicenter of Event 2.

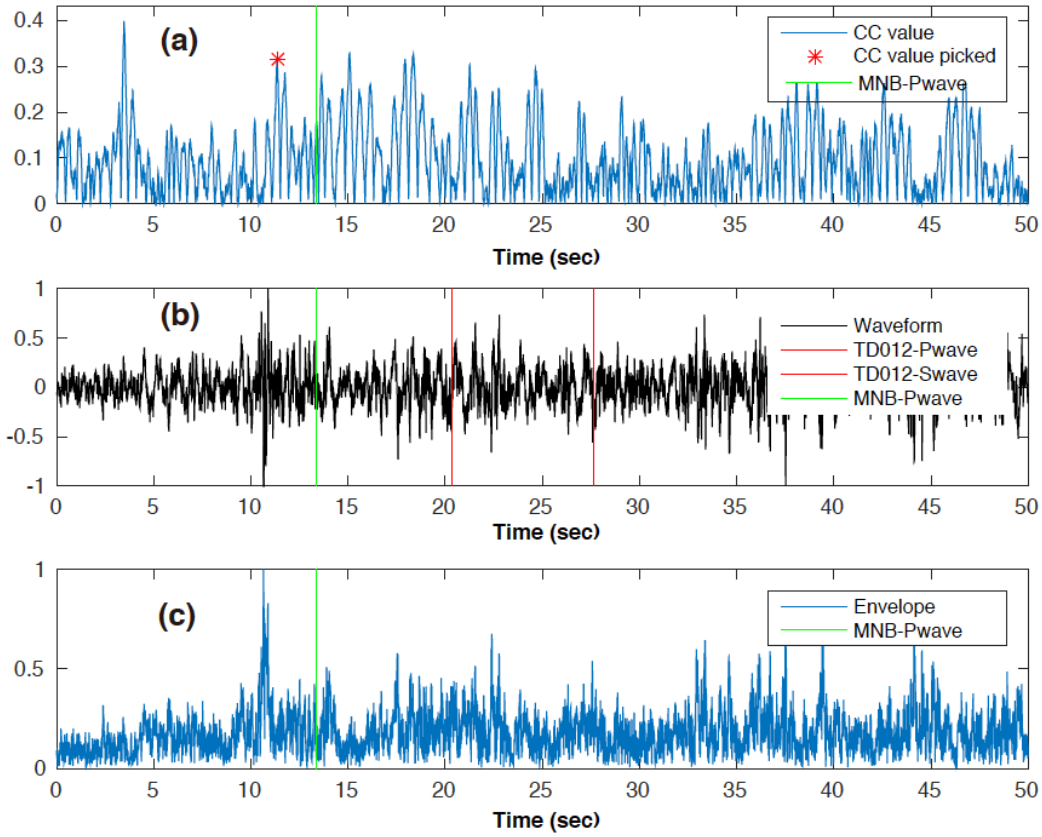

Fig.2.8 The determination of P-wave arrival time for MNB station (a) Absolute cross correlation value between MNB vertical component and TD012 P-wave window. Red star shows the picked P wave arrival time (2 s before) for station MNB. The 2-second lag results

because the P-wave arrival on station TD012 occurs 2 s after the start of the time window. (b) Normalized waveform at station MNB with high-pass filter applied at 1 Hz. (c) Envelope function of station MNB channel HHZ used to check the result of the waveform cross-correlation.

Layer thickness	Vp	Vs	Vp/Vs ratio
2	3.75	2.11	1.97
3	4.37	2.46	2.2
5	5.7	3.21	2.59
5	6	3.38	2.69
5	6.24	3.52	2.77
5	6.42	3.61	2.82
5	6.73	3.79	2.92
5	6.86	3.86	2.96
5	7.15	4.03	3.06
5	7.52	4.2	3.18
5	7.78	4.34	3.26
5	8.05	4.49	3.35
5	8.2	4.52	3.39
5	8.25	4.54	3.41
0	8.27	4.61	3.42

Tab.2.4 Velocity model used with Hypoinverse in the location of Event 2 from station NOR in Alberta.

We calculate the magnitude of Event 2 using the equation below with a nearby cataloged M_L 3.0 earthquake (epicenter shown by a purple star) as the reference event: (Richter, 1935; Gutenberg and Richter, 1956),

$$M_1 - M_2 = log_{10}A_1 - log_{10}A_2. \quad (2.6)$$

Where A is the peak amplitude measured at the station in mm. Assuming a similar source-to-station distance between the two earthquakes and station TD012 gives an estimated magnitude M_L of 1.0 (Fig.2.7).

2.4 Discussion

Figs.2.1b and 2.1c suggest that isolated locations are susceptible to triggering after the TD stations became operational. One reason triggering may appear isolated could be that many potentially triggered earthquakes fall below the completeness threshold. The observations of direct triggering exemplified in Fig.2.6. suggest at least some triggered events have magnitudes of 1 or lower, while the estimated catalog completeness threshold in this region is currently at $M_C \sim 2.8$ (Fig.2.2).

Western Alberta is not a region associated with elevated seismicity similar to British Columbia (a plate boundary) or the St. Lawrence seismic zone, yet it experiences comparable levels of triggering. The fact that dynamic stress perturbations of a fraction of 1 kPa (compared to values of 1 – 5 kPa in other studies) can trigger seismic events strongly suggests local faults hosting triggered events are in a critically stressed state, which could be related to the presence of fluids (Brodsky and Prejean, 2005; Doan et al., 2006; Elkhoury et al., 2006). If permeable structures allow fluid flow into pre-existing fault zones, elevated pore pressure could effectively unclamp faults, resulting in seismic slip on those optimally oriented in the ambient stress field (Brodsky and Prejean, 2005; Hill, 2012). A recent study of the Brazeau seismicity cluster near the Cordel Field, west central Alberta, found a strong temporal correlation of seismic events with monthly operations at a nearby disposal well (Schultz et al., 2014). However, the detailed source characteristics (e.g., fracture energy and stress drop) of

triggered and induced earthquakes are needed in order to quantitatively evaluate the fault stress state and further elucidate physical mechanisms. An interesting question would be to query how triggering propensity changes with time with respect to injection activity, however, given the recent changes installation in the TD network, it is difficult to quantify triggering rates prior to 2014 at the same level. Ideally, such a study would have to be conducted before and after oil and gas production commences.

While two triggered earthquakes occurred during the wave train of the 2014/10/14 El Salvador earthquake, the other two mainshocks in 2014 failed to trigger events during surface wave shaking, despite higher peak dynamic stress amplitudes (Tab.2.3). It is possible that the three mainshocks generated a variation in Coulomb stress changes on the recipient faults, depending on orientation. However, given the difficulties in knowing triggering fault orientation, we look to other factors that may be related to triggering stress magnitudes, such as low-frequency shaking (Brodsky and Prejean, 2005; Peng et al., 2010; Hill, 2012). Fig.2.9 shows the 2014/10/14 El Salvador earthquake has larger amplitude shaking at periods below 20 s, indicating that the long-period waves could be more important for triggering. Several studies also indicate that dilatational strain generated from passing seismic waves can alter pore pressure, flow velocities, and permeability at a given frequency (Brodsky et al., 2003; Elkhoury et al., 2011; Candela et al., 2014; Candela et al., 2015). Enhanced permeability could drive flow flushing temporary blockages from fractures, thereby redistributing the pore pressure and reducing the effective normal stress, bringing faults to failure.

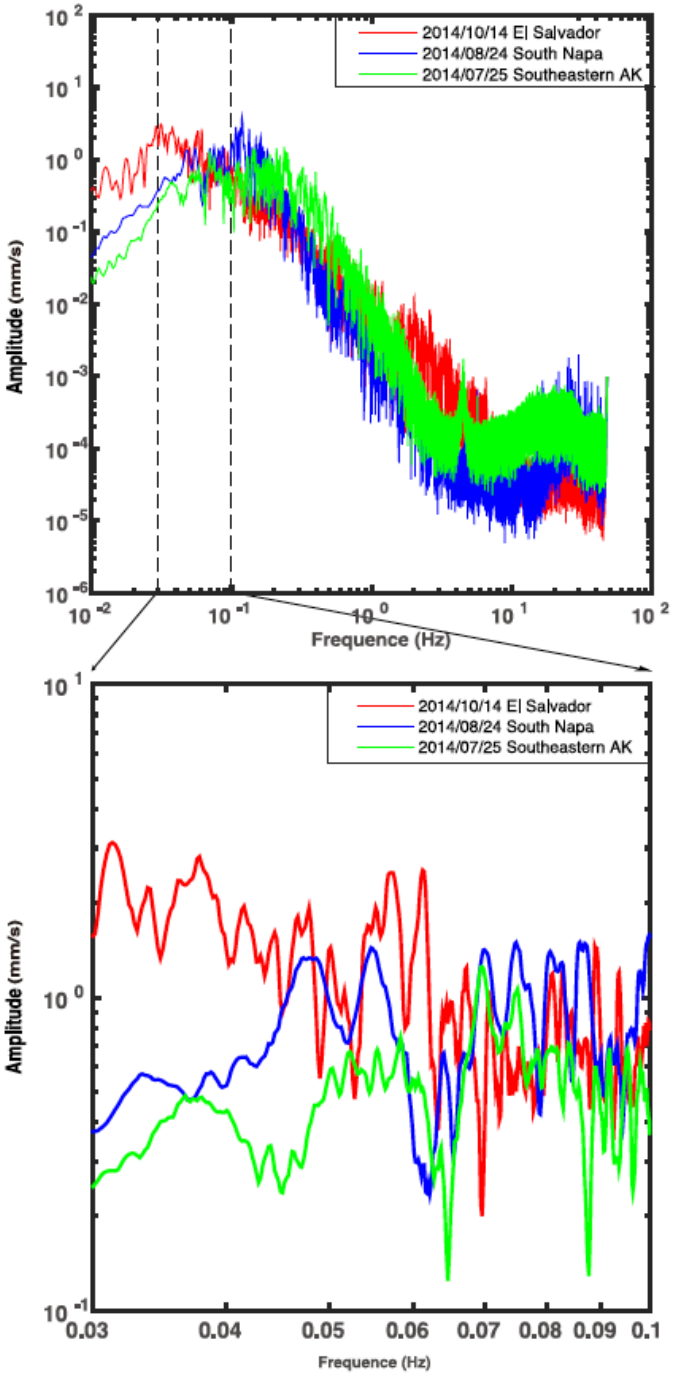

Fig.2.9 Spectrum of the vertical component at TD012 station for the three mainshocks listed in Tab.2.3. (a) Spectrum of the three mainshocks with frequencies from 0.001 Hz to 50 Hz. (b) Smoothed spectrum of the three mainshocks with frequencies from 0.03 Hz to 0.1 Hz.

We also examine the duration and cumulative energy of the mainshocks to see if they provide plausible explanations for triggering consistent with the observations (Hill et al., 1993;

Sturtevant et al., 1996; Brodsky et al., 2000). Fig.2.10a shows that the two directly triggered earthquakes occur nearly 1800 s and 2000 s after the onset of shaking from the El Salvador earthquake, while shaking from the other two mainshocks lasts less than 1500 s. Thus we can not exclude duration as a criterion for direct triggering. Fig.2.10b indicates the 2014/08/24 South Napa mainshock has the highest cumulative energy and an absence of directly triggered events, suggesting cumulative energy may not be criterion for triggering.

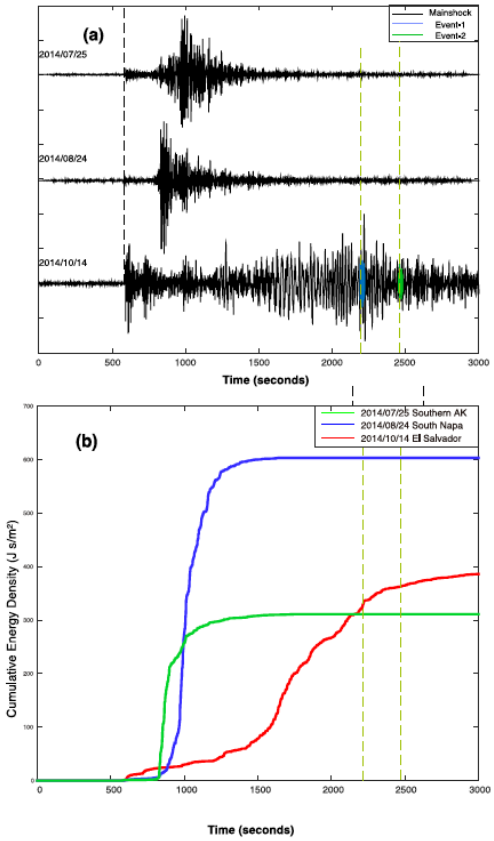

Fig.2.10 Duration and cumulative energy density of triggering mainshocks. The two dashed lines represent the origin time of two directly triggered events. (a) The normalized vertical component of three mainshocks and the two directly triggered events for 2014/10/14 mainshock. (b) Comparison of cumulative energy of triggering mainshocks. Energy is calculated from the equation $E = \rho c \int \dot{u}^2 dt$, where ρ is the local rock density, c is the phase velocity, and $\dot{u}$ is the particle velocity.

The observed stress perturbations associated with direct triggering are lower than typical ranges of 1-5 kPa observed in other studies (Brodsky and Prejean, 2005; Aiken and Peng, 2014). One reason could be that other studies focus on geothermal and volcanic areas often in extensional or trans-tensional tectonic regions while our study focuses on fluid injection (Fig.2.1b and c) and gas extraction sites in a compressional tectonic regime (Wetmiller, 1986). This study provides only limited observations of triggering, but a correlation between triggering capability and tectonic regime has been suggested in previous work (e.g., Harrington and Brodsky, 2006). Alternatively, the matched-filter approach could be more efficient at finding small, triggered earthquakes, if earthquake magnitude is somehow correlated with triggering stresses as suggested by Hill et al. (1993). Although the triggering stresses/strains observed here are small, they are consistent with observed cases of triggering with strain as low as 3×10^{-9} (equivalent to 0.1 kPa triggering stress)(van der Elst and Brodsky, 2010).

2.5 Conclusions

In this chapter, we provide evidence of remote dynamic triggering in isolated areas of Canada using catalog data, and in Alberta using both catalog and waveform data. Our catalog study suggests that much of the observed propensity for triggering occurs near active faults, but that in some cases, triggering occurs outside of active seismic zones. The propensity for triggering may be correlated with the propensity to induce earthquakes. A more localized waveform study of triggering near the TransAlta network in Alberta area shows statistically significant increases in seismicity in 2014, after station coverage increased significantly.

The waveform study also provides two clear examples of directly triggered events within

the surface wave train of the 2014/10/14 El Salvador earthquake. Transient stresses measured at the time of triggering were 0.35 kPa and 0.16 kPa, and transient dynamic strain amplitudes were 9.3×10^{-9} and 4.0×10^{-9}, respectively. Although the observed dynamic stress and strain amplitudes are lower than those in many previous studies, the dynamic strain is 1 to 3 times of 3×10^{-9}, which is interpreted to be an observational limit of strain perturbation for earthquake triggering in California (van der Elst and Brodsky, 2010). The triggering sensitivity to such low strain and stress perturbations suggests pre-existing faults in the study area may be critically stressed. Finally, the waveform study of triggered events suggests long-period shaking below 20 s may be more important for triggering than cumulative shaking or cumulative energy.

2.6 References for Chapter 2

Aiken, C., & Peng, Z. (2014). Dynamic triggering of microearthquakes in three geothermal/volcanic regions of California. *Journal of Geophysical Research: Solid Earth, 119*(9), 6992-7009. doi: 10.1002/2014jb011218

Ben-Menahem, A., & Singh, S. J. (2012). *Seismic waves and sources*: Courier Corporation.

Beresnev, I. A., Wen, K. L., & Yeh, Y. T. (1995). Nonlinear Soil Amplification - Its Corroboration in Taiwan. *Bulletin of the Seismological Society of America, 85*(2), 496-515.

Brodsky, E. E., Karakostas, V., & Kanamori, H. (2000). A new observation of dynamically triggered regional seismicity: Earthquakes in Greece following the August, 1999 Izmit, Turkey earthquake. *Geophysical Research Letters, 27*(17), 2741-2744. doi: 10.1029/2000gl011534

Brodsky, E. E., & Prejean, S. G. (2005). New constraints on mechanisms of remotely triggered seismicity at Long Valley Caldera. *Journal of Geophysical Research-Solid Earth, 110*(B4). doi: 10.1029/2004jb003211

Brodsky, E. E., Roeloffs, E., Woodcock, D., Gall, I., & Manga, M. (2003). A mechanism for sustained groundwater pressure changes induced by distant earthquakes. *Journal of*

Geophysical Research-Solid Earth, 108(B8). doi: 10.1029/2002jb002321

Brodsky, E. E., & van der Elst, N. J. (2014). The Uses of Dynamic Earthquake Triggering. *Annual Review of Earth and Planetary Sciences, Vol 42, 42*, 317-339. Doi 10.1146/Annurev-Earth-060313-054648

Candela, T., Brodsky, E. E., Marone, C., & Elsworth, D. (2014). Laboratory evidence for particle mobilization as a mechanism for permeability enhancement via dynamic stressing. *Earth and Planetary Science Letters, 392*, 279-291. Doi 10.1016/J.Epsl.2014.02.025

Candela, T., Brodsky, E. E., Marone, C., & Elsworth, D. (2015). Flow rate dictates permeability enhancement during fluid pressure oscillations in laboratory experiments. *Journal of Geophysical Research: Solid Earth*, 120.4 (2015): 2037-2055.

Chen, Y., Gu, Y. J., Dokht, R. H., & Sacchi, M. (2014). Crustal imprints of Precambrian orogenesis in western Laurenti. *Journal of Geophysical Research: Solid Earth* 120.10 (2015): 6993-7012.

Crotwell, H. P., Owens, T. J., & Ritsema, J. (1999). The TauP Toolkit: Flexible seismic travel-time and ray-path utilities. *Seismological Research Letters, 70*(2), 154-160.

Elkhoury, J. E., Niemeijer, A., Brodsky, E. E., & Marone, C. (2011). Laboratory observations of permeability enhancement by fluid pressure oscillation of in situ fractured rock. *Journal of Geophysical Research-Solid Earth, 116*(B2). doi: Artn B02311 Doi 10.1029/2010jb007759

Gomberg, J., & Davis, S. (1996). Stress strain changes and triggered seismicity at The Geysers, California. *Journal of Geophysical Research-Solid Earth, 101*(B1), 733-749. doi: 10.1029/95jb03250

Gomberg, J., Reasenberg, P. A., Bodin, P., & Harris, R. A. (2001). Earthquake triggering by seismic waves following the Landers and Hector Mine earthquakes. *Nature, 411*(6836), 462-466. doi: 10.1038/35078053

Gutenberg, B., & Richter, C. F. (1956). Magnitude and energy of earthquakes. *Annals of Geophysics, 9*(1), 1-15.

Harrington, R. M., & Brodsky, E. E. (2006). The absence of remotely triggered seismicity in Japan. *Bulletin of the Seismological Society of America, 96*(3), 871-878. doi: 10.1785/0120050076

Hill, D. P. (2008). Dynamic stresses, Coulomb failure, and remote triggering. *Bulletin of the Seismological Society of America, 98*(1), 66-92. doi: 10.1785/0120070049

Hill, D. P., & Prejean, S. G. (2007). 4.09 - Dynamic Triggering. In G. Schubert (Ed.), *Treatise on Geophysics* (pp. 257-291). Amsterdam: Elsevier.

Hill, D. P., Reasenberg, P. A., Michael, A., Arabaz, W. J., Beroza, G., Brumbaugh, D., Brune, J. N., Castro, R., Davis, S., Depolo, D., Ellsworth, W. L., Gomberg, J., Harmsen, S., House, L., Jackson, S. M., Johnston, M. J., Jones, L., Keller, R., Malone, S., Munguia, L., Nava, S., Pechmann, J. C., Sanford, A., Simpson, R. W., Smith, R. B., Stark, M., Stickney, M., Vidal, A., Walter, S., Wong, V., & Zollweg, J. (1993). Seismicity remotely triggered by the magnitude 7.3 Landers, California, earthquake. *Science, 260*(5114), 1617-1623. doi: 10.1126/science.260.5114.1617

Hough, S. E. (2005). Remotely triggered earthquakes following moderate mainshocks (or, why California is not falling into the ocean). *Seismological Research Letters, 76*(1), 58-66.

Klein, F. W. (1978). *Hypocenter locations program HYPOINVERSE*: US Department of the Interior, Geological Survey.

Lay, T., & Wallace, T. C. (1995). *Modern global seismology* (Vol. 58): Academic press.

Love, A. (1927). A treatise on the mathematical theory of elasticity. *Cambridge university press.*

Matthews, M. V., & Reasenberg, P. A. (1988). Statistical-Methods for Investigating Quiescence and Other Temporal Seismicity Patterns. *Pure and Applied Geophysics, 126*(2-4), 357-372. doi: 10.1007/Bf00879003

Nikiforuk, A. (2015). Did Alberta Just Break a Fracking Earthquake World Record?| The Tyee.

Peng, Z. G., Vidale, J. E., Wech, A. G., Nadeau, R. M., & Creager, K. C. (2009). Remote triggering of tremor along the San Andreas Fault in central California. Journal of Geophysical Research-Solid Earth, 114(B7). doi: 10.1029/2008jb006049

Peng, Z., Hill, D. P., Shelly, D. R., & Aiken, C. (2010). Remotely triggered microearthquakes and tremor in central California following the 2010Mw8.8 Chile earthquake. *Geophysical Research Letters, 37*(24). doi: 10.1029/2010gl045462

Prejean, S., Hill, D., Brodsky, E. E., Hough, S., Johnston, M., Malone, S., Oppenheimer, D., Pitt, A., & Richards-Dinger, K. (2004). Remotely triggered seismicity on the United States west coast following the Mw 7.9 Denali Fault earthquake. *Bulletin of the Seismological Society of America, 94*(6B), S348-S359.

Reasenberg, P. A., & Simpson, R. W. (1992). Response of regional seismicity to the static

stress change produced by the loma prieta earthquake. *Science, 255*(5052), 1687-1690. doi: 10.1126/science.255.5052.1687

Richter, C. F. (1935). An instrumental earthquake magnitude scale. *Bulletin of the Seismological Society of America, 25*(1), 1-32.

Schultz, R., & Gu, Y. (2012). *Micro-seismicity in Alberta recorded by the Canadian Rockies and Alberta Network.* Paper presented at the AGU Fall Meeting Abstracts.

Schultz, R., Stern, V., & Gu, Y. J. (2014). An investigation of seismicity clustered near the Cordel Field, west central Alberta, and its relation to a nearby disposal well. *Journal of Geophysical Research: Solid Earth, 119*(4), 3410-3423.

Shelly, D. R., Beroza, G. C., & Ide, S. (2007). Non-volcanic tremor and low-frequency earthquake swarms. *Nature, 446*(7133), 305-307. doi: 10.1038/nature05666

Stark, M. A., & Davis, S. D. (1996). Remotely triggered microearthquakes at The Geysers geothermal field, California. *Geophysical Research Letters, 23*(9), 945-948. doi: 10.1029/96gl00011

Sturtevant, B., Kanamori, H., & Brodsky, E. E. (1996). Seismic triggering by rectified diffusion in geothermal systems. *Journal of Geophysical Research-Solid Earth, 101*(B11), 25269-25282. doi: 10.1029/96jb02654

van der Elst, N. J., & Brodsky, E. E. (2010). Connecting near-field and far-field earthquake triggering to dynamic strain. *Journal of Geophysical Research, 115*(B7). doi: 10.1029/2009jb006681

van der Elst, N. J., Savage, H. M., Keranen, K. M., & Abers, G. A. (2013). Enhanced remote earthquake triggering at fluid-injection sites in the midwestern United States. *Science, 341*(6142), 164-167. doi: 10.1126/science.1238948

Wetmiller, R. J. (1986). Earthquakes near Rocky Mountain House, Alberta, and their relationship to gas production facilities. *Canadian Journal of Earth Sciences, 23*(2), 172-181.

Zhao, L.-S., & Helmberger, D. V. (1994). Source estimation from broadband regional seismograms. *Bulletin of the Seismological Society of America, 84*(1), 91-104.

Zhu, L. P., & Ben-Zion, Y. (2013). Parametrization of general seismic potency and moment tensors for source inversion of seismic waveform data. *Geophysical Journal International, 194*(2), 839-843. doi: 10.1093/Gji/Ggt137

Zhu, L. P., & Helmberger, D. V. (1996). Advancement in source estimation techniques using broadband regional seismograms. *Bulletin of the Seismological Society of*

America, 86(5), 1634-1641.

Chapter 3

Remote Dynamic Triggering of Earthquakes in Three Unconventional Canadian Hydrocarbon Regions Based on a Multiple-station Matched-filter Approach

3.1 Introduction

The Earth's crust is permeated with faults, portions of which are critically stressed and capable of hosting earthquakes triggered by small transient stresses (e.g., Hill et al., 1993; Brodsky et al., 2000; Zoback and Zoback, 2002; Hill, 2012). Studying dynamic triggering provides an opportunity to isolate clues about the stress state on a fault (Brodsky and Prejean, 2005; van der Elst et al., 2013; Aiken and Peng, 2014), and to isolate the mechanism(s) of earthquake nucleation by observing the minimum value of stress perturbation required to trigger fault failure. Some studies suggest that the values of transient stress needed to initiate an earthquake are comparable to tidal stresses (e.g., 5-10 kPa from Aiken and Peng, 2014). Recent studies suggest areas with elevated seismicity rates related to fluid injection could be more susceptible to dynamic triggering, as ambient fluid pressure may remain high, priming fault systems for failure (van der Elst et al., 2013; Wang et al., 2015). The diagnostic analysis of triggering near injection sites, together with the investigation of induced seismicity, could help develop operational procedures to reduce anthropogenically induced seismic activity, as well as help us better understand what mechanisms are responsible for triggering fault rupture.

Many sites in Canada currently exhibit elevated seismicity compared to historical rates as

the result of fluid injection activity (Atkinson et al., 2016). For instance, the average number of Natural Resources Canada (NRCan) cataloged earthquakes per year with magnitude > 2 in northeastern British Columbia and western Alberta in the time period from 2001 to 2003 was 12, compared with an average of 31 over the year 2010 to 2012. In contrast to the central United States, where induced seismicity has been more closely linked to disposal wells (e.g., Keranen et al., 2014; Barbour et al., 2017; Yeck et al., 2017), the sharp increase in earthquakes in the Western Canada Sedimentary Basin (WCSB) is more likely related to hydraulic fracturing (HF)(Schultz et al., 2015; Atkinson et al., 2016; Zhang et al., 2016). In efforts to monitor earthquakes induced by hydraulic fracturing activity, NRCan increased seismic station coverage from March 2013 in regions where hydraulic fracturing activity has been ongoing and/or ramping up (See Data and Resources). While remote dynamic earthquake triggering may be likely in broad regions that experience high rates of induced earthquakes, it has mainly been examined at localized sites in Canada. For example, Wang et al., (2015) examined triggering at a single site in western Alberta using a single-station matched filter approach, which limits earthquake detections to the area in close proximity to the station. The increased NRCan seismic station coverage since 2013 provides a unique opportunity for studying remote dynamic earthquake triggering at a regional scale near injection sites.

In this study, we search for dynamic triggering in three regions in Canada hosting active hydraulic fracturing in northeastern British Columbia and western Alberta (BCAB), Northwest Territories (NWT) and New Brunswick (NB) (Blue box in Fig.3.1), surrounding global mainshocks between 2013 and 2015. Our study areas in BCAB and NWT are smaller

sub-basins contained in the broader (i.e., Montney Basin, Horn River Basin and Liard Basin), and in NB is primarily located within the Moncton sub-basin, a composite, post-Acadian internal successor basin (Peter, 1994). The search for triggering is composed of a two-fold approach that identifies direct evidence of triggering in the surface wave train of triggering mainshocks using waveform data, and then identifies changes in earthquake rates in a time window surrounding the mainshocks using an enhanced earthquake catalog. The primary objectives of this study are to 1) determine if the three regions are susceptible to remote dynamic triggering over the spatial scale of basins, and 2) if triggering occurs, to infer characteristics regarding the ambient stress state, the physical factors influencing triggering, the correlation with tectonic regime, and the implications for triggering mechanism(s).

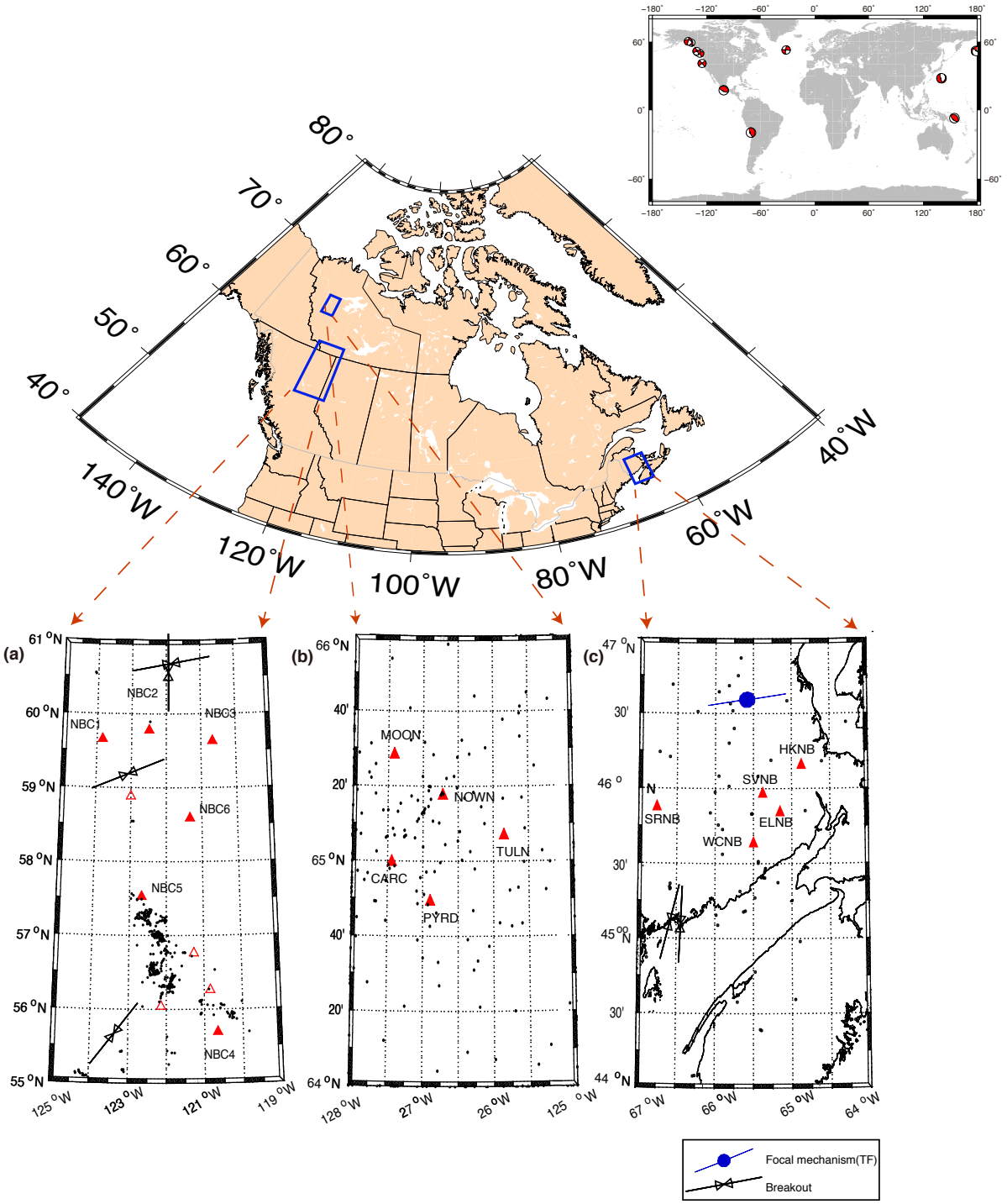

Fig.3.1 Locations of three regions (blue boxes) used in this study in (a) northeast British Columbia and western Alberta (BCAB), (b) Northwest Territories (NWT), and (c) New Brunswick (NB). NRCan seismic stations shown as red triangles, solid symbols represent stations used in this study. NRCan cataloged seismicity from 2013-2015 shown with black dots. Black arrows indicate regional compressional stress orientations in all three regions and the solid blue circle in (c) indicates the P-axis orientation inferred from an earthquake focal

mechanism solution in NB (World Stress Map project, GFZ, German Research Centre for Geosciences). Top right shows the 12 remote mainshocks considered in this study (see Tab.3.1).

Mainshock	Number
Queen Charlotte Island earthquake, M_s 6.2, 2013/09/13 20:19:06	1
Off Coast of Northern CA earthquake, M_s 6.7, 2014/03/10 05:18:13	2
Near Coast of Chile, Iqique, M_s 7.9, 2014/04/01 23:46:48	3
Guerrero earthquake, M_s 7.4, 2014/04/18 14:27:24	4
Solomon Islands earthquake, M_s 7.8, 2014/04/19 13:47:43	5
Vancouver Island earthquake, M_s 6.5, 2014/04/24 03:10:12	6
Southeastern Alaska earthquake, M_s 6, 2014/06/04 11:58:56	7
Rat Islands earthquake, M_s 7, 2014/06/23 20:53:09	8
Southeastern Alaska earthquake, M_s 6.3, 2014/07/17 11:49:33	9
Northern Mid-Atlantic earthquake, M_s 6.9, 2015/02/13 18:59:14	10
Queen Charlotte Islands earthquake, M_s 6.5, 2015/04/24 13: 56:1 5	11
Bonin Islands, Japan Reg eartqhuake, M_s 7.8, 2015/05/ 30 11:23:03	12

Tab.3.1 Candidate triggering mainshocks with origin times referred to in the text, and found in Fig.3.6, Fig3.7, Fig.3.9, Fig.3.10, Tab.3.2 and Tab.3.3.

In the following, we first present our data and methods for detecting cases of direct triggering in the filtered mainshock waveforms, and then present the catalog-based approach to assessing triggering. In the catalog-based approach, we first detail the method for building an enhanced earthquake catalog using a multiple-station matched-filter (MMF) approach, as well as describe the two statistical methods used to evaluate seismicity rate change, namely, a *p*-value test on the null hypothesis of no rate change, and a test that evaluates rate changes via inter-event times. We then present the observations of triggering in each of the shale regions and discuss the physical factors associated with triggering in the context of the results.

Interpretation based on geologic context and production history will be discussed, followed by the conclusions of the study. We will show that the observations presented here, combined with modeling results from a related study (Deng et al., 2016), have implications for the mechanisms of immediate versus delayed triggering. Namely, that for tight shale formations, the rock matrix stress may be the dominant factor causing immediate triggering, and that pore pressure diffusion may dominate in cases of delayed triggering.

3.2 Candidate mainshocks and waveform-based identification of direct triggering

We begin by identifying candidate triggering mainshocks from the global International Seismological Center (ISC) catalog with depths < 100 km and surface wave magnitudes of M_S > 6 occurring during the time period of increased station coverage (2013-2015). We choose the above magnitude and depth threshold values based on previous studies that suggest remote earthquake triggering can be more easily observed for mainshocks with surface magnitudes > 6, primarily because they generate higher local Peak Ground Velocity (PGV) at potential triggering sites, a favorable condition for triggering, and because surface wave shaking is presumed the main cause for dynamic triggering (e.g., Hill et al., 1993; Brodsky et al., 2000; Hill and Prejean, 2007). Additionally, cases of dynamic triggering are commonly associated with the transient stresses imparted by the passing surface waves of triggering mainshocks, and shallow-focus mainshocks (with depths < 100 km) tend to generate more surface wave energy (e.g., Stark and Davis,1996; Gomberg and Davis, 1996; Wen et al., 1996). We further restrict candidate mainshocks to those with an estimated PGV of 0.01 cm/s locally in the three regions shown in Fig.3.1. The PGV threshold is chosen based

on other studies showing similarly small shaking amplitudes (i.e., transient stresses) that caused dynamic triggering (e.g., Brodsky and Prejean, 2005; Aiken and Peng, 2014; Wang et al., 2015). The following empirical ground motion regression provides an estimate of PGV (Lay and Wallace, 1995; Aki and Richards, 2002):

$$Log_{10}A_{20} = M_S - 1.66Log_{10}\delta - 2 \quad (3.1)$$

$$PGV \approx \frac{2\pi A_{20}}{T} \quad (3.2)$$

where M_s is surface wave magnitude, δ is epicenter-station distance in degrees, and A_{20} is the surface wave amplitude for phases with period T = 20 s. In total, five mainshocks satisfy the above criteria for BCAB, six for NWT and three for NB, as listed in Tab.3.1.

Once candidate mainshocks are identified, we begin searching for evidence of triggering using a waveform-based approach, which aims to detect local earthquakes directly triggered by the transient stress oscillations imparted by the passing surface waves of the triggering mainshocks. In the case that local events are triggered during surface wave shaking, they are often not visible in the raw waveforms recorded at a given station, but become visible once the high-amplitude, low-frequency energy from the mainshock surface waves is removed with a high-pass filter. Waveform data for the BCAB region are available from the Incorporated Research Institutions for Seismology (IRIS) data archive, while data for the NWT and NB areas are archived by NRCan, and are available upon request.

We use high-pass-filtered (1 Hz) waveforms in 8000-second time windows before and after the mainshock origin time (roughly two hours surrounding each mainshock signal), and visually inspect for uncataloged earthquakes, both before (assumed “background” seismicity) and after the mainshock body wave arrivals (assumed “directly triggered” seismicity). If

direct triggering is observed, it is possible to estimate the triggering stress by converting the particle motion resulting from the surface wave shaking to stress using the phase velocity in the following equation (Love, 1927),

$$\tau = \frac{PGV \times \mu}{V_R} \tag{3.3}$$

where PGV is observed particle velocity, and the crustal shear modulus (μ) is assumed at 32 GPa. We also assume a Raleigh wave velocity value V_R of 2.85 km/s for BCAB and NWT, and 3.1 km/s for NB, based on previous studies (Hughes and Luetgert, 1991; Gu and Shen, 2015).

Fig.3.2 shows the observed examples of local earthquakes detected in the high-pass filtered 8000-second time windows for each region. Using Eq.3.3 to convert the observed particle velocities to stresses, we infer maximum direct triggering stresses of 1.7 kPa, 1.1 kPa and 0.35 kPa in BCAB, NWT and NB, respectively, as listed in Tab.3.2. Tab.3.2 also includes the range of stress perturbation values imparted by the mainshock surface waves for all the events during which directly triggered local earthquakes were observed. In addition to the events observed during the passage of surface waves, additional local triggered events occurred in all three regions within the 8000-second (roughly 2-hour) time window.

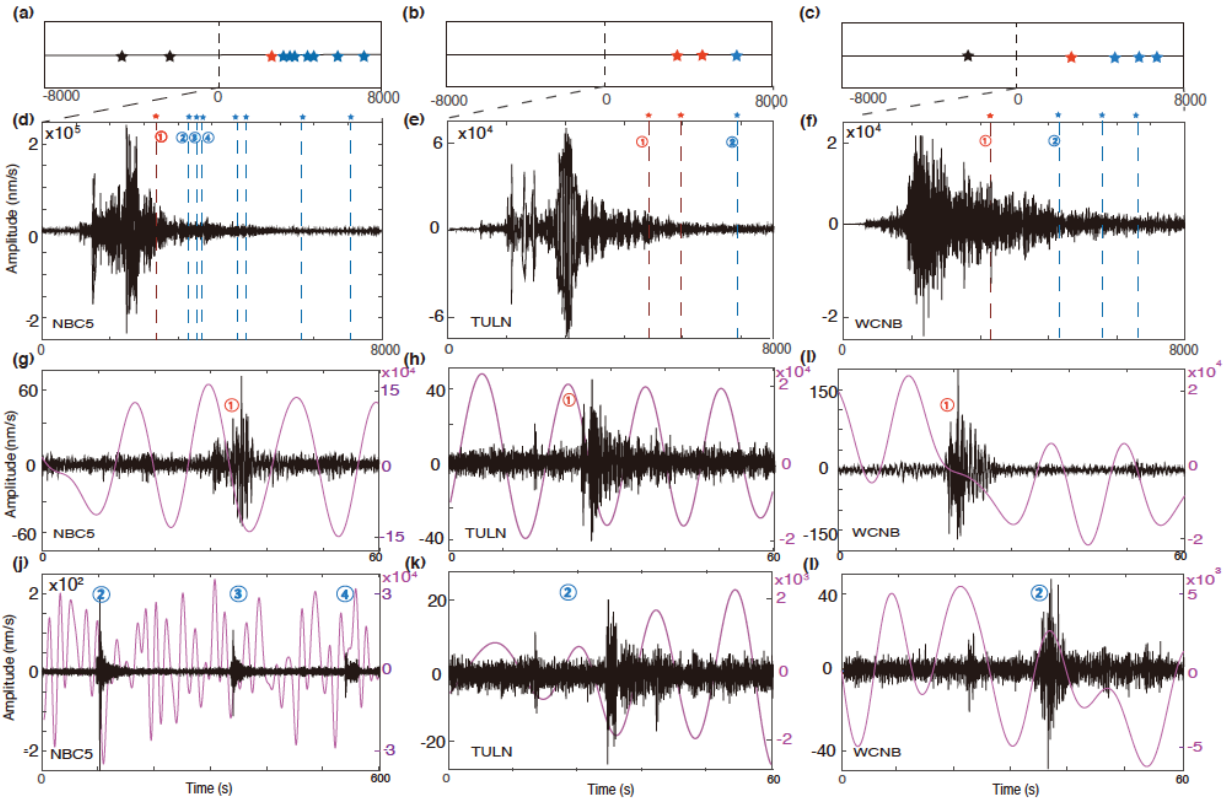

Fig.3.2 Examples of manually detected earthquakes in the 8000-second windows before and after the onset time of mainshocks (shown in (d)(e)(f)), and the left, middle, and right columns correspond to the 2014/04/01 mainshock for BCAB, the 2014/04/19 mainshock for NWT, and the 2014/04/18 mainshock for NB, respectively. (a)(b)(c)(d)(e)(f) show times of detected earthquakes. Black stars in (a)(b)(c) denote earthquakes prior to the mainshock, red stars denote earthquakes in the surface wave train of the mainshock, and blue stars denote the earthquakes after surface shaking has died down. Waveforms in the bottom two rows are high band-pass filtered at 1 Hz and show earthquakes marked with numbers in (d)(e)(f). Purple waveforms in (g)-(l) are the 0.1 Hz low band-pass filtered waveforms from the mainshock.

British Columbia and Alberta			Northwest Territories			New Brunswick		
Mainshock number	Number of directly triggered earthquakes	Range of observed stresses	Mainshock number	Number of directly triggered earthquakes	Range of observed stresses	Mainshock number	Number of directly triggered earthquakes	Range of observed stresses
1	-	-	4 & 5	2	0.2-0.22 kPa	3	2	0.32-0.35 kPa
2	1	1.7 kPa	6	-	-	4	1	0.2 kPa
3	-	-	7	-	-	10	-	-
11	-	-	8	1	1.1 kPa	-		
12	-	-	9	-	-	-		

Tab.3.2 Number of directly triggered earthquakes and the observed range of inferred transient stresses imparted by each associated candidate mainshock based on observed local particle velocity calculated using Equation 3.3. Mainshock number corresponds to Tab.3.1.

3.3 Catalog-based method to identify triggering

As remotely triggered earthquakes are typically small (M < 2), we employ an improved MMF (multiple-station matched-filter) detection method on continuous waveform data to build an enhanced earthquake catalog and decrease the detection threshold magnitude. In contrast to using a single station matched-filter approach (e.g., Wang et al., 2015), the MMF method enables searching for a larger number of un-cataloged earthquakes over a wider spatial area. The enhanced catalog uses all stations shown by filled symbols in Fig.3.1 to detect as many earthquakes as possible at each site on a regional scale. While the magnitudes of the additionally detected earthquakes (relative to the existing catalog) can be constrained using the relative amplitudes between new detections and template (i.e., cataloged), in many

cases, it is impossible to robustly constrain locations for additional detections, because the small magnitudes make clear phase arrival picks possible only on a limited number of stations. However, the moveout and waveform character is similar for the additional detections to the template events, suggesting that additional detections must be within close proximity to templates, and local to the region. We therefore assume that additional detections are co-located (within error) with their respective templates, an approach taken in other studies using the MMF approach (e.g., van der Elst et al., 2013; Skoumal et al., 2015).

3.3.1 Enhanced catalog using MMF detection

The MMF detection method consists of the following two steps. First, we build template events using NRCan cataloged earthquakes in each study region. Second, we search for uncataloged local earthquakes by cross-correlating the waveforms of template events to the continuous waveform during a maximum period of 10 days before and after each of the candidate mainshocks at each station. A time window of 10 days allows establishing whether any delayed triggering has occurred while simultaneously reducing the risk of erroneously considering any event rate fluctuations related to potential nearby injection activity. In some cases outside of BCAB, time windows of 5 days were considered as a result of data availability or temporally associated mainshocks. However, we will show in the Physical factors that influence triggering Section that time windows of 5 days are sufficient to detect seismicity increases in the study areas considered here.

The process of building templates consists of first removing earthquakes recorded at less than 3 stations among the cataloged events. The reason is twofold. First, empirical tests show

that it reduces the number of false detections with the MMF method by retaining templates with higher signal-to-noise ratios (SNRs). Second, it allows us to locate template events, and thereby assume similar locations for MMF detected events with similar waveforms that are too small to locate. We then group the remaining events into families based on waveform similarity on the East-West component at a single station, e.g., NBC5 for BCAB, where correlation coefficient values exceed 0.5 determined using the GISMO tool box (Reyes and West, 2011). Station NBC5 has the best SNR and most complete record during the study period. Next, the single representative earthquake with the highest SNR per family is selected as a template waveform, again using only the East-West component in the detection. The clustering of similar events reduces the possible number of template events from 356 to 145 for BCAB and from 343 to 52 for NWT. Given that only 32 earthquakes are cataloged for NB during the time period of our study, we use all events as templates. Figs.3.3 and 3.4 illustrate the clustering of event families and template identification. We also test several bandpass filters and template time-window lengths to optimize the detection. Empirical tests show that the MMF method works optimally in different frequency bands for the three sedimentary regions. For example, we detect the highest number of events by filtering the template waveforms between 5–15 Hz in BCAB and NB, and 1-15 Hz in NWT, while filtering the NWT templates in the 5-15 Hz band removed too much of the energy. We attribute the differences in frequency sensitivity to potentially different lithology (i.e., sandstone beds at BCAB and limestone beds at NWT (Yose et al., 2001; Zonneveld et al., 2010)), as well as site and travel path effects due to differing station geometry. We find a 40-s cross-correlation time window (20 s before and after S-wave arrival) for BCAB and NWT, and a 30 s window for

NB (15 s before and after S-wave arrival) work best to include a distinct S-wave signal and a weak P-wave signal on the horizontal components.

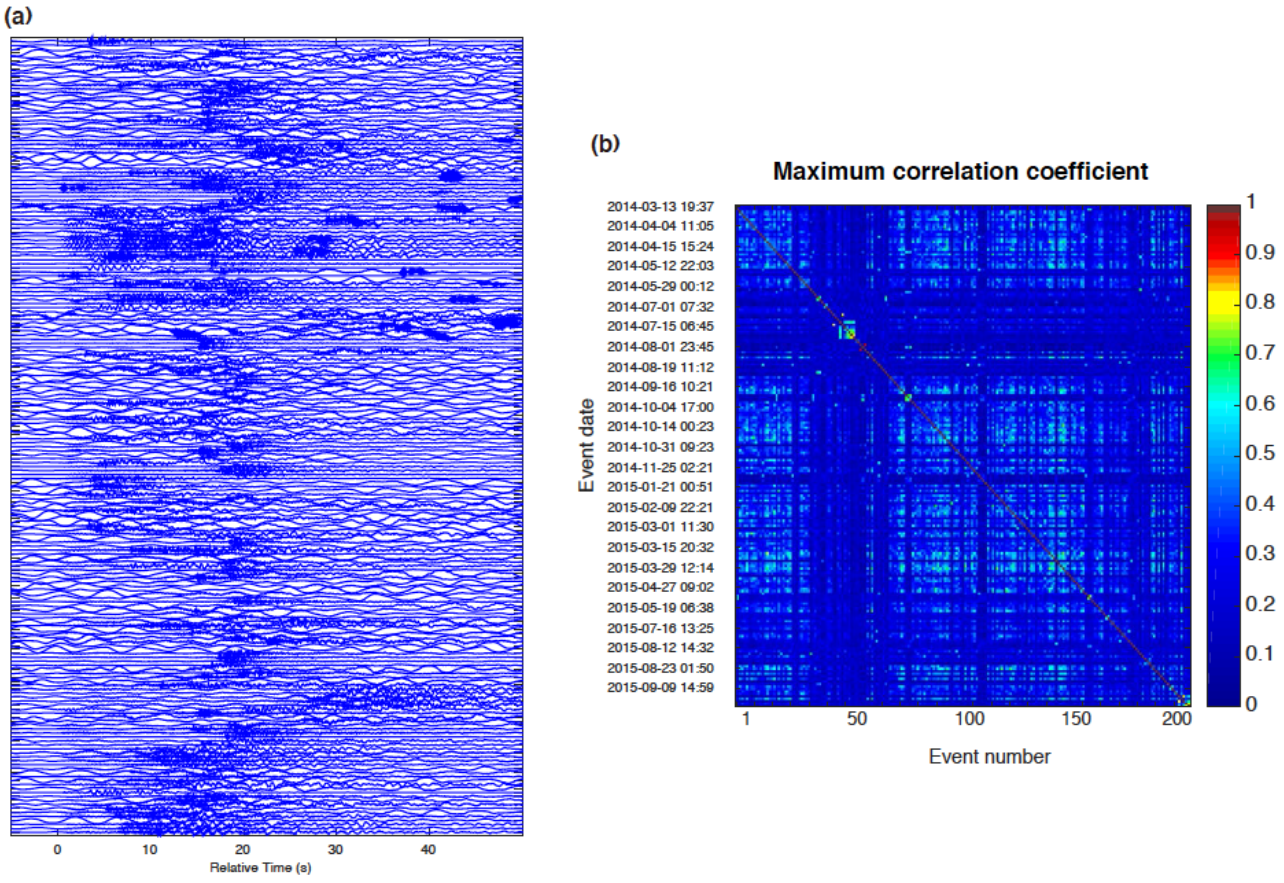

Fig.3.3 (a) Waveforms of the 200 cataloged earthquakes used in the cross-correlation (CC) calculation filtered from 5-15 Hz on the vertical component of station NBC4 in BCAB (Fig.3.1). (b) CC matrix of the waveforms with color bar indicating the CC value; vertical axis indicates the origin time of 25 earthquakes (only 25 are shown due to space limitation).

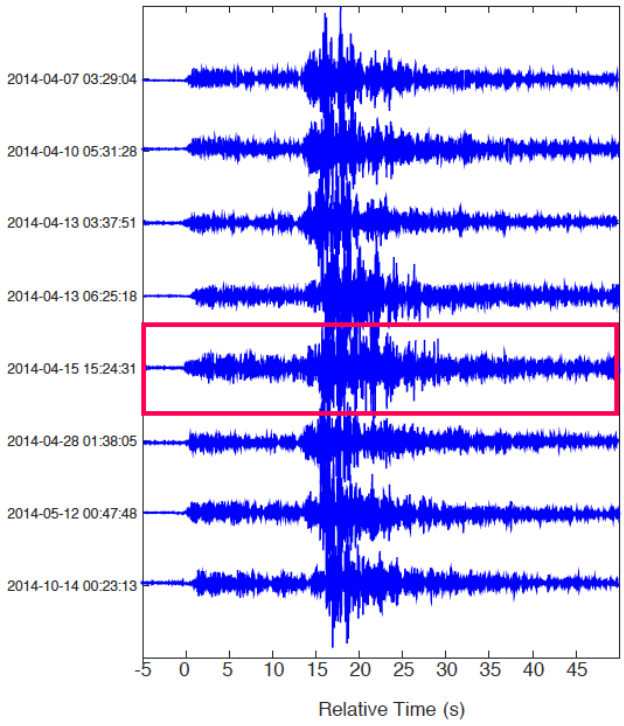

Fig.3.4 Example of an earthquake family in BCAB. All cataloged earthquakes in this family have CC value > 0.5. Waveforms are shown on the East-West component, filtered between 5-15 Hz, as in Fig.3.3. The event highlighted by the red rectangle has the highest SNR, thus is the master event of the family used as a template in the MMF detection.

Once templates are identified, we perform the detection by cross-correlating each of the templates with continuous waveform data at all available stations on horizontal components, and then calculate the normalized cross-correlation value at a given station. We shift the correlation time window in increments of 0.01 s for stations in BCAB and NWT, and increments of 0.025 s for stations in NB (increment differences are due to the sampling rate variation among the data). The normalized cross-correlation value from each E-W component at each station is then summed after being shifted according to the move-out for each template and divided by the number of stations. We allow time window shifts of up to 2 s between

stations to maximize the correlation coefficient values before summing in order to detect earthquakes with hypocenters that vary slightly from template locations. Detection occurs when the maximum correlation sum exceeds an empirically determined threshold. We use the median absolute deviation (MAD), which is the 75th percentile for a symmetric distribution with zero mean (e.g., Skoumal et al., 2014), to define the detection threshold. We find through trial-and-error and visual inspection that a threshold of 19.1*MAD provides a false detection rate < 5% for BCAB and NWT as shown in Fig.3.5. A threshold of 18*MAD provides the same false detection rate for NB. Note that in Fig.3.6, predominantly three stations in BCAB exhibited a high signal-to-noise ratio (stations NBC4, NBC5, and NBC6), and are therefore responsible for the bulk of the additional detections.

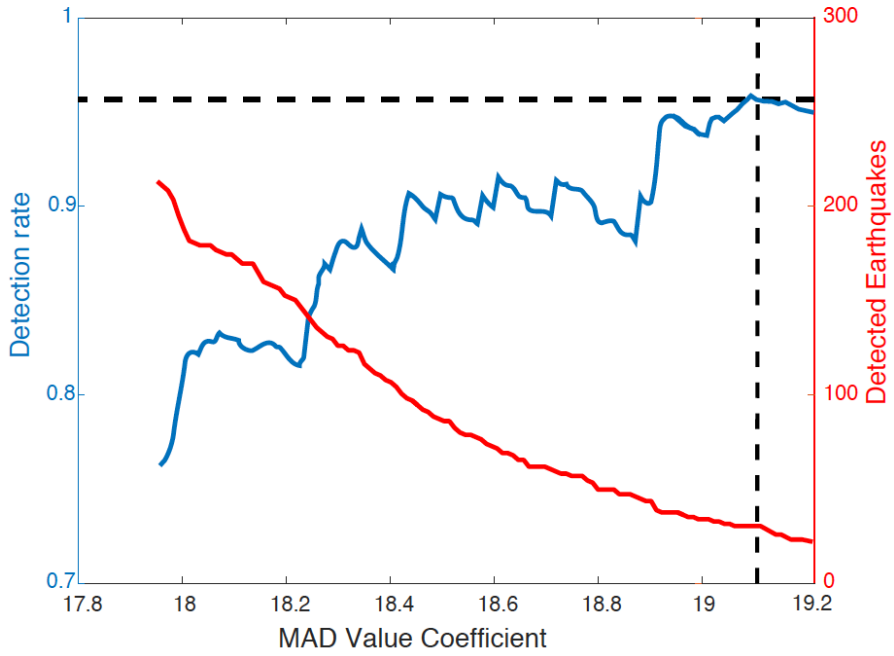

Fig.3.5 Detection accuracy of the MMF algorithm as a function of Mean Absolute Deviation (MAD) value. Red line shows the total number of detected earthquakes using the MMF algorithm. Blue line indicates the detection accuracy determined by manual inspection for a test data set. The total number of detections decreases with MAD, while the detection accuracy increases. The vertical dashed line shows the false detection rate of 5% with a

corresponding 19.1*MAD value.

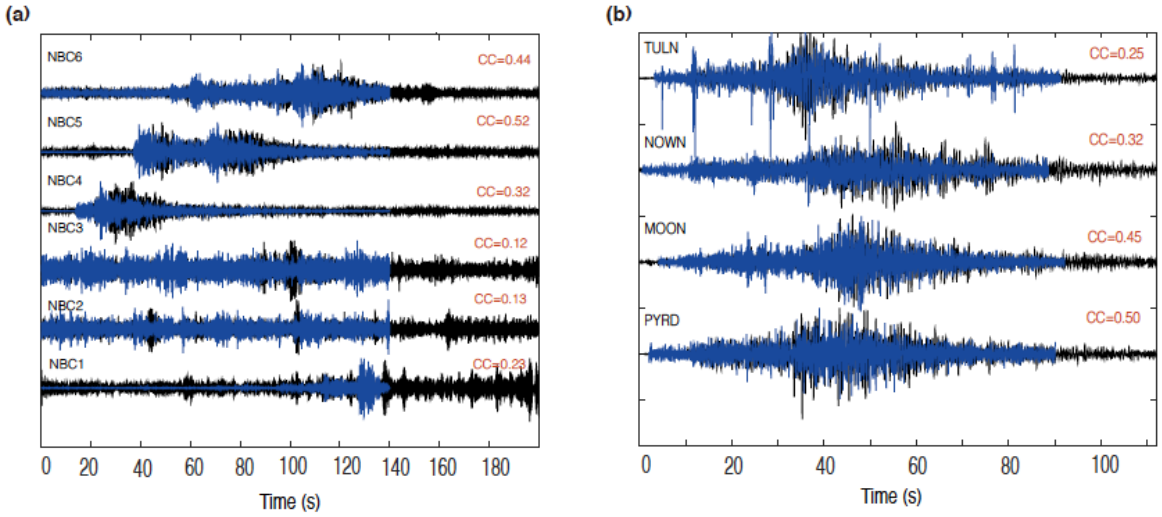

Fig.3.6 (a)(b) Representative examples of two earthquake detections in BCAB (left column) and NWT (right column) using the multi-station matched filter (MMF) approach. (a) Earthquake detection shown on the horizontal components (East-West) in the 5-15 Hz frequency band in BCAB. Continuous waveforms shown in black, template waveforms in blue. Correlation coefficient values (CC) for each trace shown on top of each waveform in red. Mean CC and 19.1*MAD detection threshold values for (a) are 0.29 and 0.19, respectively. Note the detection in (a) results primarily from the top three stations (see text). (b) Detection example in NWT similar to (a), but in the 1-15 Hz frequency band. Mean CC and 19.1*MAD values for (b) are 0.38 and 0.22, respectively. All waveforms are normalized in amplitude.

Once the MMF detections are completed, we compile the original and new detections into an enhanced catalog (for which only the original cataloged events have robustly constrained hypocenters), with which we estimate earthquake rates, and rate changes. We note that the "enhanced catalog" is not a true catalog, as we do not calculate the magnitudes of the MMF-detected events. As stated above, we assume that additional detections that are too small to locate are proximal to templates, however, we lack of any direct constraint on

their locations. Correspondingly, we note that temporal changes of catalog completeness can not be tracked easily if families of earthquakes become active/inactive that do not have a corresponding template for detection. We group the earthquakes for each region into 24-hour bins, and examine the earthquake rates up to 10 days surrounding the mainshock to assess whether changes in earthquake rates resulted from the mainshock surface waves.

From the visual inspection of the histograms, the MMF enhanced catalog data shown in Fig.3.7 suggest that all regions experienced triggering following at least two of the mainshocks. For example, Fig.3.7a qualitatively suggests that mainshocks on 2014/03/10 and 2014/04/01 as well as the 2015/05/30 mainshock may have elicited a sustained increase in seismicity over the entire 10-day time window in BCAB. Seismicity rate also increases in NWT following earthquakes on 2014/04/18, 2014/04/24 and the earthquake on 2014/06/23(Fig.3.7b), and in NB following all three mainshocks (Fig.3.7c). In both NWT and NB, seismicity increases appear to have subsided within 1-2 days following events with direct triggering (blue stars in Fig.3.7).

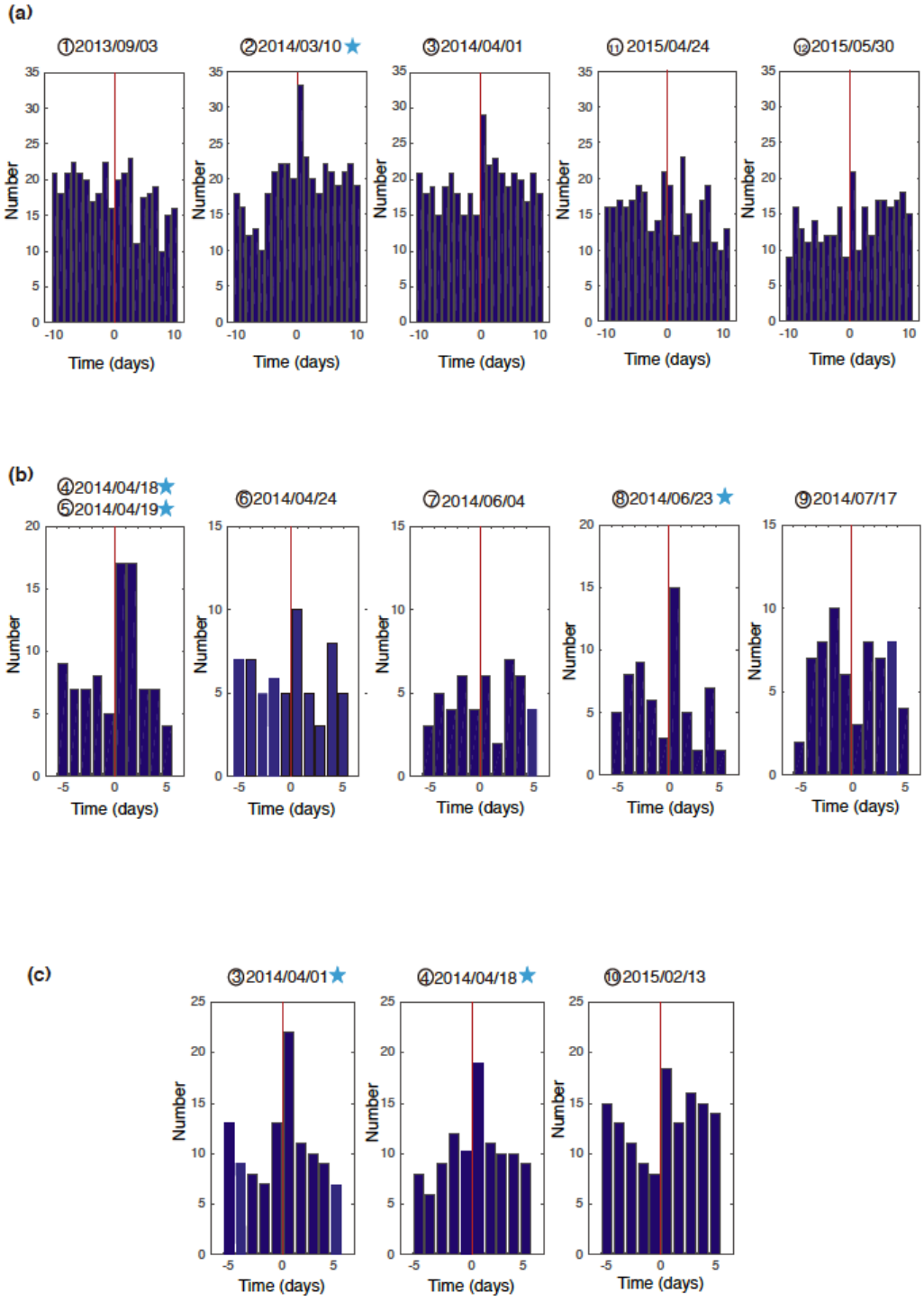

Fig.3.7 Seismicity rates based on the enhanced MMF catalog (see text) grouped into 24-hour bins surrounding candidate mainshocks in each of the three regions within selected time windows of 10 days (BCAB at top) and 5 days (NWT in the middle and NB at bottom) (see text for details of time window selection). Figure (a) shows the seismicity in the 10-day window before and after each mainshock at BCAB, with red lines indicating mainshock onset

time. (b) and (c) show the corresponding seismicity in 5-day time windows for the candidate mainshocks in at NWT and NB, respectively. Blue stars indicate mainshocks with observed direct triggering.

3.3.2 Statistical assessment of dynamic triggering

After qualitatively examining seismicity rate changes (Fig.3.7), we employ two statistical approaches to assess whether the perceived changes in seismicity rates associated with a number of the candidate mainshocks are indeed significant. The first uses Poisson statistics to evaluate the probability of observing a given configuration of average earthquake rates (λ_b and λ_a) before and after a stressing event based on the number of earthquakes that are observed prior to the stressing event (e.g., Kane et al., 2007; van der Elst et al., 2013). The second test provides a consistency check on the results obtained from the first test. It also evaluates the probability of observing changes in average seismicity rates λ_b and λ_a based on inter-event times (van der Elst and Brodsky, 2010). Both tests follow assumptions commonly used in aftershock and dynamic triggering statistical tests, namely that the distribution of background seismicity obeys a Poisson distribution, while potentially triggered sequences following a stressing event decay in time according to the Omori's Law, which can be considered as a non-homogeneous (time-dependent) Poisson process (e.g., Gardner and Knopoff, 1974; Reasenberg and Jones, 1989; Ogata, 1999; van der Elst and Brodsky, 2010). Both tests yield similar results with respect to their assessment of seismicity rate changes, as will be shown in the following.

Before calculating the significance of seismicity rate changes associated with each of the mainshocks as introduced above, we first test our assumption that the local background

seismicity follows a Poisson distribution, one commonly used in dynamic triggering statistical tests (e.g., Velasco et al., 2008; van der Elst and Brodsky, 2010). (Note that we also tested in the affirmative that the results presented below are also consistent if a Binomial distribution is assumed for the background seismicity). Typically earthquake catalogs are de-clustered to recover the background seismicity rate (e.g., Gardner and Knopoff, 1974). However, given that robust locations are not possible for the MMF-detected events in the enhanced catalog, we are unable to perform any type of de-clustering, and thus test the assumption on the original enhanced catalog. Nevertheless, similar to van der Elst and Brodsky (2010), we are assessing triggering based on changes in the average rates before and after a potential trigger (stressing event), thus the details of the underlying distribution are secondary to changes in average rates. We apply both a Chi-squared (χ^2) goodness-of-fit test and one-sample Kolmogorov-Smirnov test on the enhanced catalog earthquake rates before the mainshock and find both algorithms suggest that our assumption of a Poisson distribution cannot be rejected at the 95% confidence level.

3.3.2.1 *p*-value test

If we assume that the seismicity on a basin-wide scale follows a Poisson distribution, we can use the cumulative probability distribution function to estimate the probability that a given number of earthquakes X or more is exceeded in a day. If the probability of X or more earthquakes occurring in one day is small, for example, 0.05, then there is a 95% chance that the observed number during any given day is anomalous, based on the mean rate for the given distribution of events. For each of the mainshocks considered, we use the distribution of

events in the enhanced catalog ranging from 5 to 10 days surrounding each mainshock to determine if anomalous rate changes follow each mainshock, indicating significant seismicity rate changes. Varying the time window length is necessary to test the robustness of the results, as well as to maintain comparable time windows for each region based on data availability. For example, in the case where two of the mainshocks occurred within a short time period (e.g., on 04/18/2014 and 04/19/2014, but with a hypocentral distance larger than 10000 km), we use the same pre-mainshock and post-mainshock time windows for both mainshocks (5 days before 04/18/2014 and 5 days after 04/19/2014). However, for the case where two mainshocks occurred 5 days apart, we use the background seismicity before the first earthquake for both mainshocks. Similarly, we use the 5-day windows following each mainshock to measure post-mainshock seismicity levels due to data availability (e.g., no data exists for the 2014/04/01 mainshock at station SVNB during the time period from 2014/03/22 to 2014/03/25 at NB, nor following the 2014/04/18 mainshock at station MOON in the time period from 2014/04/29 to 2014/05/01 at NWT). Taking the above factors and continuous waveform availability into consideration, we test with maximum time windows of 10 days for BCAB, and 5 days for NWT and NB.

We then proceed with the *p*-value approach to estimate the likelihood of exceeding the number of earthquakes observed in a given period. We start with a given time window between 1 and 10 days, and require time window (t) to be the same both before and after the mainshock, i.e., $t_a = t_b$. The average number of earthquakes (λ) is then empirically defined by dividing the total number of events (n) in each time window, that is $\lambda_b = n_b/t_b$ before the mainshock and $\lambda_a = n_a/t_a$ after the mainshock. If λ_b represents the background rate (based

on a selected time window length), then the λ_a represents the stepwise change in rate following the stressing event. For a homogeneous Poisson process, the probability of observing *n* earthquakes in a time window *t* given an average rate of λ is.

$$P(N_{eq} = n|\lambda t) = \frac{(\lambda t)^n e^{-\lambda t}}{n!} \quad (3.4)$$

Based on the background rate of earthquakes before the stressing event, λ_b, or, given that $t_a = t_b$, the number of earthquakes that occurs before the stressing event, n_b, we can then use the Poisson cumulative distribution function to estimate the probability of a given change in rates (or number of events increasing or decreasing in the "after" time window). In other words, the probability of observing n_a earthquakes or more following a stressing event is given by the compliment of the Poisson CDF:

$$p = 1 - P_{cdf}(n_a|\lambda_b t_b) = 1 - e^{-\lambda_b t_b} \sum_{i=0}^{n_a} \frac{(\lambda_b t_b)^i}{i!} \quad (3.5)$$

We formulate a null hypothesis of no triggering at values of $P_{cdf} < 0.95$ (p-values ≥ 0.05), similar to other studies (e.g., Kane et al. 2007; van der Elst et al., 2013). If the P_{cdf}-value calculated by Eq.3.5 is less than 0.95, then we assume the null hypothesis of no triggering can not be rejected (for the time window length corresponding to the particular P_{cdf}-value). Fig.3.8 shows the maximum P_{cdf}-value for each mainshock as a function of PGV. We repeat the P_{cdf}-value calculation with Eqs. 4-5 for each time window length ranging from 1 to 10 days for each mainshock in order to test the dependence on time window length. Fig.3.9 shows the P_{cdf} (or 1-p) values, with the blue dashed lines indicating the threshold above which the null hypothesis is rejected. In conclusion, high P_{cdf} values (lower p-values) indicate a higher probability of seismicity rate changes resulting from the mainshock, i.e., that

we can reject the null hypothesis of no triggering. (Note that a statistically significant decrease in seismicity would also be classified by a small *p*-value or a large P_{cdf} value, but in our case, most of the changes in seismicity rate following respective candidate mainshocks were positive).

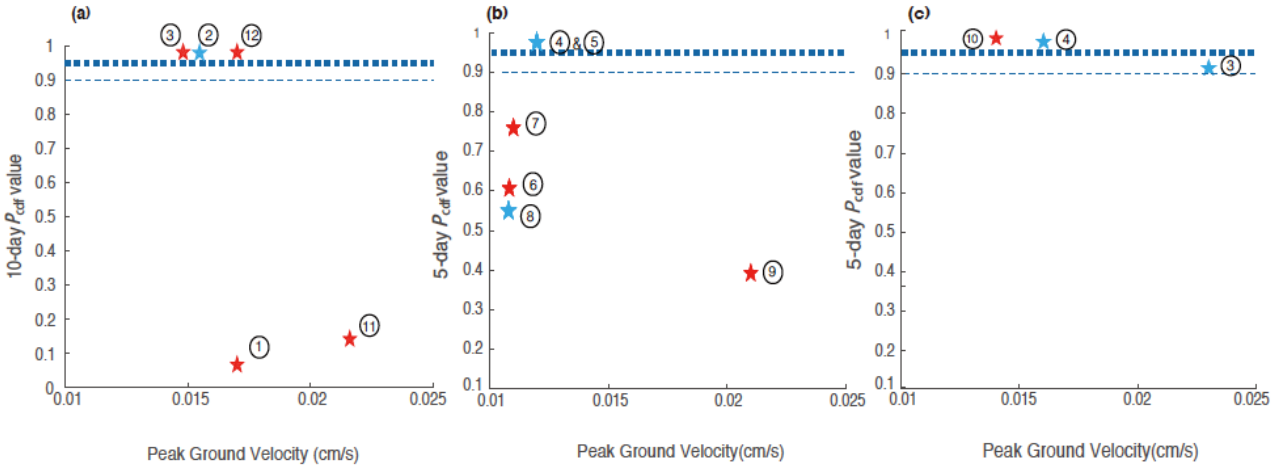

Fig.3.8 Dependence of statistical P_{cdf} value (see Eq.3.6) and observed particle wave velocity for BCAB (left column), NWT (middle column), and NB (right column). There appears to be no clear correlation between dynamic triggering occurrence and observed particle velocity for any of the study areas. Blue dashed lines show triggering thresholds of P_{cdf} = 0.95 (heavy dashed line, α = 0.05 (see text)) and P_{cdf} = 0.9 (thin dashed line, α = 0.1). Red stars correspond to triggering mainshocks with mainshock numbers listed in Tab.3.1, and blue stars correspond to mainshocks with directly triggered earthquakes in Tab.3.2.

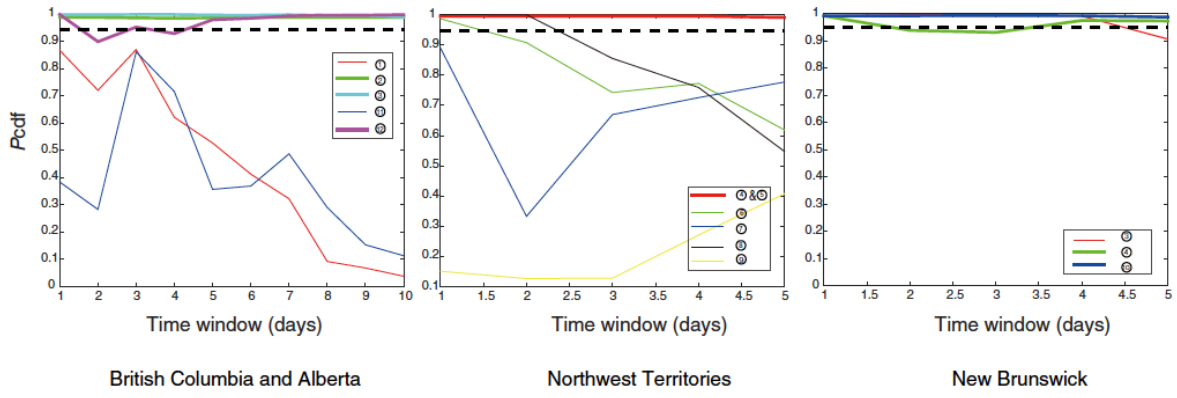

Fig.3.9 P_{cdf} -value (Eq.3.8) as a function of the time window used to calculate changes in seismicity rates. P_{cdf} and p-value are calculated using Eq.8. The number for each mainshock corresponds to the earthquake listed in Tab.3.1.

3.3.2.2 Inter-event time test

We also follow the method of van der Elst and Brodsky (2010) to assess changes in earthquake rates, and approximate the potential non-homogeneous Poissonian seismicity distribution (following stressing events) as stepwise homogeneous process under the assumption tested above. We use time windows of equal length before and after the stressing event (i.e., passage of mainshock surface waves), similar to the p-value test section (i.e. $t_a = t_b$), and calculate the average seismicity rates before and after the stressing event (passing mainshock surface waves) (λ_b, and λ_a, respectively) using the number of earthquakes observed in t_a and t_b. As in the previous test, the time windows before and after the stressing event are of equal length, and in cases where no rate changes are observed, λ_b and $\lambda_{\square}$ should be equal. van der Elst and Brodsky (2010) define the inter-event time ratio, R, as the ratio of waiting times before and after a presumed trigger:

$$R \equiv \frac{t_1}{t_1+t_2} \qquad (3.6)$$

A value of $R = 0.5$ implies no rate change (i.e., no triggering), while $R < 0.5$ implies an increase in earthquake rate, and $R > 0.5$ implies a decrease. In their formulation, rate changes can be quantified using the average rates before and after the stressing event:

$$n \equiv \frac{\lambda_a-\lambda_b}{\lambda_b} \qquad (3.7)$$

The expectation of R ($\langle R \rangle$) for a stepwise homogeneous Poisson process is then given by

the following function of the rate change (n) (see van der Elst and Brodsky, 2010, Appendix A),

$$< R >= \frac{1}{n^2}[(n+1)ln(n+1) - n] \qquad (3.8)$$

After relating the fractional rate change, R, to the earthquake rate change, n, one can use the same statistical model to calculate the probability of observing an earthquake within its own recurrence interval (corresponding to an increase in rate, or decrease in inter-event time) using Eq.3.8 (C3) of van der Elst & Brodsky (2010):

$$P_{ri}(N_{EQs} \geq 1) = 1 - \exp\{-(n+1)\} \qquad (3.9)$$

Similar to the P_{cdf} -value in the previous section, we use a probability of $P_{ri} \geq 95\%$ to indicate triggering. Fig.3.10 indicates the probability, P_{ri}, as calculated in Eq.3.9 with rates calculated as a function of time window length, where the black dashed line in Fig.3.10 indicates no rate changes (n = 0). Fig.3.10 indicates the same results as Figures 3.8 and 3.9: that in addition to the direct triggering observed in the waveforms, the statistical test suggests triggering occurred following mainshocks 2, 3, and 12 in BCAB, mainshocks 4 and 5 in NWT, and 4 and 10 in NB (Tables 3.1, 3.3). The probabilities for both tests in NB would not allow us to strictly rule out the null hypothesis of no triggering on the basis of the enhanced catalog data alone. However, the P_{cdf}-values greater than 90% coupled with the observations of direct triggering suggest triggering did occur following the candidate mainshock 3. Note that due to the close temporal spacing between the two mainshocks in NWT for which triggering is observed, it is impossible to determine whether the observed triggering can be attributed to one or both of them. Fig.3.8 shows the P_{cdf}-value as a function of the observed PGV value of each mainshock, and shows no obvious dependence between P_{cdf} -value and PGV. Tab.3.3

summarizes the results of both the waveform and catalog-based approaches to establishing cases of remote triggering.

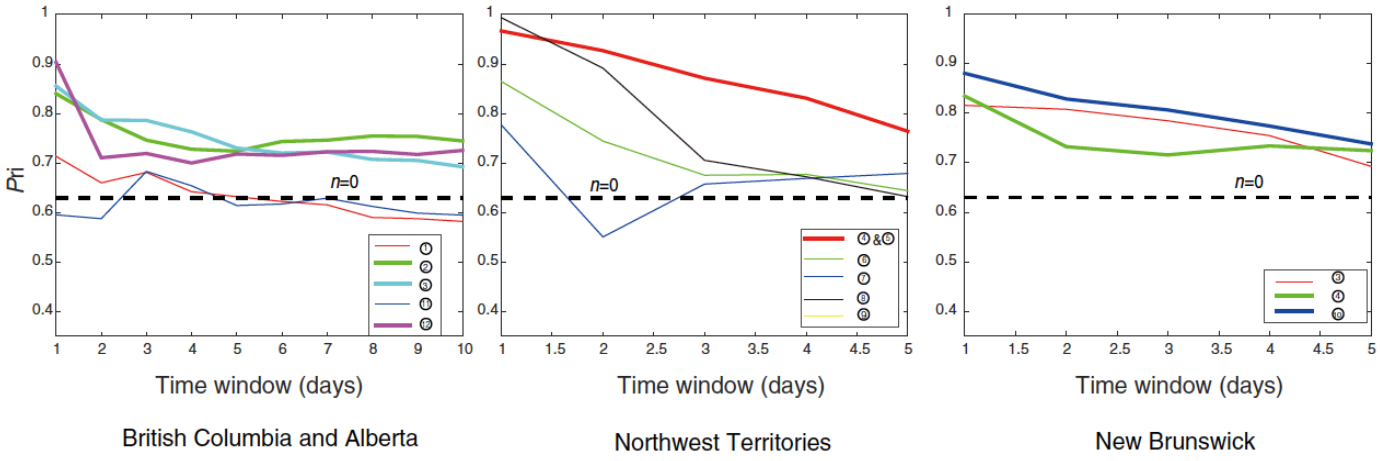

Fig.3.10 P_{ri} -value as a function of time window used to calculate changes in seismicity rates. P_{ri} -values are calculated using Eq.3.9. The number for each mainshock corresponds to earthquake listed in Tab.3.1.

Methods / Basins	Waveform-Based	Catalog-Based
British Columbia and Alberta (BCAB)	2	2, 3, 12
Northwest Territories (NWT)	4, 5, 8	4, 5
New Brunswick (NB)	3, 4	4, 10

Tab.3.3 Mainshocks demonstrating remote triggering via waveform or catalog-based methods for each of the three basins shown in Fig.3.1. The waveform-based column lists mainshocks where triggered earthquakes are visible in the surface wave train of the candidate mainshocks in filtered waveforms (Fig.3.2). The catalog-based column lists where the enhanced catalog suggests significant increases in earthquake rates following the passing of mainshock surface waves considering 5-day (NWT, NB) and 10-day (BCAB) time windows (Fig.3.8). Tab.3.1 lists the corresponding mainshocks and numbers with origin time and magnitude.

3.4 Physical factors influencing triggering

Figures 3.2, 3.7, and 3.8 provide evidence that all three regions do exhibit instances of triggering. From Eq.3.3, we calculate the corresponding stress perturbations for the low-pass filtered waveforms at 0.1 Hz to be smaller than 10 kPa (Fig.3.11 and Tab.3.4), suggesting that the stress perturbations responsible for triggering are on the order of tidal stress magnitudes (e.g., Cochran et al., 2004). However, Fig.3.8 shows a lack of obvious dependence of triggering on PGV. For example, the mainshock with the largest amplitude of shaking does not trigger seismicity at a statistically significant level, suggesting that no simple threshold for the transient stress perturbation exists above which we would expect to observe triggering. In addition, neither the duration of the mainshock nor the cumulative seismic energy seems to be the factor controlling dynamic triggering (Fig.3.12). The absence of any simple correlation suggests that other physical factors may also influence the triggering mechanism(s).

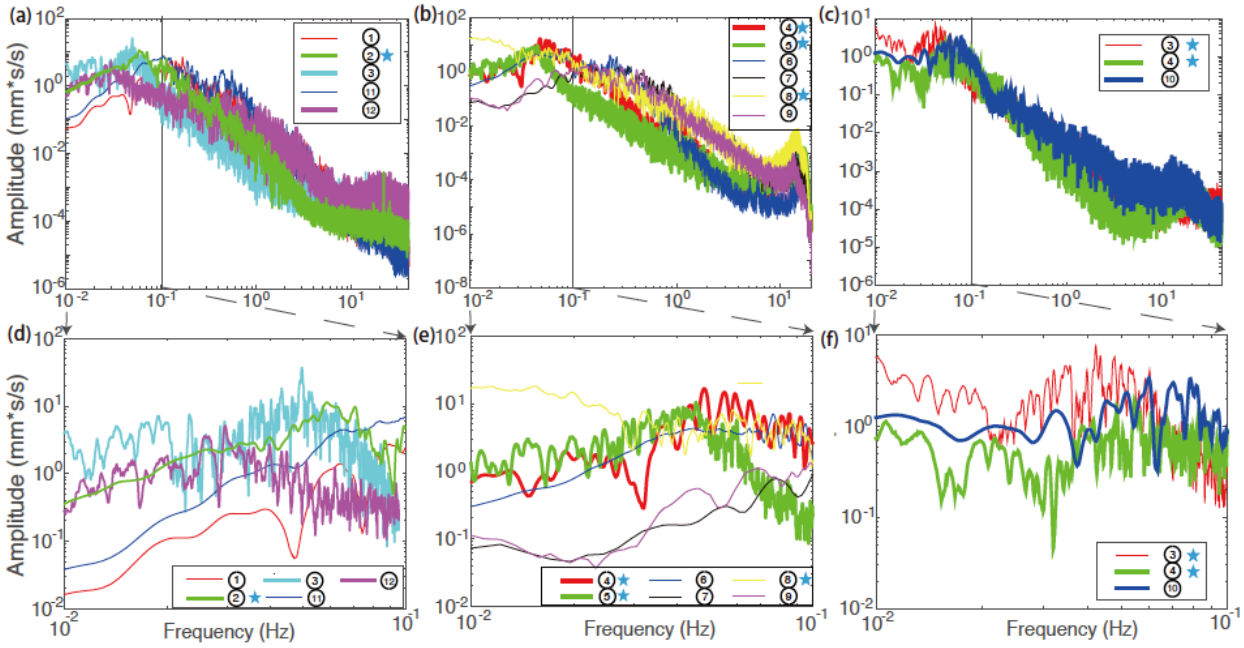

Fig.3.11 Vertical ground velocity spectra for candidate triggering mainshocks listed in Tab.3.1 for BCAB (left column), NWT (middle column), and NB (right column). Thick lines indicate earthquakes associated with remote triggering based on the enhanced catalog. (a)(b)(c) Smoothed mainshock spectra at frequencies 0.01 - 50 Hz. (d)(e)(f) Smoothed mainshock spectra at frequencies of 0.01 - 0.1 Hz (100 – 10 s). Mainshock numbers correspond to Fig.3.8(a)(b)(c). Blue stars in the legend indicate mainshocks with observed direct triggering.

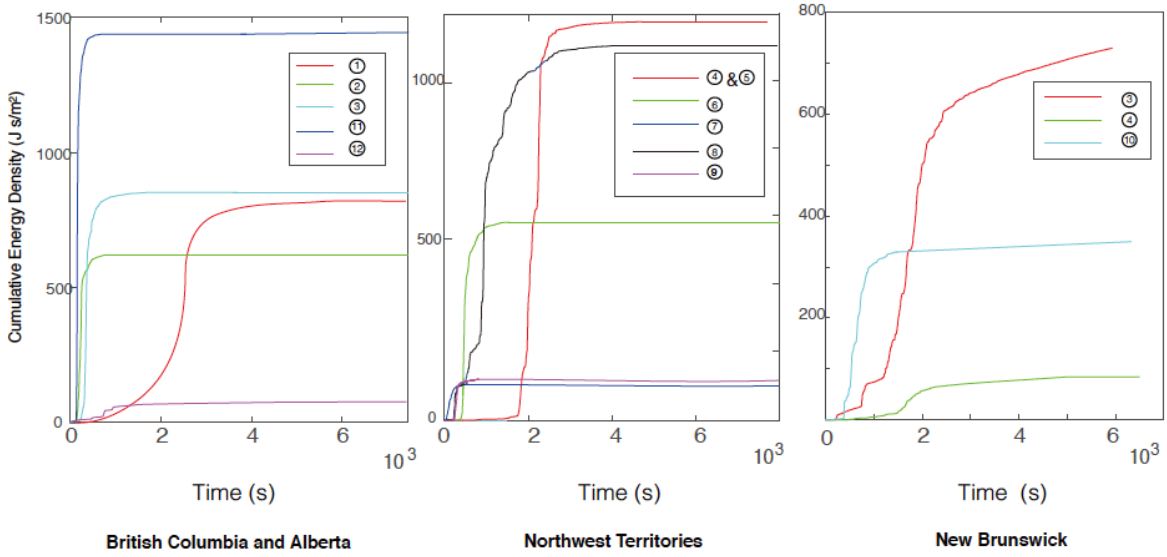

Fig.3.12 Comparison of cumulative energy of triggering mainshocks, where time $t = 0$ corresponds to the P-wave arrival measured at a representative station at each site. Energy is

calculated from the equation of Brodsky and Prejean, 2005, namely, $E = \rho c \int \mu^2 dt$, where ρ is the local rock density, c is the phase velocity and μ is the particle velocity. The results in the figure provide a quantitative measure of duration and cumulative shaking.

British Columbia and Alberta		Northwest Territories		New Brunswick	
1	1.1 kPa	4 & 5	2.8 kPa	3	1.6 kPa
2	3.4 kPa	6	3.0 kPa	4	0.4 kPa
3	1.9 kPa	7	0.5 kPa	10	1.0 kPa
11	2.2 kPa	8	4.5 kPa		
12	1.2 kPa	9	0.7 kPa		

Tab.3.4 Maximum estimated transient stress inferred (based on Equation 3.3) from surface wave amplitudes at periods > 10 s.

The factors that may influence the occurrence of triggering include the amplitude of low frequency shaking, magnitude of transient stress imparted by surface waves, and the tectonic regime. We therefore consider each of the factors in the following as well as their implications for triggering mechanism(s).

Although Fig.3.8 demonstrates a lack of dependence of $P_{c\text{-}sum}$ value on PGV, examining the dependence of triggering on frequency suggests that a correlation exists. Fig.3.11 shows the mainshock ground displacement spectra over a range of frequencies, with spectral amplitudes of mainshocks plotted in bold if they are associated with triggering. In particularly for BCAB, the waveforms suggest the dependence of $P_{c\text{-}sum}$ value on the frequency of the mainshock shaking, as reported by other studies (e.g., Brodsky and Prejean, 2005, Aiken and Peng, 2014, Wang et al., 2015). Specifically, the long-period shaking (i.e., below 0.1 Hz) may be more effective at promoting dynamic triggering, compared with shaking at periods above

0.1 Hz. For instance, Fig.3.11(a) shows that the two mainshocks (1) and (11) with smaller low-frequency shaking amplitudes did not trigger changes in earthquake rates, while the remaining events with higher amplitudes at longer periods (particularly below 30-40 s) did. The two mainshocks (3) and (4) in NWT (Fig.3.11(b)) occur within a 5-day time window, therefore from Figures 3.8(b) and 3.11(b) it is difficult to attribute triggering to one of the mainshocks individually. It is unclear as to why the other mainshocks with similar low-frequency amplitudes (i.e., Events 6 and 8 in Fig.3.8(b) and Fig.3.11(b)) do not have associated triggering within the 5-day time window. Potential explanations could be that the receiver faults were not optimally oriented in the transient stress field to promote triggering (Hill, 2008) and the 5-day time window could be too long. However, since we do not have local (receiver) fault information, it is impossible to do more than speculate on the importance of fault orientation in NWT. For NB, with similar low frequency shaking, two mainshocks show dynamic triggering while one does not if $P_{c\text{-}sum}$ is set at 0.95, at least within the 5-day time window. If we also consider a shorter time window or a slightly lower probability of rejecting the null hypothesis (i.e., $P_{c\text{-}sum}$ = 0.8), then all three mainshocks in NB caused statistically significant triggering. Because all three mainshocks may have triggered seismicity in NB, it is difficult to assess the relative influence on earthquake triggering between long-period and short-period shaking. In summary, our observations in BCAB seem to be consistent with other studies that long-period shaking is more effective at triggering local earthquakes.

In our study, the magnitude of dynamic stress perturbation calculated from observed particle velocities responsible for directly triggered earthquakes (Fig.3.2) ranges from 0.2-1.7

kPa (Tab.3.2, available in the electronic supplement to this article). The small stresses imposed by the triggering mainshocks imply that local faults are likely in a critically stressed state such that even small stress perturbations can promote earthquake nucleation. The delicate equilibrium from which many of the local faults may be easily disturbed may be related to the presence of injection fluids from unconventional hydrocarbon development, and the low permeability of the tight shale formations which could function to keep pore fluid pressures high (Neuzil, 1994; Flewelling and Sharma, 2014). For example, the increase in seismicity after the beginning of hydraulic fracturing in Horn River basin of British Columbia and the strong temporal correlation of seismic events with monthly operations at a nearby disposal well at Cordel Field in western Alberta suggest that pore pressure remained high enough to trigger seismicity for months after injection ceased (e.g., Schultz et al., 2014; Farahbod et al., 2015; Atkinson et al., 2016). Furthermore, fluid diffusion timescale in tight shale formations is expected to be much longer than in more crystalline rocks near sites such as Soultz Sous-Forets, France or Basel, Swizterland (Shapiro et al., 2002; Shapiro and Dinske, 2009), suggesting that pore pressure could remain elevated for a longer time. As Tab.3.1 indicates (available in the electronic supplement to this article), most time intervals between successive triggering mainshocks are on the order of months, implying that many pre-existing faults in the region may remain critically stressed and susceptible to triggering over comparable time scales due to the widespread injection activity. The presence of fluids along pre-existing faults or cracks may also serve to amplify stress perturbations locally and therefore facilitate seismic rupture (Zheng, 2018).

Finally, tectonic regime has been proposed as a key physical factor that influences

dynamic triggering. Although dynamic triggering has been documented in all kinds of tectonic environments (Velasco et al., 2008; Wu et al., 2011; Parsons et al., 2014; Wei et al., 2015), it appears that trans-tensional and extensional environments may be more susceptible to dynamic triggering than compressional ones, as the faults in extensional tectonic regimes may be weaker (Harrington and Brodsky, 2006; Hill and Prejean, 2007; Hill, 2015). However, previous studies using shallow stress measurements and focal mechanism analysis for a small number of earthquakes in the northern part of the Appalachian Seismic Zone in NB suggest reverse and strike-slip faulting mechanisms, implying that the triggering we observe here occurs in a dominantly compressional regional stress field (Bent et al., 2003; Heidbach et al., 2008; Lamontagne et al., 2015). The basins at BCAB and NWT are located in an intra-plate tectonic environment not historically associated with high levels of background seismicity, as is NB. Regional stress field (Fig.3.1a) and focal mechanism solutions of M 4+ earthquakes in BCAB (Fig.3.13) also suggest a tectonically compressive regime (Ristau et al., 2002; Heidbach et al., 2008; Kao et al., 2012). Therefore the occurrence of triggering exhibited in all three regions suggests that a trans-tensional or extensional tectonic regime is not a prerequisite for dynamic triggering, at least in injection environments.

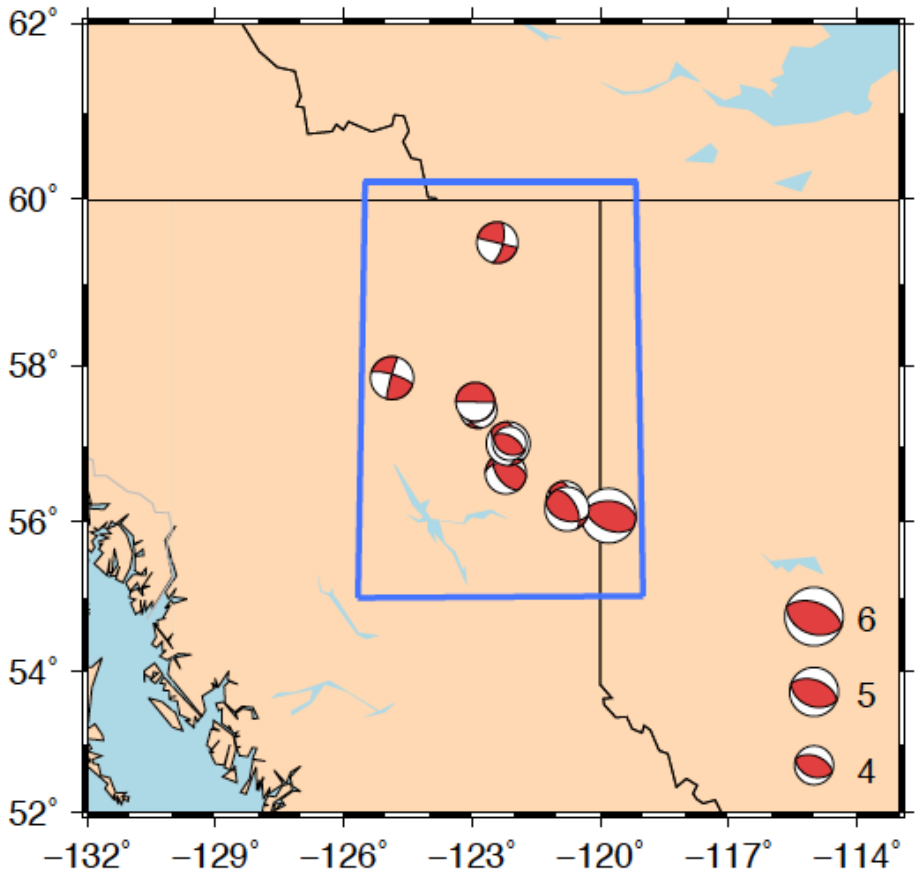

Fig.3.13 Focal mechanism solutions of M > 4 events occurring from 2001-2015 in the BCAB region (inside the blue box, from Kao et al., 2012). Beachball diameter corresponds to event magnitude. All focal mechanism solutions shown can be requested through NRCan website.

3.5 Discussion

We find that each of the regions experiences changes in seismicity level of varying significance depending on the length of window considered (Fig.3.9). For instance, the $P_{c\text{-}sum}$ value increases in BCAB as the time window increases from 1 to 10 days for several mainshocks, suggesting that delayed triggering occurs. In contrast, most of the $P_{c\text{-}sum}$ value decreases for NWT and NB, over the time window, suggesting a more immediate response. While delayed triggering in BCAB may be an indication of lower permeability and longer

diffusion times, the $P_{c\text{-}sum}$ value dependence on time window length may have additional implications. BCAB has a longer unconventional hydrocarbon development history (Schultz et al., 2014; Lamontagne et al., 2015), meaning injection has been occurring over a longer time period, and could result in a relatively larger permeability enhancement relative to the other regions. Several studies have shown the importance of poroelastic triggering, and the results of such studies may be useful for providing a unifying mechanism to explain delayed vs. immediate triggering. For example, new modeling results suggest that, without highly permeable conduits effectively connecting the injected fluids to the sites of triggering, earthquakes within a few kilometers of a hydraulic fracturing well near Crooked Lake, Alberta, are more likely induced by the elastic response (shear and normal stress changes) of the rock matrix than by pore pressure perturbation (Deng et al., 2016). Similarly, Goebel et al. (2017) demonstrate that the poroelastic response of the medium is required to explain observed earthquake triggering at distances of up to 40 km from disposal wells. Particularly in the case of BCAB, it would be difficult for pore pressures to migrate on the time scales needed to explain triggering of events by fluid pressure migration alone in such low permeability rock units (Deng et al., 2016). Conversely, pore pressure migration might be responsible for triggering over the time scales of several days, explaining why some observed triggering is delayed relative to the surface wave arrivals.

If BCAB has experienced a larger permeability enhancement compared to the other regions, the pore pressure perturbations resulting from the transient seismic wave mediated stresses may allow for triggering over an extended period after the mainshock, whereas the stresses transmitted via the rock matrix might more readily explain the immediate triggering

response. Similarly, immediate triggering at the NWT and NB regions would be consistent with a mechanism of stresses transfer via the rock matrix. The broader scale implications of the poroelastic modeling studies (e.g., Deng et al., 2016; Goebel et al., 2017) as well as the results shown here, could be that immediate or delayed triggering may be explained by the relative importance of the two mechanisms, namely rock matrix response and pore pressure diffusion, due to their different influential time scales.

One line of evidence that also supports pore pressure diffusion having at least some role in triggering is the apparent dependence of triggering on low frequency shaking. Fig.3.9 and 3.11 examine the variation of $P_{c\text{-}sum}$ value with respect to the length of time window, and the results show that the mainshock with stronger low frequency shaking is associated with triggering. We note that the observations in Fig.3.11(as well as other studies) support the claim that low-frequency shaking may be more effective at triggering, and that dilatational strain generated from seismic waves could alter pore pressure, flow velocities, and permeability at a given frequency (Elkhoury et al., 2006; Elkhoury et al., 2011; Candela et al., 2014; Candela et al., 2015). The flow-driven mechanism of unclogging of fine fractures is the most reliable explanation of transient permeability enhancement during the passage of seismic waves, as suggested by Candela et al. (2015). Fracture unclogging is also consistent with a new study suggesting that low-frequency waves are more effective at triggering fault rupture because they can amplify stresses in fluid filled fractures by more than two orders of magnitude (Zheng, 2018). In addition, low-frequency shaking has a longer cycling period that allows fractures to remain open compared to the quick opening and closure during high frequency shaking, which may potentially allow the stress amplification suggested by Zheng

(2018) to act over sustained periods. Slower opening and closing may also be more efficient for increasing the fluid velocities and allowing fluid, and entrained particles dislodged from fractures, to pass. Recent studies on the focal mechanisms of induced earthquakes in the WCSB suggest significant non-double-couple components, which may also be explained by dilatant jogs created between multiple fractures (Zhang et al., 2016).

3.6 Conclusions

In this chapter, we find evidence for remote dynamic triggering in three unconventional hydrocarbon regions in Canada using observations of direct triggering in continuous waveform data, and an enhanced earthquake catalog built from a multiple-station matched-filter detection method. We perform a *p*-value statistical test on the catalog to quantitatively support both the observations of direct triggering and the perceived increases in seismicity observed in the enhanced catalog. The propensity for triggering occurs in areas within a compressive tectonic regime, suggesting triggering does not require extensional or transtensional tectonic environments. The transient stresses estimated from observed particle velocities smaller than 10 kPa due to passing surface waves are inferred to have caused changes in seismicity levels at all three regions, suggesting that low permeability in shale formations keeps pore pressure high near injection sites over extended periods of time. The observations of triggering presented here, coupled with the injection history and recent poroelastic modeling results, suggest that immediate versus delayed seismicity increases from transient stresses may result from stress transfer via the rock matrix and pore pressure perturbations, respectively, and could provide a unifying mechanism that explains both types of triggering.

3.7 References for Chapter 3

Aiken, C., & Peng, Z. G. (2014). Dynamic triggering of microearthquakes in three geothermal/volcanic regions of California. *Journal of Geophysical Research-Solid Earth, 119*(9), 6992-7009. doi: 10.1002/2014jb011218

Aki, K., & Richards, P. G. (2002). *Quantitative seismology.*

Aron, A., & Hardebeck, J. L. (2009). Seismicity rate changes along the central California coast due to stress changes from the 2003 M 6.5 San Simeon and 2004 M 6.0 Parkfield earthquakes. *Bulletin of the Seismological Society of America, 99*(4), 2280-2292. doi: 10.1785/0120080239

Atkinson, G. M., Eaton, D. W., Ghofrani, H., Walker, D., Cheadle, B., Schultz, R., Shcherbakov, R., Tiampo, K., Gu, J., Harrington, R. M., Liu, Y. J., van der Baan, M., & Kao, H. (2016). Hydraulic Fracturing and Seismicity in the Western Canada Sedimentary Basin. *Seismological Research Letters, 87*(3), 631-647. doi: 10.1785/0220150263

Bent, A. L., Drysdale, J., & Perry, H. C. (2003). Focal mechanisms for eastern Canadian earthquakes, 1994–2000. *Seismological Research Letters, 74*(4), 452-468. doi: 10.1785/gssrl.74.4.452

Brodsky, E. E., Karakostas, V., & Kanamori, H. (2000). A new observation of dynamically triggered regional seismicity: Earthquakes in Greece following the August, 1999 Izmit, Turkey earthquake. *Geophysical Research Letters, 27*(17), 2741-2744. doi: 10.1029/2000gl011534

Brodsky, E. E., & Prejean, S. G. (2005). New constraints on mechanisms of remotely triggered seismicity at Long Valley Caldera. *Journal of Geophysical Research-Solid Earth, 110*(B4). doi: 10.1029/2004jb003211

Candela, T., Brodsky, E. E., Marone, C., & Elsworth, D. (2014). Laboratory evidence for particle mobilization as a mechanism for permeability enhancement via dynamic stressing. *Earth and Planetary Science Letters, 392*, 279-291. doi: 10.1016/J.Epsl.2014.02.025

Candela, T., Brodsky, E. E., Marone, C., & Elsworth, D. (2015). Flow rate dictates permeability enhancement during fluid pressure oscillations in laboratory experiments. *Journal of Geophysical Research: Solid Earth*. doi: 10.1002/2014JB011511

Cochran, E. S., Vidale, J. E., & Tanaka, S. (2004). Earth tides can trigger shallow thrust fault

earthquakes. *Science, 306*(5699), 1164-1166. doi: 10.1126/science.110396

Barbour, A. J., Norbeck, J. H., & Rubinstein, J. L. (2017). The effects of varying injection rates in Osage County, Oklahoma, on the 2016 M w 5.8 Pawnee earthquake. *Seismological Research Letters, 88*(4), 1040-1053. doi: 10.1785/0220170003

Deng, K., Liu, Y., & Harrington, R. M. (2016). Poroelastic Stress Triggering of the December 2013 Crooked Lake, Alberta, Induced Seismicity Sequence. *Geophysical Research Letters*. doi: 10.1002/2016GL070421

Elkhoury, J. E., Brodsky, E. E., & Agnew, D. C. (2006). Seismic waves increase permeability. *Nature, 441*(7097), 1135-1138.

Elkhoury, J. E., Niemeijer, A., Brodsky, E. E., & Marone, C. (2011). Laboratory observations of permeability enhancement by fluid pressure oscillation of in situ fractured rock. *Journal of Geophysical Research-Solid Earth, 116*(B2). doi: 10.1029/2010jb007759

Farahbod, A. M., Kao, H., Walker, D. M., Cassidy, J. F., & Calvert, A. (2015). Investigation of regional seismicity before and after hydraulic fracturing in the Horn River Basin, northeast British Columbia. *Canadian Journal of Earth Sciences, 52*(2), 112-122. doi: 10.1139/cjes20140162

Flewelling, S. A., & Sharma, M. (2014). Constraints on upward migration of hydraulic fracturing fluid and brine. *Groundwater, 52*(1), 9-19. doi: 10.1111/gwat.12095

Gardner, J., & Knopoff, L. (1974). Is the sequence of earthquakes in Southern California, with aftershocks removed, Poissonian? *Bulletin of the Seismological Society of America, 64*(5), 1363-1367.

Goebel, T., Weingarten, M., Chen, X., Haffener, J., & Brodsky, E. (2017). The 2016 Mw5. 1 Fairview, Oklahoma earthquakes: Evidence for long-range poroelastic triggering at> 40 km from fluid disposal wells. *Earth and Planetary Science Letters, 472*, 50-61. doi: 10.1016/jepsl201705011

Gomberg, J., & Davis, S. (1996). Stress strain changes and triggered seismicity at The Geysers, California. *Journal of Geophysical Research-Solid Earth*, 101(B1), 733-749. doi: 10.1029/95jb03250

Gomberg, J., Reasenberg, P. A., Bodin, P., & Harris, R. A. (2001). Earthquake triggering by seismic waves following the Landers and Hector Mine earthquakes. *Nature, 411*(6836), 462-466. doi: 10.1038/35078053

Gu, Y. J., & Shen, L. (2015). Noise correlation tomography of Southwest Western Canada Sedimentary Basin. *Geophysical Journal International, 202*(1), 142-162. doi:

10.1093/gji/ggv100

Harrington, R. M., & Brodsky, E. E. (2006). The absence of remotely triggered seismicity in Japan. *Bulletin of the Seismological Society of America, 96*(3), 871-878. doi: 10.1785/0120050076

Heidbach, O., Tingay, M., Barth, A., Reinecker, J., Kurfeß, D., & Müller, B. (2008). The world stress map database release 2008, doi: 10.1594/GFZ. *WSM. Rel2008*.

Hill, D. P. (2012). Dynamic stresses, Coulomb failure, and remote triggering-corrected. *Bulletin of the Seismological Society of America*, 102,2311-2336. doi: 10.1785/012120085

Hill, D. P. (2015). On the sensitivity of transtensional versus transpressional tectonic regimes to remote dynamic triggering by Coulomb failure. *Bulletin of the Seismological Society of America, 105*(3), 1339-1348. doi: 10.1785/0120140292

Hill, D. P., & Prejean, S. G. (2007). 4.09 - Dynamic Triggering. In G. Schubert (Ed.), *Treatise on Geophysics* (pp. 257-291). Amsterdam: Elsevier.

Hill, D. P., Reasenberg, P. A., Michael, A., Arabaz, W. J., Beroza, G., Brumbaugh, D., Brune, J. N., Castro, R., Davis, S., Depolo, D., Ellsworth, W. L., Gomberg, J., Harmsen, S., House, L., Jackson, S. M., Johnston, M. J., Jones, L., Keller, R., Malone, S., Munguia, L., Nava, S., Pechmann, J. C., Sanford, A., Simpson, R. W., Smith, R. B., Stark, M., Stickney, M., Vidal, A., Walter, S., Wong, V., & Zollweg, J. (1993). Seismicity remotely triggered by the magnitude 7.3 Landers, California, earthquake. *Science, 260*(5114), 1617-1623. doi: 10.1126/science.260.5114.1617

Hughes, S., & Luetgert, J. H. (1991). Crustal structure of the western New England Appalachians and the Adirondack Mountains. *Journal of Geophysical Research: Solid Earth, 96*(B10), 16471-16494. doi: 10.1029/91JB01657

Kane, D. L., Kilb, D., Berg, A. S., & Martynov, V. G. (2007). Quantifying the remote triggering capabilities of large earthquakes using data from the ANZA Seismic Network catalog (southern California). *Journal of Geophysical Research: Solid Earth,* 112(B11). doi: 10.1029/2006JB004714

Kao, H.,and P.-R. Jian (1999). Source parameters of regional earthquakes in Taiwan: July 1995-December 1996, *Terr. Atmos. Ocean. Sci*., v10, 585-604.

Kao, H., S.-J. Shan, A. Bent, C. Woodgold, G. Rogers, J.F. Cassidy, and J. Ristau (2012). Regional centroid-moment-tensor analysis for earthquakes in Canada and adjacent regions: An update, *Seismol. Res. Lett*., v83, 505-515. doi: 10.1785/gssrl.83.3.505

Keranen, K., Weingarten, M., Abers, G., Bekins, B., & Ge, S. (2014). Sharp increase in central Oklahoma seismicity since 2008 induced by massive wastewater injection. *Science, 345*(6195), 448-451. doi: 10.1126/science.1255802

Lamontagne, M., Lavoie, D., Ma, S., Burke, K. B., & Bastow, I. (2015). Monitoring the earthquake activity in an area with shale gas potential in southeastern New Brunswick, Canada. *Seismological Research Letters, 86*(4), 1068-1077. doi: 10.1785/0220150051

Lay, T., & Wallace, T. C. (1995). *Modern global seismology* (Vol. 58): Academic press.

Love, A. (1927). A treatise on the mathematical theory of elasticity.

Matthews, M. V., & Reasenberg, P. A. (1988). Statistical-Methods for Investigating Quiescence and Other Temporal Seismicity Patterns. *Pure and Applied Geophysics, 126*(2-4), 357-372. doi: 10.1007/Bf00879003

Neuzil, C. (1994). How permeable are clays and shales? *Water resources research, 30*(2), 145-150. doi: 10.1029/93WR02930

Ogata, Y. (1999). Seismicity analysis through point-process modeling: A review Seismicity patterns, their statistical significance and physical meaning (pp. 471-507): Springer doi: 10.1007/978-3-0348-8677-2_14.

Ostle, B, and Richard W. M (1975). Statistics in Research: Basic Concepts and Techniques for Research Workers.

Parsons, T., Segou, M., & Marzocchi, W. (2014). The global aftershock zone. *Tectonophysics, 618*, 1-34. doi: 10.1016/j.tecto.2014.01.038

Peter, C. St. "Maritimes Basin evolution: key geologic and seismic evidence from the Moncton Subbasin of New Brunswick." (1993): 233-270. Atlantic Geology.

Prejean, S., Hill, D., Brodsky, E. E., Hough, S., Johnston, M., Malone, S., Oppenheimer, D., Pitt, A., & Richards-Dinger, K. (2004). Remotely triggered seismicity on the United States west coast following the Mw 7.9 Denali Fault earthquake. *Bulletin of the Seismological Society of America, 94*(6B), S348-S359. doi: 10.1785/0120040610

Reyes, C. G., & West, M. E. (2011). The Waveform Suite: A Robust Platform for Manipulating Waveforms in MATLAB. *Seismological Research Letters, 82*(1), 104-110. doi: 10.1785/Gssrl.82.1.104

Ristau, J., G. Rogers, and J.F. Cassidy (2003). Moment magnitude-local magnitude calibration for earthquakes off Canada's west coast, *Bull. Seismol. Soc. Am*., v93, 2296-2300. doi: 10.1785/0120030035

Schultz, R., Stern, V., & Gu, Y. J. (2014). An investigation of seismicity clustered near the

Cordel Field, west central Alberta, and its relation to a nearby disposal well. *Journal of Geophysical Research: Solid Earth, 119*(4), 3410-3423. doi: 10.1002/2013JB010836

Schultz, R., Stern, V., Novakovic, M., Atkinson, G., & Gu, Y. J. (2015). Hydraulic fracturing and the Crooked Lake Sequences: Insights gleaned from regional seismic networks. *Geophysical Research Letters, 42*(8), 2750-2758. doi: 10.1002/2015gl063455

Shapiro, S., & Dinske, C. (2009). Fluid-induced seismicity: Pressure diffusion and hydraulic fracturing. *Geophysical Prospecting, 57*(2), 301-310. doi: 10.1111/j.1365-2478.2008.00770.x

Shapiro, S. A., Rothert, E., Rath, V., & Rindschwentner, J. (2002). Characterization of fluid transport properties of reservoirs using induced microseismicity. *Geophysics, 67*(1), 212-220. doi: 10.1190/1.1451597

Skoumal, R. J., Brudzinski, M. R., & Currie, B. S. (2015b). Earthquakes induced by hydraulic fracturing in Poland Township, Ohio. *Bulletin of the Seismological Society of America*, 105(1), 189-197. doi: 10.1785/0120140168

Skoumal, R. J., Brudzinski, M. R., Currie, B. S., & Levy, J. (2014). Optimizing multi-station earthquake template matching through re-examination of the Youngstown, Ohio, sequence. *Earth and Planetary Science Letters*, 405, 274-280. doi: 10.1016/J.Epsl.2014.08.033

Stark, M. A., & Davis, S. D. (1996). Remotely triggered microearthquakes at The Geysers geothermal field, California. *Geophysical Research Letters, 23*(9), 945-948. doi: 10.1029/96GL00011

van der Elst, N. J., & Brodsky, E. E. (2010). Connecting near-field and far-field earthquake triggering to dynamic strain. *Journal of Geophysical Research, 115*(B7). doi: 10.1029/2009jb006681

van der Elst, N. J., Savage, H. M., Keranen, K. M., & Abers, G. A. (2013). Enhanced remote earthquake triggering at fluid-injection sites in the midwestern United States. *Science, 341*(6142), 164-167. doi: 10.1126/science.1238948

Velasco, A. A., Hernandez, S., Parsons, T., & Pankow, K. (2008). Global ubiquity of dynamic earthquake triggering. *Nature Geoscience, 1*(6), 375-379. doi: 10.1038/ngeo204

Wang, B., Harrington, R. M., Liu, Y., Yu, H., Carey, A., & Elst, N. J. (2015). Isolated cases of remote dynamic triggering in Canada detected using cataloged earthquakes combined with a matched-filter approach. *Geophysical Research Letters, 42*(13),

5187-5196. doi: 10.1002/2015GL064377

Wei, M., Y. Liu, Y. Kaneko, J. J. McGuire, R. Bilham, Dynamic triggering of creep events in the Salton Trough, Southern California by regional M>=5.4 earthquakes constrained by geodetic observations and numerical simulations, *Earth and Planet. Sci. Lett.*, doi:10.1016/j.epsl.2015.06.044, 2015.

Wen, K.-L., Beresnev, I. A., & Cheng, S.-N. (1996). Moderate-magnitude seismicity remotely triggered in the Taiwan region by large earthquakes around the Philippine Sea plate. *Bulletin of the Seismological Society of America*, 86(3), 843-847.

Wiemer, S. (2000). Introducing probabilistic aftershock hazard mapping. *Geophysical Research Letters*, 27(20), 3405-3408 doi: 10.1029/2000GL011479

Wu, C., Peng, Z., Wang, W., & Chen, Q.-F. (2011). Dynamic triggering of shallow earthquakes near Beijing, China. *Geophysical Journal International, 185*(3), 1321-1334. doi: 10.1111/j.1365-246X.2011.05002.x

Yeck, W. L., Hayes, G. P., McNamara, D. E., Rubinstein, J. L., Barnhart, W. D., Earle, P. S., & Benz, H. M. (2017). Oklahoma experiences largest earthquake during ongoing regional wastewater injection hazard mitigation efforts. *Geophysical Research Letters, 44*(2), 711-717. doi: 10.1002/2016GL071685

Yose, L. A., Eiben, T., Brown, S., Kompanik, G. S., Davis, T. L., & Maxwell, S. R. (2001). 3-D geologic model of a fractured carbonate reservoir, Norman Wells Field, NWT, Canada. *Bulletin of Canadian Petroleum Geology, 49*(1), 86-116. doi: 10.2113/49.1.86

Zhang, H., Eaton, D. W., Li, G., Liu, Y., & Harrington, R. M. (2016). Discriminating induced seismicity from natural earthquakes using moment tensors and source spectra. *Journal of Geophysical Research: Solid Earth*, *121*(2), 972-993. doi: 10.1002/2015JB012603

Zheng, Y. (2018). Transient Pressure Surge in a Fluid-Filled Fracture. *Bulletin of the Seismological Society of America*, 108(3A), 1481-1488. doi: 10.1785/0120170230

Zoback, M. D., & Zoback, M. L. (2002). State of stress in the Earth's lithosphere. *International Handbook of Earthquake and Engineering Seismology* (2002).

Zonneveld, J.-P., MacNaughton, R. B., Utting, J., Beatty, T. W., Pemberton, S. G., & Henderson, C. M. (2010). Sedimentology and ichnology of the Lower Triassic Montney Formation in the Pedigree-Ring/Border-Kahntah River area, northwestern Alberta and northeastern British Columbia. *Bulletin of Canadian Petroleum Geology, 58*(2), 115-140. doi: 10.2113/gscpgbull.58.2.115

Chapter 4

Detection, location and stress drop of induced seismicity in the northern Montney Play, British Columbia, Canada, including the M_w 4.6 hydraulic fracturing induced earthquake

4.1. Introduction

Induced seismicity refers to earthquakes caused by stress and strain perturbations to the Earth crust imposed from anthropogenic activities. Recent studies have shown strong positive correlation between earthquakes in North America and wastewater disposal or hydraulic fracturing (HF) activity (e.g., B.C. Oil and Gas Commission, 2012; Ellsworth, 2013; B.C. Oil and Gas Commission, 2014; Weingarten et al., 2015; Atkinson et al., 2016). For instance, in the central United States, induced earthquakes are triggered by saltwater disposal with pore pressure increase within specific subsurface zones by destabilizing pre-existing faults (e.g., Ellsworth, 2013; Keranen et al., 2014; Weingarten et al., 2015), while in western Canada, HF has been inferred as the main contributor to the drastic increase in seismicity since ~ 2008 (Atkinson et al., 2016). Both poroelastic stress transfer and pore pressure diffusion may act as triggering factors. For example, static stress transmitted by the rock matrix could introduce near-instantaneous stress perturbations at distances of up to ~10 km from the injection point, while fluid pressure diffusion may act immediately within ~1 km of the well bore on short time scales, and with a delayed response at greater distances (e.g., Atkinson et al., 2016; Bao and Eaton, 2016; Deng et al., 2016; Ali et al., 2017; Schulze et al., 2018; Yu et al., 2019). For the past decade, British

Columbia (BC) has become one of the most active regions for unconventional resources exploitation in Western Canada Sedimentary Basin (WCSB), followed by a fast seismic rate increase. Meanwhile, a lot of remaining questions related to the induced earthquakes in BC need to be addressed, for instance, what is the spatial/temporal correlation between injection activity and induced earthquakes? What are the source parameters of induced earthquakes and what implications do the scaling of source parameters have on and implied triggering mechanisms?

Among all of the hydrocarbon plays in the WCSB, the Montney Formation in northeastern BC is one of the primary shale gas and tight gas reserves. With hydrocarbon exploitation activities after 2011 shifting to unconventional reservoir production, the Montney Formation became a primary target reservoir, and seismicity levels increased commensurately with injection activity (e.g., B.C. Oil and Gas Commission, 2012). For instance, 10 M > 3 earthquakes were reported by Natural Resources Canada (NRCan) in the study area shown in Fig.4.1a between 2003 and 2010, compared to 58 M > 3 events between 2011 and 2019, including the M_L 4.6 Fort St. John earthquake, and the November 2018 M_W 4.5 earthquake near Dawson Creek. Meanwhile, a lot of remaining questions related to the induced earthquakes at BC need to be addressed, for instance, the triggering and distribution pattern of induced seismicity to the HF operations, the source parameters and the triggering mechanisms of the induced earthquakes.

On 17 August 2015, one of the largest potentially HF induced earthquakes in western Canada occurred near Fort St John, in northeastern BC, with a reported moment magnitude M_W of 4.6. In this study, we examine in detail the seismicity distribution surrounding the M_W 4.6 and its nearby earthquakes through enhanced earthquake detection and double-difference earthquake relocation, as well as earthquake spectral analysis. The primary objectives of this study are to 1)

establish and quantify correlations between the M_W 4.6 sequence and injection history, and 2) to estimate event source parameters (seismic moment, corner frequency, and hence stress drop values) in order to quantify the magnitude and scaling of stress drop values with event size for large, induced earthquakes. We compare our results with tectonic events, and examine possible correlation with injected volume in an effort to uncover any potential causal links between operational parameters and event size. In the following, we begin by introducing the study area and data acquisition in Section 4.2, followed by a description of earthquake detection using a multi-station matched filter approach (MMF) and refined location methods in Sections 4.3.1 and 4.3.2. We present the spectral analysis procedures (single spectrum and spectral ratio) in Section 4.4, followed by the discussion of our findings and conclusions in Sections 4.5 and 4.6, respectively.

4.2. Data acquisition

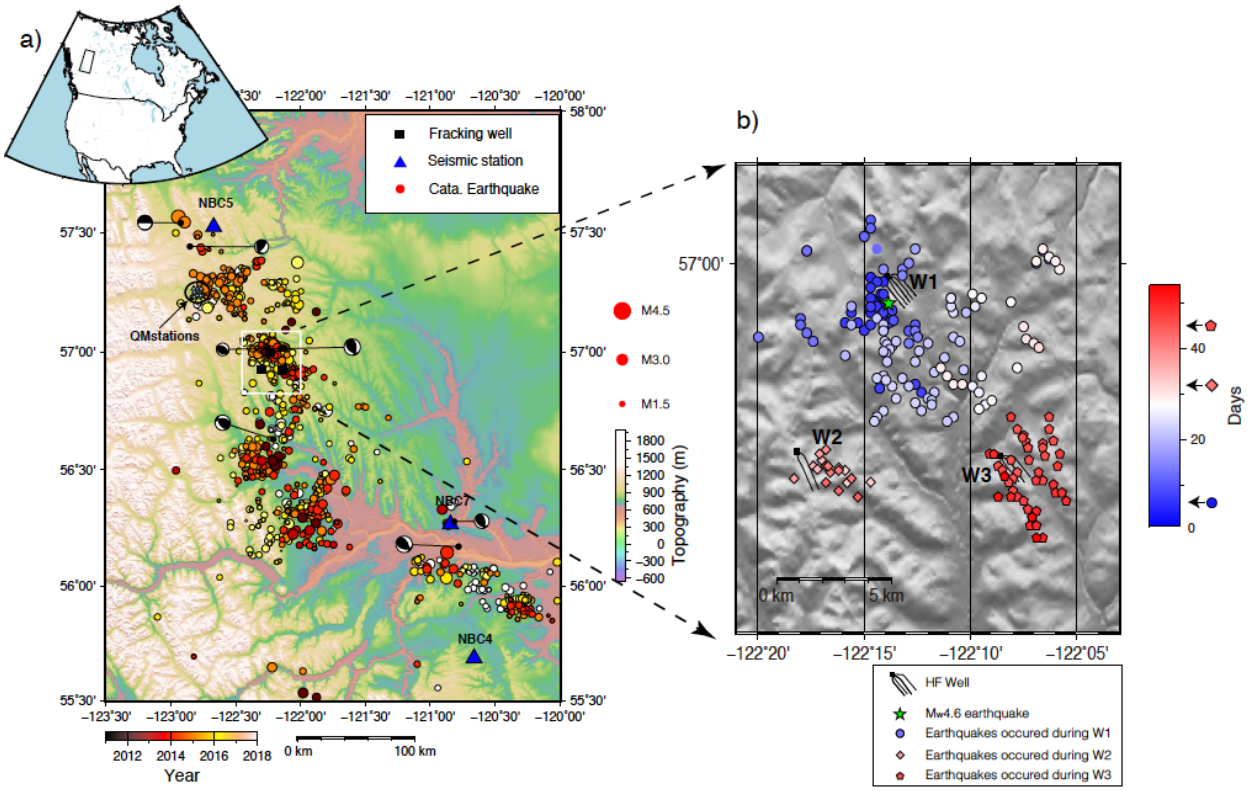

Fig.4.1 (a)Seismicity and seismic stations in northeastern British Columbia for the period from 2011-2018. Earthquake size indicates magnitude, and color indicates the occurrence year. NRCan stations in operation since 2011 shown in dark blue; QM stations operating from 05/10/2015-10/10/2015 shown in light blue. Focal mechanism solutions are from NRCan database. (b) Relative earthquake relocations using the MMF detection, where colors indicate day of occurrence. Horizontal well injection data is from the BCOGC database. The green star indicates the location of the M_w 4.6 mainshock. Symbol shapes differentiate clusters associated with respective hydraulic fracturing wells, W1, W2, and W3.

Here we use data from a temporary deployment of 8 broadband seismic stations (stations MG01 – MG08 of the QM network, with 200 Hz sampling rate) northwest of Fort St. John, supplemented by three NRCan regional stations (CN, 100 Hz sampling rate), to study HF induced seismicity (Fig.4.1). The QM stations recorded data from 13 May to 7 October 2015, but we use data from the 11 August 2015 to 7 October 2015 for the analysis here, as activity in the study area was negligible before then. Four of the QM stations had unlocked GPS signals during part of the deployment period, which caused a non-negligible timing error. We applied an ambient noise correction to reduce timing error from ~1 s to ~0.1 s (details of the correction and the approach applied can be found in the Text.A1 in appendix and in Yu et al., 2019). Fig.4.1a shows the locations of the study area which is roughly 50 km to the southwest of the QM seismic stations, and the HF wells proximal to the 17 August 2015 M_w 4.6 earthquake.

4.3. Enhanced catalog and event location

After the seismic data acquisition from NRCan and QM stations, then we use the data for earthquake detection, location and relocation, source parameter estimation for the period from 08/11/2015 to 10/07/2015.

4.3.1. Enhanced catalog building using a MMF detection approach

The NRCan catalog contains 25 events during the time window of this study (11 August – 7 October) ranging in magnitude from 1.4 to 4.6. In order to increase the number of detected earthquakes, we perform an enhanced detection using an MMF approach. The MMF approach searches for signals in the continuous waveforms that are similar to the template events by cross-correlating templates across stations and summing the cross-correlation coefficients (Skoumal et al., 2015). When the summed correlation coefficients exceed some pre-determined threshold, a detection is declared. We follow the methods of Wang et al. (2018) to detect additional earthquakes using continuous waveforms from the 8 QM stations and 3 NRCan stations (Fig.4.1a), with five earthquakes occurring in the week after the M_w 4.6 earthquake (M_w 1.4 – 4.6) as templates.

Prior to performing the cross-correlation, we remove the instrument response and apply a band-pass filter of 5-15 Hz to both the templates and the continuous waveforms, which is the frequency band of dominant energy of the micro earthquakes in this study. We then calculate the cross correlation (CC) values with templates through the continuous waveforms of each station at time steps of 0.01 s. We allow time window shifts up to 2 s between stations by maximizing CC values before summing in order to detect earthquakes with hypocenters that vary from template locations. A candidate for detection is declared when the CC value exceeds 18 times the mean absolute deviation (MAD) value, which is the 75^{th} percentile for a symmetric distribution with zero mean. We also visually inspect all MAD declared detections to remove false detections (The false detections we referred to here are the detections with less than 5 phase picks that can not subsequently be used for hypocenter location). The above procedure results in a total of 468 automatic detections, and 323 true detections after visual inspection, hence a false detection rate

of ~ 31%.

4.3.2. Location, double-difference relocations, and injection volume timing

We first compute absolute event locations for the 323 individual detections outlined in Section 3.1 using the CRUST 1.0 velocity model with the 1° × 1° box centered at 57.5°N, 122.5°W (Laske et al., 2013; Fig.4.2) as an input velocity model, and manually picked P and S-wave arrival times. Some larger events also contained phase picks from the more distal NBC4 and NBC7 stations, where it was possible to constrain phase arrivals using cross-correlation time lags (see Fig.4.3 for an example of such picks). Once phases are picked, we estimate hypocenters of the 323 MMF detections in a two-step approach, first using a coarse grid matrix search followed by initial location and origin time refinement with a nonlinear iterative method. The details of the two-step grid search method are explained in the Text.A2 and Fig.A.1.

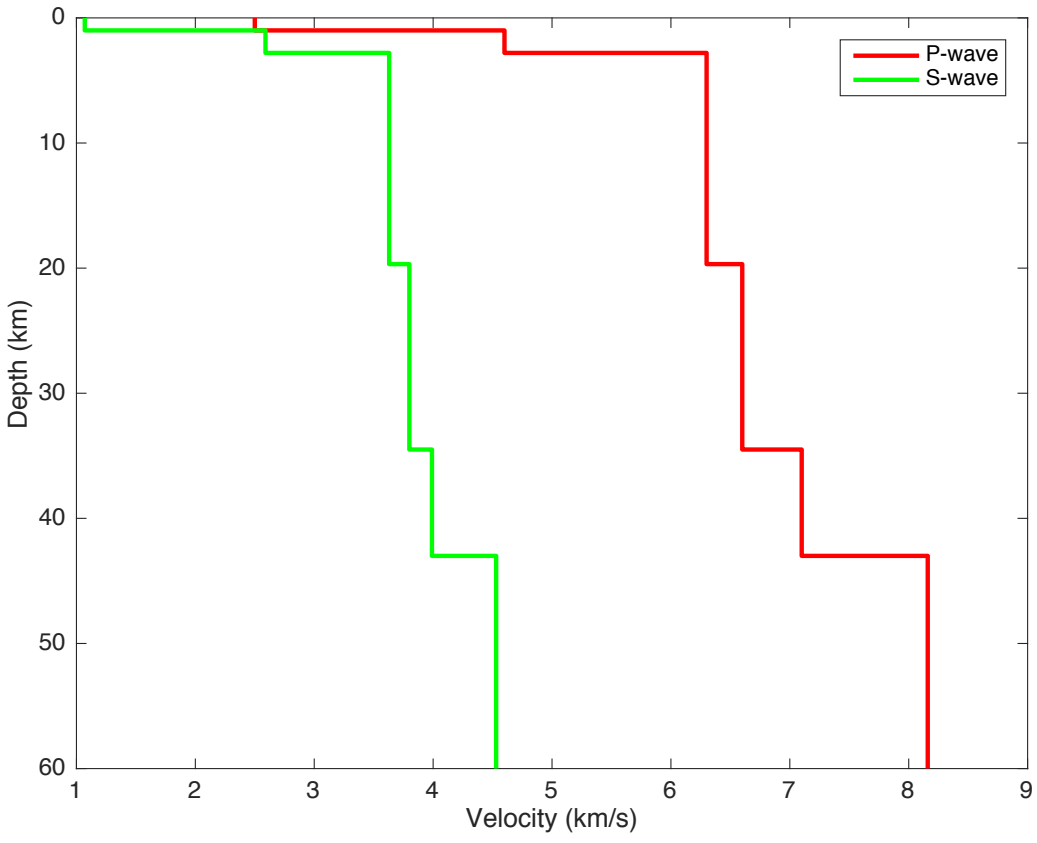

Fig.4.2 Velocity model used for the earthquake location and relocation from Laske et al. (2013).

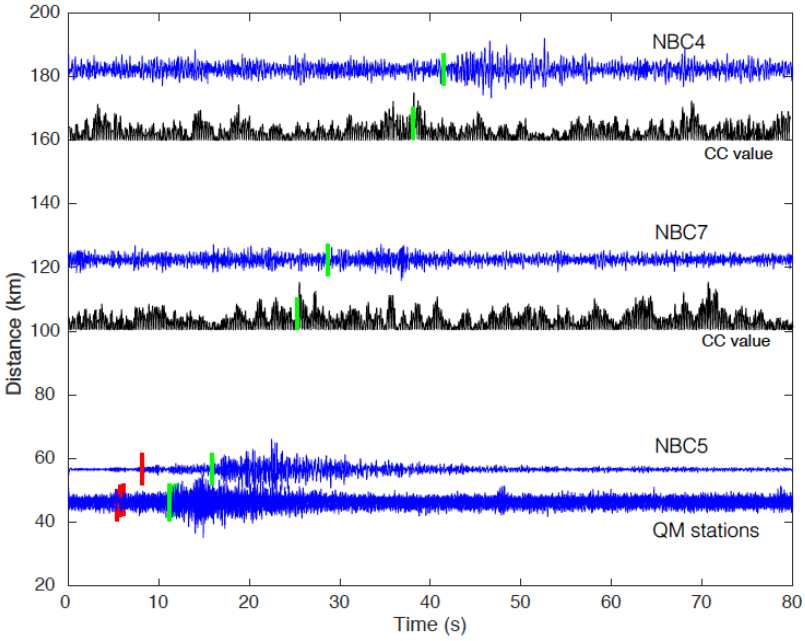

Fig.4.3 Phase arrival picks by cross-correlating high SNR signals from MG04 to low SNR signals at NBC7 and NBC4. The full waveforms on horizontal components are shown in blue (note that several waveforms from QM stations are overlapping), and below the waveforms are the normalized CC values. Red vertical lines correspond to P wave arrival times, and green vertical lines denote the S wave arrival time and the highest CC values.

To further improve the relative locations of the initial hypocenters, we employ a double-difference relocation approach hypoDD (Waldhauser and Ellsworth, 2000). We use the parameter settings in the hypoDD inversion listed in Tab.4.1, which let us to retain 191 of the initial 323 detections. We calculate the spatial uncertainty of relocated hypocenters by using a bootstrap random replacement error estimation based on 1000 trials (Efron and Tibshirani,1986), where errors range up to ~2.8 km, and are listed in Tab.A1. We impose a quality control criterion of 3 km/2 km for horizontal and vertical error, respectively. Fig.4.1b shows the 191 relocated events in the time period from 11 August to 07 October 2015. The color bar and spatial grouping

suggests three earthquake sequences correlate spatially with nearby HF well injection activity, and that a majority of the earthquakes occur during injection periods at the most proximal HF well. Fig.4.1b also suggests (at least at W1) a seismicity migration pattern where earthquakes occur at greater distances from the well at progressively later points in time. The spatial/temporal migration of the event cluster near W1 also shows similar behavior to the seismicity associated with pumping closer to the network of QM stations, and may be related to pore pressure diffusion within 5 km of the well (Yu et al., 2019).

Dtimes of P phase			Dtimes of S phase						
CT		CC	CT		CC		OBSCT		OBSCC
14912		1160	35937		2474		6		4
NITER	WTCCP	WTCCS	WRCC	WDCC	WTCTP	WTCTS	WRCT	WDCT	DAMP
5	0.01	0.005	-9	-9	1	0.5	-9	-9	150
5	0.01	0.005	-9	2	1	0.5	6	4	150
5	1	0.5	-9	2	0.01	0.005	6	4	150
5	1	0.5	5	2	0.01	0.005	6	4	150
5	1	0.5	5	2	0.01	0.005	6	4	150

Tab.4.1 Parameters used for the HypoDD relocation. Dtimes: the total number of travel time differences for cataloged travel time difference (CT) and cross-correlated travel time difference (CC, with value > 0.7). OBSCT/OBSCC: the minimum number threshold for event pair to form a continuous cluster. Niter: the number of iterations used for each step. WTCCP, WTCCS, WTCTP, WTCTS are the weights for the four data types, and WRCC, WRCT, WDCC, WDCT are the characteristics of the re-weighting functions. DAMP is the damping factor.

We then compute local earthquake magnitude M_L of the 191 relocated hypocenters by using the peak S-wave amplitude and averaging over all stations, and seismic moment M_0 by fitting the long-period spectral amplitude with a Brune spectral model (details for M_L can be found in

supplementary material, and for M_0 can be found in Section 4.4). Fig.4.4 shows the cumulative moment value and earthquake occurrence based on the 191 relocated events shown together with the cumulative injection volume during the HF period for three wells (W1, W2 and W3 in Fig.4.1b) as reported in the BC Oil and Gas Commission database, which suggests a complex relationship between the rate of induced earthquake nucleation at individual wells with respect to daily and cumulative injection volume. First, the lag time between the onset of injection and the onset of seismicity differs between sites: there is a ~5-day lag at W1, a ~1-day lag at W2, and ~1-day lag W3. Second, there is a spike in seismicity on 09/02/2015 (day 23) preceded by a small peak in daily injection volume two days prior, and a small jump in the cumulative injection volume (due to the relative volume injected compared to the first 10 days of the curve). Close examination of the location of the cluster on day 23 shows that it began south of the horizontal terminus of the active W1, in close proximity to the M_w 4.6 mainshock and its aftershock sequence. The location of the seismicity suggests a reactivation (further stress perturbation on) of the same fault system associated with the mainshock. Third, there is lower seismicity response to injection at W2 compared to W1 and W3, and one plausible explanation for this is that the total injected volume is less, which is also consistent with the conclusions reached by Schulz et al. (2018), namely that the cumulative amount of injected fluid may be the dominant factor in generating induced seismicity.

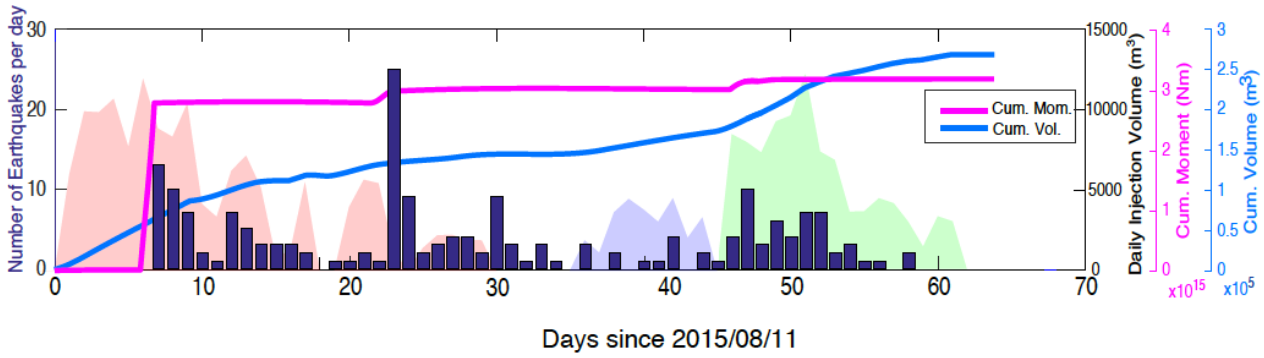

Fig.4.4 Daily seismicity versus the injection data. Daily injection data is indicated with the shaded areas, where color denotes the injection activity for the different HF wells, red shaded areas denotes W1 injection, blue shaded areas denotes W2 injection and green shaded areas denotes W3 injection. The purple line indicates the cumulative moment for the detected earthquakes shown in the histogram, and the blue line denotes the cumulative injection volume for the three HF wells. The time starts from 2015/08/11, one day before the start of HF operation at W1.

4.4. Static stress drop estimates

Making robust estimates of earthquake stress drop values requires careful consideration of bandwidth limitations and correction for non-source related effects. To estimate source parameters to M_0 and f_c, we first use single event displacement spectra to constrain M_0 using the long period spectral amplitude, Ω_0, and to provide initial estimates of f_c assuming a constant quality factor (i.e., attenuation), which is described in Section 4.4.1. Assuming a constant attenuation often leads to underestimates of corner frequency, particularly for M < 4 earthquakes (e.g., Viegas et al., 2010; Abercrombie et al., 2017). The problem of f_c underestimation can be mitigated by estimating corner frequencies from spectral ratios of co-located event pairs, which has the effect of canceling non-source related effects between earthquake spectra. We therefore refine initial estimates of spectral corner frequencies for event pairs with similar waveforms and a high signal-to-noise ratio over the frequency band of interest (detailed in Section 4.4.2). In

Section 4.4.3, we use the M_0 and f_c estimates to calculate values of static stress drop, where values calculated using refined f_c estimates are assumed to be more accurate due to minimizing non-source related effects via the spectral ratio estimation (e.g., Ide et al., 2003, Harrington et al., 2015).

4.4.1 Seismic moment and corner frequency values estimated using single spectra

We start with instrument response corrected displacement recordings of earthquakes and calculate the phase (P and S) spectra using time windows of 4 and 2 s for earthquakes with magnitudes of M > 4 and M < 4, respectively. Time windows start 0.1 second before the phase arrival, and spectral estimates are performed using a multi-taper spectral estimation on individual components (Thomson, 1982). We compute noise spectra using noise waveform of identical time windows directly preceding the P-wave arrival by 5 s (for cases without P wave arrival, we use 12 s directly preceding the S wave arrival, considering a ~50 km epicentral distance). We use a Brune spectral model to fit values of Ω_0 and f_c (Brune 1970, 1971) on the power spectrum vector sum of all 3 components (for both signal and noise) as seen in Eq.4.1

$$\Omega(f) = \sqrt{\Omega_{HHZ}(f)^2 + \Omega_{HHN}(f)^2 + \Omega_{HHE}(f)^2}, \quad (4.1)$$

where the analytical expression for the Brune spectrum is given by Eq.4.2 ,

$$\Omega(f) = \frac{\Omega_0 e^{-\frac{\pi f t}{Q}}}{[1+(\frac{f}{f_c})^{\gamma n}]^{\frac{1}{\gamma}}} \ . \quad (4.2)$$

The parameter t is the travel time, f is the spectral frequency, f_c is the corner frequency, n is the high-frequency fall-off rate, γ is a constant, and Q is the quality factor. Here, we follow the method described by Abercrombie (1995) for Model 2, that assuming a constant Q = 1000 for both P and S waves, a value of γ = 2, with n as an additional free parameter (to Ω_0 and f_c) that

varies between 1 and 4, we then use the MATLAB least squares curve fitting algorithm to perform the fitting. We estimate 95% confidence intervals with the asymptotic normal distribution method using the residuals calculated from 'Lsqcurfit'. The band over which the spectra and spectral ratios are fit is not fixed, but dictated by the following factors: a) The SNR > 2 over a bandwidth of at least 15 Hz (we also retain some of the fittings with bandwidth > 10 Hz, which has stable long-period amplitude estimations), and b) the fitted f_c value is higher/lower than the first/last three spectra data points. In addition, all spectra fitting results have been reviewed to remove qualitatively poor fits. In total we have 135 single spectrum fits of the 191 events with high-quality locations. Two representative examples of the single spectrum fits for P and S phases can be found in Fig.4.5. After applying the above quality-control criteria, we retain spectral parameter estimates for 135 of the original 191 events.

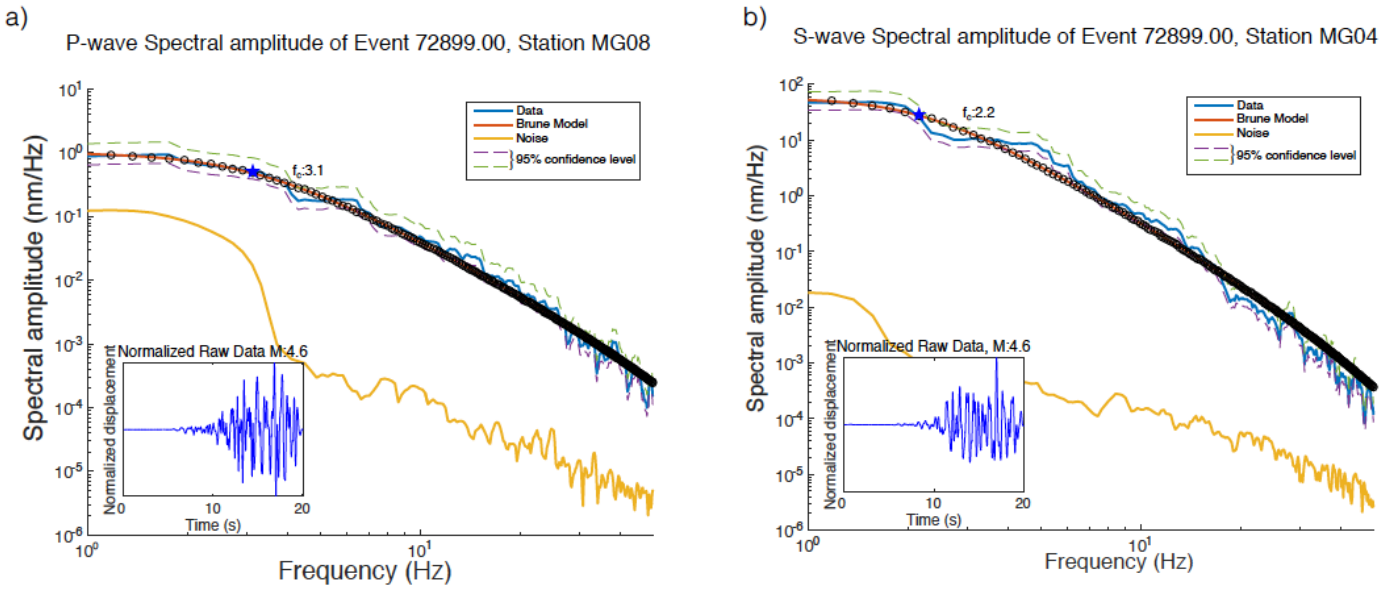

Fig.4.5 Examples for single spectral fitting. Left panel: Least square curve fits of P-phase spectra for Event 2015/08/17 M_w 4.6 recorded on MG08. Right panel: Least square curve fits of S phase spectra for the same event recorded on MG03. Bottom left windows show the normalized raw data on displacement for the two events.

Finally, the seismic moment values are calculated using the estimated Ω_0 and averaging over all stations in the following relation (Keilis-Borok, 1960),

$$M_0 = \frac{4\pi\rho c^3 R\Omega_0}{U_{\phi\theta}} \qquad (4.3)$$

where c is the seismic wave velocity (here we assume a constant velocity versus depth, due to the poor constraints on depth), R is the hypocentral distance, ρ is the density, and the mean radiation pattern U is assumed to be 0.52 and 0.63 for P waves and S waves, respectively (Aki and Richards, 2002). The moment uncertainties are estimated following the jackknife uncertainty estimation method (Efron, 1981; Prieto, et al., 2007).

4.4.2 Corner frequency values estimated using spectral ratios

Once we have the initial estimates of f_c from the single spectra fitting, we use a spectral ratio approach to refine f_c estimation. The single event earthquake spectrum contains energy related to the earthquake source, but also information regarding travel path, instrument response, and site effects. Taking the ratio of two co-located earthquake spectra effectively cancels all non-source related terms within the spectra, thereby removing any bias or influence on the spectral corner frequency (e.g., Ide et al., 2003; Viegas et al., 2010; Abercrombie 2013; Abercrombie et al., 2017). We refer the reader to (e.g., Ide et al., 2003; Abercrombie 2013; Shearer et al., 2019) for a detailed background on spectral ratio approaches.

Effectively fitting one or two of the event corner frequencies in a spectral ratio pair requires identifying two co-located events (assumed through waveform similarity), with a resolvable difference in corner frequency. Generally, events with nearly an order of difference in moment have corner frequencies that differ sufficiently to be resolved in spectral fitting. Here we refer to

the larger magnitude event as the master event and the smaller magnitude event as the eGf (empirical Green's function). We use the following criteria for event pair selection:1) the magnitude difference between the master and the eGf event must be at least 0.5 units to help ensure resolvable f_c values (notice that eGfs should have the same time window length to the master events), 2) the catalog location distance between events in a pair may not exceed 5 km, and 3) the cross-correlation coefficient (CC) value threshold of 0.7 must be exceeded for P and S-phases within individual event pairs. The latter two criteria will only be fulfilled for approximately collocated events with similar focal mechanisms.

We use the same approach to spectral estimation as detailed above for the single event spectra, with the exception that the instrument response is not removed, as it cancels in the spectral ratio. We follow the approach of Huang et al. (2016) for each event pair by stacking spectral ratios of all stations that fulfill the criteria for event pairs listed above. Stacking the spectral ratios across stations produces better constrained parameter fits by reducing noise and radiation pattern effects compared to fitting spectral ratios calculated from a single station (Huang et al., 2016, Abercrombie et al., 2017). We then fit the stacked spectral ratios using the analytical expression for the ratio of two Brune spectra (Brune, 1970，1971),

$$\frac{M_1(f)}{M_2(f)} = \frac{\Omega_{01}}{\Omega_{02}} \left(\frac{1+\left(\frac{f}{f_{c1}}\right)^{\gamma n}}{1+\left(\frac{f}{f_{c2}}\right)^{\gamma n}} \right)^{\frac{1}{\gamma}} \qquad (4.4)$$

where f_{c1} and f_{c2} and Ω_{01} and Ω_{02} are the corner frequencies and long-period spectral amplitude values for the master and eGf events, respectively. In fitting with the Brune model, the high-frequency falloff, n, and γ are fixed constants set to n = 2, and γ = 1 (e.g., Viegas et al., 2010; Abercrombie, 2014; Abercrombie et al., 2017; Shearer et al., 2019). The free parameter

values (i.e., Ω_{01}, Ω_{02}, f_{c1}, and f_{c2}) listed above are also fit using the least square curve fitting algorithm in MATLAB, which minimizes the function residual. While the high and low frequency amplitudes of the ratio are fit, we only retain the estimated f_{c1}, and f_{c2} values for refinement. The long period amplitude values from the single spectrum fitting are used for the moment and magnitude estimations, as they are less affected by attenuation compared to spectral estimates at higher frequencies (such as the corner frequency).

We retain the refined f_c parameter estimates from the spectral ratio fits based on several imposed criteria. First, the fitted f_{c1} value (master event) should be at least 4 data points larger than the low-frequency limit of fitting. Second, we perform a grid-search in increments of 0.1 Hz surrounding the best-fit values of f_{c1} and f_{c2} where the misfit values are calculated for each of the fixed f_c values in the grid search (e.g., Viegas et al., 2010; Abercrombie, 2017). We discard event pairs for which the grid-search misfit curve does not have a parabolic shape (Fig.4.6), and we require the corner frequency uncertainty corresponding to a 5% perturbation of the best-fit f_{c1} value differ by less than a factor of two ($(f_{c1max} - f_{c1min})/f_{c1} = f_{c1\_err} \leq 2$) following the study of Abercrombie (2014). Finally, we retain the f_{c1} and f_{c2} estimates with the minimum variance for each event pair, where the errors are determined from the 95% confidence interval of the misfits calculated via the grid search. An example of a spectral ratio pair using the M_W 4.6 mainshock is shown in Fig.4.6.

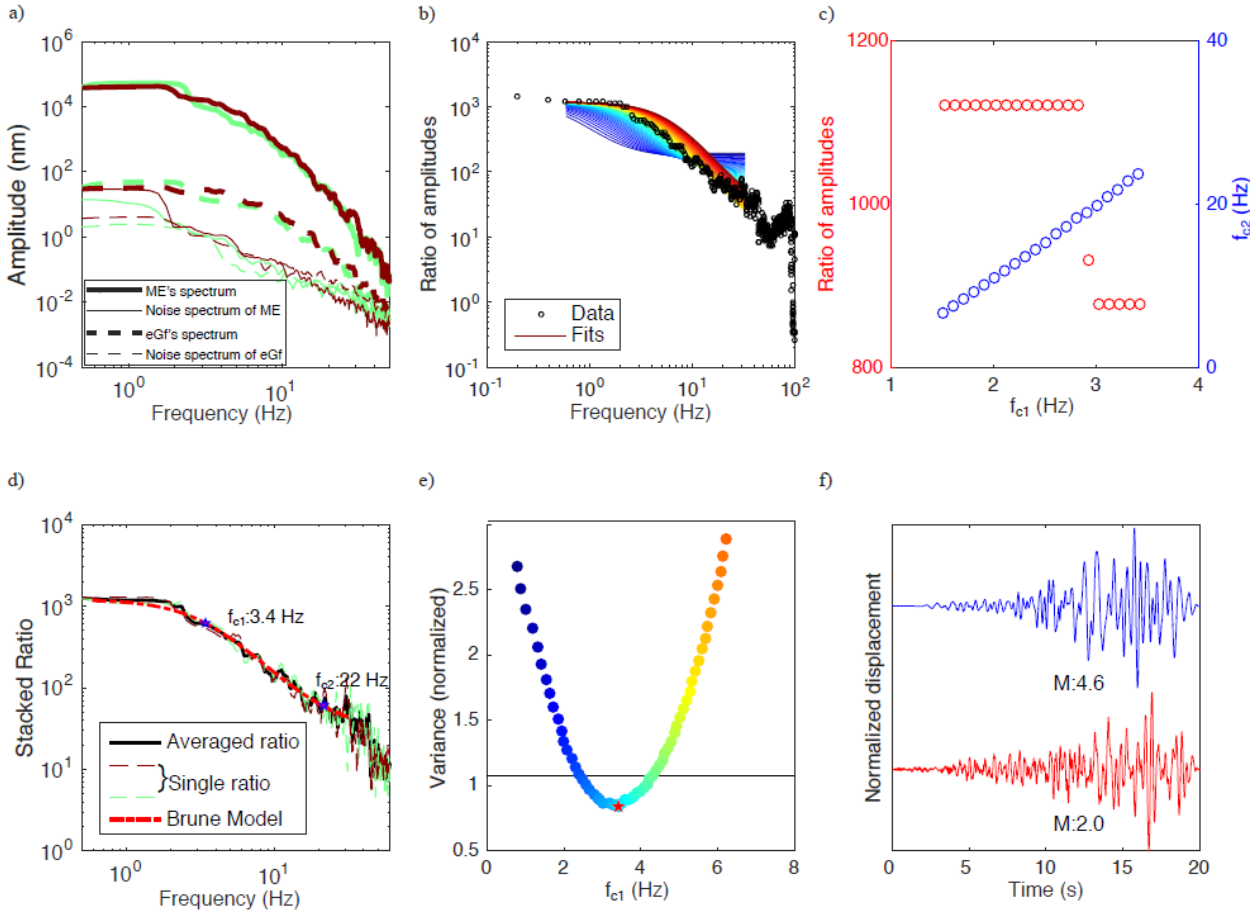

Fig.4.6 Representative example of spectral ratio fitting procedure to estimate corner frequency. (a) Vector spectral amplitude (thick line) and noise spectra (thin line) of one master event (solid line) and one eGf (dashed line). Each color denotes a spectrum recorded on an individual station. (b) Corresponding data fits for the incremental perturbation of f_{c1} values, with corresponding misfit shown below in panel (f). Color convention corresponds to that used in (f). (c) Corresponding fits of long-period spectral amplitude ratio Ω_{01}/Ω_{02}, and f_{c2} between master event and eGf for the f_{c1} increments shown in (b). (d) The best average fit of values f_{c1} and f_{c2} for a Brune spectral model of the stacked spectral ratio. When multiple secondary events are available, the f_{c1} value is calculated using the weighted mean (see text). Same color convention is used as in (a). (e) The misfit of incremented values of f_{c1}, where each fixed f_{c1} value is represented by a different color. (f) The waveforms in the time domain for both the master event and eGf on one horizontal component.

Where a master event is associated with multiple eGfs, hence multiple corner frequency estimates are possible for the master event, we calculate the representative corner frequency of

the master event as the weighted mean of the corner frequency values estimated as described above. We calculated the weighted mean and standard deviation using the inverse-variance weighting method (e.g., Abercrombie, 2014), with the following two equations:

$$\hat{\gamma} = \frac{\sum_i(\frac{\gamma_i}{\sigma_i{}^2})}{\sum_i(\frac{1}{\sigma_i{}^2})}, \quad D^2(\hat{\gamma}) = \frac{1}{\sum_i(\frac{1}{\sigma_i{}^2})} \qquad (4.5)$$

where $\hat{\gamma}$ is the weighted mean f_c, γ_i is the ith measurement, σ_i the variance, and D is the standard deviation of the weighted mean. Notice that the f_{c2} estimation is often disregarded in the weighted mean corner frequency calculation because it commonly lies out of the bandwidth with SNR > 2. Other studies have also show poorer resolution and less stability in f_{c2} estimates, thus only f_{c1} values are reported in Fig.4.7 (Viegas et al., 2010; Abercrombie, 2013) Tab.A2 lists all of the weighted mean f_{c1} estimates with standard deviation values obtained for each of the secondary events for cases where multiple eGfs fulfilled event pair and fitting criteria.

4.4.3 Static stress drop estimation

Using values of M_0 and f_c estimated from single spectrum fitting, and refined f_c values from spectra ratio fitting, we calculate the stress drop for the earthquakes using a circular crack model (Eshelby, 1957):

$$\Delta\sigma = \frac{7}{16}\frac{M_0}{r^3} \qquad (4.6)$$

$$r = \frac{kv}{f_c} \qquad (4.7)$$

where $\Delta\sigma$ is the static stress drop, M_0 is the seismic moment, r is the source radius, v is the phase (P or S) velocity at the source, and k is a constant. Here we assume values of 5 km/s and 2.8 km/s for the P-wave and S-wave velocities, respectively, and use the following to calculate k,

$$k = \frac{C}{2\pi} \qquad (4.8)$$

where C is 1.6 for P waves and 1.99 for S waves, assuming a rupture velocity equal to 90% of the shear wave velocity (Sato and Hirasawa, 1973). These parameters from Sato and Hirasawa model lead to a ratio of P to S wave corner frequencies ~1.4, which is more suitable for our ratio range with ~0.9-1.1 estimated from spectral ratio method (Fig.4.7a). Fig.4.7 shows the stress drop values calculated with corner frequencies estimated from single spectra and spectral ratio fitting.

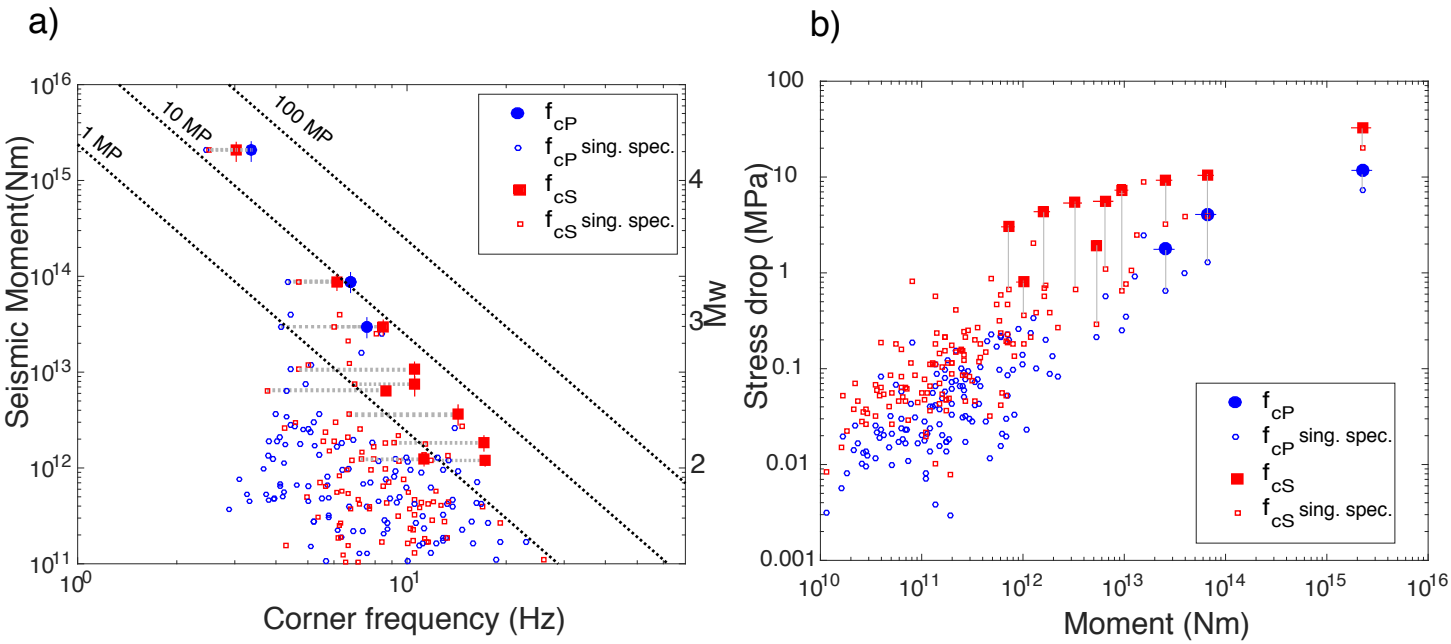

Fig.4.7 Single spectrum moment and corner frequency values and spectral-ratio refined corner frequency values with corresponding static stress drop estimations. (a) Solid circles and squares indicate the corner frequencies for P and S waves estimated using the spectral ratio approach, respectively; empty circles and squares denote corner frequencies for P and S waves from the single spectrum fitting, respectively. Black dashed lines mark lines of constant stress drop based on a constant S wave speed of 2800 m/s. (b) Stress drop values versus station-averaged moment values.

Fig.4.7 indicates that the corner frequency estimates from single spectrum fitting are likely underestimated, and that the spectral ratio estimates are more robustly correct for non-source

related effects, thereby providing better constrained f_c estimates, as suggested by many previous studies (e.g., Ide et al., 2003; Viegas et al., 2010; Harrington et al., 2015).

4.5. Discussion

Kao et al., (2018) found a lack of a clear pattern between the onset of injection and the delay of seismic activity in northeastern BC, a feature that makes assessment and management of seismic hazard difficult. One possible explanation for the ~5-day lag observed at W1 could be that the pre-existing fault (inferred from *b*-value < 1, see Text.A3 and Fig.4.8) on which the M_w 4.6 mainshock occurred was not critically stressed when injection started, and that the elapsed time and volume of fluid injected was sufficient to allow fluids to migrate into the fault due to proximity to W1. High permeability of the conduit-like structures might also enhance the diffusivity between the HF wells and the pre-existing fault, leading to a faster accumulated fluid mass and elevated pore pressure that could bring the fault to failure over the 5-day period. In comparison, for the 1-day lag at W2 and W3, this might be due to the stress perturbations generated from the continuous HF pumping at W1 already altering the stress conditions at W2 and W3 through rock matrix or pore-fluid pressure migration, bringing proximal faults closer to a critically stressed state, event before the pumping of W2 and W3 began (e.g., Deng et al., 2016; Goebel et al., 2017; Yu et al., 2019). If the interpretation is correct, it would imply that only relatively small volumes of fluid were needed to create an immediate response once pumping started.

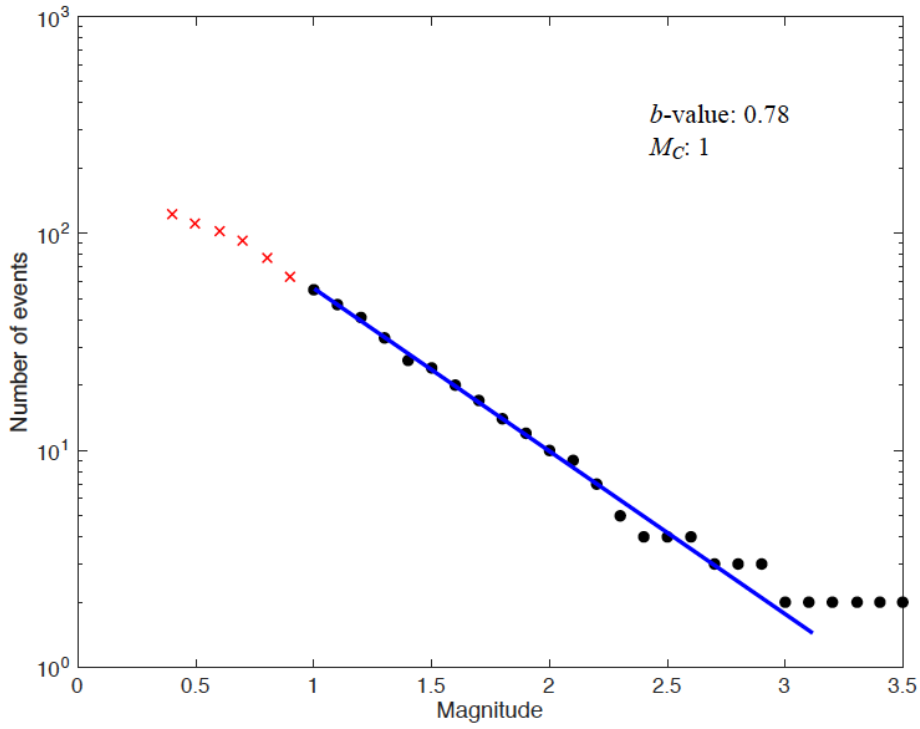

Fig.4.8 *b*-value and catalog completeness M_C for the relocated earthquakes related to W1 based on the maximum likelihood method, black dots represent the earthquakes above catalog completeness and the x points represent below.

We calculate the cumulative reported injection volume in proximity to the M_w 4.6 earthquake to see where the mainshock stands in the McGarr (2014) proposed relation between the maximum induced magnitude and cumulative injection volume. We find that the M_W 4.6 event lies above the upper threshold line (see Fig.4.9), suggesting that the magnitude may more likely be controlled by the tectonic environment, as suggested by van der Elst et al. (2016). An interpretation of the tectonic conditions controlling maximum magnitude are also suggested by the estimated *b*-value of 0.78 (see Text.S3) and is supported by the interpretation of Atkinson et al. (2016), who suggest that the upper magnitude limit of the HF induced seismicity could be controlled by the size of available fault surface.

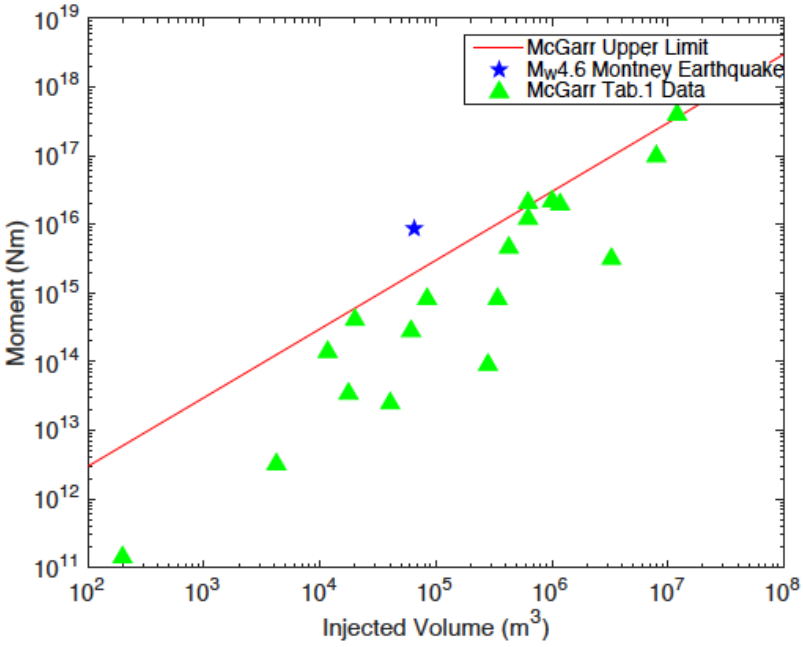

Fig.4.9 The maximum observed magnitude versus the total injected volume when the earthquake occurs. Green triangles denote the reproduced data from Table 1 of McGarr (2014), and the blue star denotes the M_W 4.6 earthquake in this study. The red line represents the McGarr moment cap.

The main drawback of the spectral ratio method is that it typically reduces the number of events for which the method can be applied (due to co-location and magnitude difference requirements), which is demonstrated here with the 13 refined corner frequency estimates (3 for P waves and 10 for S waves, Fig.4.7) we obtain, compared to the 191 relocated events in the catalog. For our data set, the main restricting factor that reduces the number of available event pairs is that most of the eGfs have relatively small magnitudes (M_w < 1.0), and thus have difficulties meeting the SNR requirements.

The SNR of the surface stations in this study typically reaches 1 at frequencies of roughly 30-40 Hz, meaning that corner frequencies of earthquakes with M_w < 2 become difficult to

resolve (e.g., a M_w 2 event with a stress drop of 1-10MPa should have a f_c ~15-30 Hz for *S*-waves). The smallest main event for which we refine the corner frequency has a magnitude of ~M_w 1.9, meaning that we can not rule out the possibility that the step-like feature in the stress drop estimates shown in Fig.4.7 for the relatively small earthquakes could be caused by frequency bandwidth limitations (e.g., Boatwright, 1994; Viegas et al. 2010; Onwuemeka et al., 2018). In addition, we assume a constant shear wave velocity when we calculate the stress drop, which sometime can lead to an artificial dependence with depth shallower than 5 km (e.g., Allmann and Shearer, 2007), however, due to the poor depth constraints, it is not possible for us to inhibit the influence on scaling of assuming the constant velocity.

While some studies suggest that the stress drop values of induced earthquakes are lower than their tectonic counterparts, there are also documented cases of induced earthquakes in the WCSB having stress drop values that are on the high side (~100 MPa) of the typical range of tectonic events (e.g., Hough, 2014; Goertz-Allman et al., 2011; Clerc et al., 2016). Here we find stress drop values from P-waves ranging from 1.9 MPa to 15.2 MPa with a median of 6.5 MPa, and from S-waves ranging from 0.9 MPa to 33.8 MPa with a median of 6.6 MPa (Fig.4.7). The range of values is relatively small compared to other studies, which document up to 3 orders of magnitude difference in the stress values (e.g., Abercrombie,1995; Clerc et al., 2016), albeit with a larger number of events. Furthermore, stress drop values estimated with spectral ratios do not show any significant scaling with event magnitude (within the 1-10 MPa range), indicating that stress drop values for induced earthquakes may exhibit self-similar behavior, similar to their tectonic counterparts, (e.g., Abercrombie 1995; Kwiatek et al., 2010; Goertz-Allman et al 2011; Clerc et al., 2016). The stress drop values estimated here fall within the typical range reported for

tectonic events, and are somewhat lower than other examples of induced seismicity in the WCSB, including the induced earthquake sequence at Fox Creek, Alberta which had estimated stress drop values ranging from 10 MPa to 100 MPa by Clerc et al. (2016) using the Boatwright model, and a range of 2-90 MPa for induced earthquakes over a wider spatial distribution in the WCSB with single spectral fitting method (Zhang et al., 2016).

4.6. Conclusions

We detect more than three hundred induced earthquakes between 08/11/2015 and 10/07/2015 proximal to the 17 August 2015 M_w 4.6 earthquake sequence near Fort St. John, British Columbia using an MMF method, and relocate 191 earthquakes with horizontal/vertical errors < 3 km (Fig.4.1b), which exceed the number of NRCan cataloged earthquakes by a factor of ~10 times for the same period. Estimated stress drop values range from 0.9 and 33.8 MPa are relatively smaller compared to other stress drop estimates of HF induced earthquakes in the WCSB. The delayed seismic response to pumping at W1 supports Kao et al.'s (2018) conclusions that a lack of a clear pattern makes seismic hazard assessment difficult if based on operational parameters alone. Variations in lag times at wells, *b*-value of 0.78 (similar to other tectonic areas), the M_w 4.6 lying outside the McGarr curve, in addition to the range of stress drop values observed, suggest that the fault (or fault system) on which the M_w 4.6 was generated was pre-existing, and thus governed by the same statistics we use to quantify behavior on tectonic faults (i.e., concurs with van der Elst et al.'s (2016) conclusions). Therefore, to reduce the potential risks of large HF induced earthquakes similar to this M_w 4.6 mainshock at Fort St. John, proximity of HF wells to pre-existing fault structures should be a factor considered in seismic hazard estimation, because this can enable activating a fault network beyond the reach of the

well.

4.7 Appendix

Tab.A1 The catalog for the relocated earthquakes, together with the horizontal/vertical errors in km calculated from 1000 bootstrap trials.

Year	Month	Day	Hour	Min	Sec	Lon	Lat	E_h(km)	E_z(km)	Depth(km)
2015	8	17	20	15	0.56	-122.231	56.983	2.42	0.87	3.5
2015	8	17	20	22	2.32	-122.24	56.983	0.925	0.084	2.6
2015	8	17	20	24	13.16	-122.243	56.985	1.485	0.176	2.4
2015	8	17	20	26	10.1	-122.237	56.982	0.53	0.164	1.9
2015	8	17	20	26	53.62	-122.235	56.977	0.9	0.228	2.3
2015	8	17	20	28	38.1	-122.233	56.975	1.08	0.212	2.1
2015	8	17	20	34	12.08	-122.245	56.98	0.395	0.1	2.9
2015	8	17	21	0	13.92	-122.238	56.982	0.735	0.26	1.1
2015	8	17	21	37	37.29	-122.235	56.993	2.475	0.316	1.5
2015	8	17	22	0	12.97	-122.233	56.987	2.205	0.328	1.2
2015	8	17	22	4	44.78	-122.237	56.987	0.54	0.148	1.5
2015	8	17	23	42	39.16	-122.235	56.993	2.18	0.244	1.3
2015	8	17	23	46	21.92	-122.245	56.994	0.765	0.168	1.2
2015	8	18	0	9	19.72	-122.243	56.99	1.155	0.256	2.4
2015	8	18	0	52	26.32	-122.24	56.993	0.89	0.128	2
2015	8	18	1	23	23.95	-122.235	56.987	0.715	0.088	1.4
2015	8	18	2	21	40.72	-122.245	56.99	1.37	0.768	2.5
2015	8	18	3	18	45.4	-122.24	56.982	1.865	0.328	1.6
2015	8	18	3	43	34.09	-122.26	56.98	2.805	0.172	3.9
2015	8	18	4	45	31.41	-122.265	56.976	0.765	0.164	1.1
2015	8	18	5	26	39.45	-122.255	56.976	1.795	0.212	2.4
2015	8	18	6	25	29.43	-122.25	56.973	0.87	0.256	1.2
2015	8	18	11	39	8.12	-122.245	56.986	0.94	0.572	2
2015	8	19	6	9	12.09	-122.238	56.949	0.89	0.256	1.5
2015	8	19	9	9	7.79	-122.205	56.947	2.565	0.364	2.4
2015	8	19	9	16	53.53	-122.21	56.951	1.795	0.64	3.2

2015	8	19	12	43	8.52	-122.245	56.982	0.98	0.184	1
2015	8	19	12	56	13.87	-122.235	56.98	2.65	0.244	3.4
2015	8	19	13	33	17.68	-122.228	56.981	0.65	0.096	1.3
2015	8	19	16	16	53.58	-122.245	56.975	0.46	0.2	0.6
2015	8	20	3	24	4.73	-122.235	56.973	0.405	0.156	2
2015	8	20	9	54	11.07	-122.23	56.976	1.86	0.244	1.4
2015	8	21	15	3	40.07	-122.227	56.977	2.625	0.264	1.4
2015	8	22	8	6	59.95	-122.115	57	2.695	0.124	4.2
2015	8	22	8	14	28.64	-122.11	57.005	1.1	0.092	3.5
2015	8	22	8	14	28.9	-122.295	57.005	2.1	0.86	1.5
2015	8	22	10	55	4.29	-122.105	57.002	1.215	0.556	2.3
2015	8	22	10	55	37.24	-122.21	56.975	1.88	0.264	2.7
2015	8	22	11	22	16.19	-122.215	56.972	0.46	0.1	2.4
2015	8	22	11	24	15.32	-122.245	57.017	0.795	0.3	1.2
2015	8	23	1	50	2.7	-122.3	56.977	0.71	0.104	1.5
2015	8	23	3	41	3.47	-122.245	57.014	0.91	0.356	2.1
2015	8	23	4	2	23.74	-122.25	57.011	0.74	0.24	1
2015	8	23	12	8	39.31	-122.24	57.006	1.44	0.524	4
2015	8	23	12	20	18.97	-122.3	56.975	0.915	0.396	1.5
2015	8	24	6	20	38.38	-122.295	56.972	0.92	0.26	2.6
2015	8	24	6	27	33.36	-122.29	56.968	1.36	0.564	3.7
2015	8	24	16	0	59.18	-122.295	57.005	0.6	0.252	1.3
2015	8	25	10	20	47.72	-122.333	56.97	1.02	0.252	1.4
2015	8	25	10	54	32.57	-122.215	56.967	0.815	0.12	1.3
2015	8	25	11	29	33.9	-122.21	56.972	0.76	0.192	3.5
2015	8	26	4	59	54.43	-122.208	56.97	1.06	0.268	2.4
2015	8	26	18	15	5.02	-122.22	56.997	0.875	0.22	1.1
2015	8	26	18	37	3.46	-122.22	56.995	1.215	0.188	1.4
2015	8	27	14	57	51.87	-122.215	57	0.87	0.3	2.8
2015	8	27	14	57	52.25	-122.235	56.997	1.42	0.188	3.4
2015	8	29	2	34	33	-122.21	57.006	0.46	0.12	2.7
2015	8	30	9	59	30.74	-122.26	56.982	0.55	0.136	1

2015	8	31	16	51	17.26	-122.26	56.975	0.995	0.216	1.9
2015	8	31	23	16	35.42	-122.265	56.962	0.93	0.16	2.8
2015	9	1	10	28	40.34	-122.17	56.98	0.505	0.108	2.5
2015	9	2	2	10	54.71	-122.24	56.978	0.865	0.116	2.6
2015	9	2	4	49	21.78	-122.235	56.975	0.84	0.164	2.2
2015	9	2	7	18	53.03	-122.235	56.973	1.215	0.172	1.7
2015	9	2	7	27	31.73	-122.234	56.968	0.63	0.16	2.6
2015	9	2	7	28	11.11	-122.228	56.966	0.655	0.292	2
2015	9	2	7	29	15.62	-122.228	56.967	0.63	0.092	3.3
2015	9	2	7	30	29.25	-122.232	56.967	1.14	0.176	1.1
2015	9	2	7	31	26.04	-122.225	56.968	1.325	0.232	3.3
2015	9	2	7	31	53.41	-122.23	56.965	0.835	0.276	3.5
2015	9	2	7	33	29.89	-122.233	56.963	2.925	0.28	3.8
2015	9	2	7	33	42.65	-122.235	56.964	0.74	0.08	1.5
2015	9	2	7	42	34.98	-122.232	56.96	1.9	0.212	3.2
2015	9	2	7	46	25.39	-122.2	56.967	0.98	0.252	1.3
2015	9	2	7	55	52.8	-122.207	56.964	1.42	0.236	3.2
2015	9	2	8	24	58.38	-122.21	56.96	1.25	0.164	1.4
2015	9	2	8	42	49.88	-122.195	56.956	1.595	0.332	3.6
2015	9	2	8	50	47.38	-122.22	56.953	0.515	0.108	1.9
2015	9	2	9	5	9.74	-122.215	56.95	0.525	0.216	1.6
2015	9	2	9	23	57.24	-122.195	56.948	1.095	0.132	1.4
2015	9	2	10	15	25.66	-122.2	56.945	1.085	0.284	2
2015	9	2	10	19	28.3	-122.197	56.944	0.855	0.14	1.9
2015	9	2	12	3	38.32	-122.197	56.942	1.21	0.14	1.3
2015	9	2	13	1	4.44	-122.205	56.94	1.205	0.156	3.5
2015	9	2	13	13	36.52	-122.18	56.938	1.81	0.52	3
2015	9	2	18	21	8.96	-122.185	56.936	0.815	0.104	3
2015	9	2	18	40	7.4	-122.187	56.962	1.025	0.22	2.6
2015	9	2	18	44	57.12	-122.172	56.957	0.515	0.104	2.2
2015	9	2	23	18	19.64	-122.18	56.97	0.91	0.164	2.3
2015	9	2	23	32	59.32	-122.175	56.968	1.51	0.308	2.1

2015	9	3	5	30	5.72	-122.225	56.945	1.235	0.324	3
2015	9	3	5	48	42.48	-122.228	56.95	2.045	0.252	2.9
2015	9	3	5	48	43.34	-122.21	56.943	0.955	1.188	4.5
2015	9	3	7	27	58.89	-122.235	56.954	2.68	1.54	1.8
2015	9	3	10	3	8.07	-122.24	56.953	0.805	0.516	2.8
2015	9	3	14	29	38.64	-122.235	56.94	1.045	0.188	3.3
2015	9	3	15	23	47.18	-122.24	56.938	1.21	1.212	2
2015	9	3	15	59	49.15	-122.242	56.936	0.66	0.268	3.9
2015	9	3	15	59	49.89	-122.233	56.953	0.63	0.248	3.9
2015	9	4	4	4	40.05	-122.18	56.98	0.725	0.268	2.4
2015	9	4	11	34	3.07	-122.182	56.982	0.43	0.192	1.9
2015	9	5	10	44	37.64	-122.182	56.986	0.9	0.228	4.3
2015	9	5	14	19	58.22	-122.163	56.982	1.845	0.28	2.5
2015	9	5	16	15	48.76	-122.182	56.986	0.915	0.376	3.9
2015	9	6	12	17	17.85	-122.165	56.95	2.935	0.904	1.8
2015	9	6	13	24	51.14	-122.16	56.947	1.435	0.232	4.4
2015	9	6	14	16	17.91	-122.155	56.942	1.095	0.38	2.2
2015	9	6	21	55	56.78	-122.158	56.954	0.915	0.1	3.2
2015	9	7	6	28	40.38	-122.165	56.987	1.195	0.316	2.3
2015	9	7	10	20	15.42	-122.135	56.984	0.695	0.248	1.5
2015	9	7	11	0	27.94	-122.158	56.986	0.69	0.332	1.3
2015	9	7	11	7	32.52	-122.13	56.957	1.545	0.108	3.7
2015	9	8	1	40	23.36	-122.15	56.944	2.45	0.596	2
2015	9	8	8	8	33.65	-122.16	56.941	2.01	0.388	1.5
2015	9	9	0	49	23.5	-122.097	56.997	0.51	0.16	3.2
2015	9	9	5	2	49.48	-122.115	57.001	1.44	0.928	1.7
2015	9	9	5	11	46.13	-122.11	57.006	0.88	0.676	3
2015	9	9	6	24	17.77	-122.105	57.002	0.84	0.105	3.2
2015	9	9	6	48	13.57	-122.185	56.954	1.29	0.22	2.9
2015	9	9	6	48	14.24	-122.1	57.001	0.58	0.205	2.1
2015	9	9	8	21	19.6	-122.19	56.957	1.73	0.285	4
2015	9	9	8	45	31.01	-122.18	56.951	0.795	0.265	1.6

2015	9	9	11	15	58.85	-122.173	56.951	1.4	0.125	3.5
2015	9	10	0	46	15.33	-122.125	56.974	0.63	0.325	1.2
2015	9	10	10	42	32.3	-122.123	56.969	1.7	0.395	2.6
2015	9	10	10	50	21.9	-122.117	56.967	2.265	0.41	3.9
2015	9	11	3	37	17.84	-122.113	56.966	0.48	0.185	2.3
2015	9	12	4	15	57.42	-122.27	56.916	2.105	0.305	3.1
2015	9	12	14	1	3.55	-122.275	56.917	0.705	0.21	1.7
2015	9	12	20	50	34.6	-122.268	56.911	0.905	0.32	1.6
2015	9	13	13	52	5.07	-122.25	56.911	1.81	0.16	3.7
2015	9	15	6	12	48.17	-122.295	56.917	1.55	0.11	2.7
2015	9	15	10	35	58.61	-122.292	56.916	1.575	0.96	2.9
2015	9	15	18	27	27.88	-122.288	56.92	1.065	0.41	1.4
2015	9	17	5	21	42.56	-122.31	56.912	1.02	0.215	1.8
2015	9	17	11	18	50.95	-122.29	56.922	0.73	0.205	3
2015	9	19	7	32	19.18	-122.285	56.924	0.71	0.265	1.9
2015	9	20	7	20	21.88	-122.285	56.917	1.81	0.32	2.7
2015	9	21	6	19	3.45	-122.282	56.915	2.845	0.715	2.6
2015	9	21	6	20	10.41	-122.275	56.916	1.1	0.32	2.1
2015	9	21	12	39	32.07	-122.265	56.912	2.725	0.455	3.5
2015	9	21	15	48	3.34	-122.283	56.917	0.885	0.8	3.1
2015	9	23	22	29	14.6	-122.285	56.911	1.625	0.23	2.8
2015	9	23	23	45	11.74	-122.275	56.907	0.515	0.305	3.6
2015	9	24	7	4	28.63	-122.26	56.905	0.525	0.12	3.3
2015	9	25	0	52	51.7	-122.135	56.91	1.515	0.25	2.9
2015	9	25	0	54	52.11	-122.138	56.907	0.41	0.195	2.5
2015	9	25	11	45	5.21	-122.14	56.915	2.075	0.305	1.2
2015	9	25	14	30	9.85	-122.135	56.927	1.715	0.33	2.2
2015	9	26	2	45	22.94	-122.13	56.925	0.55	0.155	2.5
2015	9	26	3	28	47.67	-122.128	56.922	0.945	0.115	2.2
2015	9	26	4	20	46.38	-122.115	56.907	2.47	1.075	1.9
2015	9	26	5	19	29.43	-122.131	56.924	1	0.695	1.4
2015	9	26	5	40	57.78	-122.11	56.927	1.07	0.33	1.2

2015	9	26	8	6	50.88	-122.115	56.922	0.455	0.125	2.5
2015	9	26	8	55	0.17	-122.15	56.912	1.185	0.375	1.6
2015	9	26	9	55	19.9	-122.147	56.911	0.675	0.13	2.7
2015	9	26	9	56	44.02	-122.142	56.906	1	0.445	1.7
2015	9	26	10	39	2.76	-122.138	56.902	0.75	0.3	3
2015	9	27	14	4	30.78	-122.127	56.92	1.36	0.655	3.7
2015	9	27	15	26	7.29	-122.107	56.923	0.865	0.495	3.1
2015	9	27	16	32	38.55	-122.115	56.92	0.73	0.325	2.3
2015	9	28	5	43	16.07	-122.127	56.92	1.78	0.705	2.1
2015	9	28	11	44	45.04	-122.126	56.915	0.885	0.315	1.6
2015	9	28	12	9	4.65	-122.113	56.917	1.165	0.315	2.1
2015	9	28	12	22	55.17	-122.11	56.932	0.685	0.15	2.6
2015	9	28	12	47	12	-122.118	56.91	0.77	0.24	1
2015	9	28	17	20	52.68	-122.135	56.9	1.155	0.335	2
2015	9	29	7	51	38.99	-122.13	56.898	0.655	0.275	1.2
2015	9	29	14	15	31.11	-122.127	56.895	1.055	0.235	1.9
2015	9	29	14	28	12.93	-122.102	56.917	0.515	0.375	1.1
2015	9	29	16	50	38.08	-122.123	56.892	0.455	0.235	2.8
2015	9	30	3	22	24.63	-122.14	56.932	0.48	0.15	2.4
2015	9	30	5	21	28.02	-122.12	56.907	0.445	0.17	2.6
2015	9	30	5	40	55.49	-122.103	56.912	0.71	0.27	1
2015	9	30	8	30	21.62	-122.107	56.905	0.86	0.2	2.6
2015	9	30	9	10	57.33	-122.105	56.902	0.49	0.135	1.6
2015	9	30	9	28	4.18	-122.1	56.902	0.69	0.145	1.4
2015	9	30	10	59	31.67	-122.097	56.898	0.675	0.205	2.7
2015	10	1	2	6	59.27	-122.157	56.917	1.14	0.215	2.5
2015	10	1	2	54	22.7	-122.153	56.917	0.585	0.2	1.9
2015	10	1	5	27	30.11	-122.14	56.9	0.77	0.365	1.5
2015	10	1	6	4	12.12	-122.12	56.894	0.765	0.115	1.6
2015	10	1	19	23	4.45	-122.123	56.892	1.265	0.22	2.5
2015	10	2	9	51	31.02	-122.125	56.888	0.75	0.29	1.4
2015	10	2	11	29	33.26	-122.12	56.888	0.915	0.345	2.7

2015	10	3	2	22	57.55	-122.115	56.883	0.72	0.35	2.6
2015	10	3	11	55	51.38	-122.15	56.9	0.64	0.1	1.6
2015	10	4	0	50	53.22	-122.123	56.892	1.065	0.265	2.1
2015	10	7	13	24	10.5	-122.145	56.908	1.08	0.315	2.9
2015	10	8	15	3	51.39	-122.12	56.883	1.405	0.045	3

Tab.A2 The corner frequency and error values between each master event and respective multiple eGFs, calculated from the stacked spectral ratio method. S and P in the second columns denote the corner frequency for the P-wave and S-wave, respectively.

Master event	eGF	Corner frequency
M_w 4.6 Master event	6555.82(S)	3.2±0.2
	4951.15(S)	3.4±0.7
	47586.40(S)	4.3±0.4
	47586.40(P)	2.45±0.6
	41020.00(S)	3.8±0.2
	40540.23(P)	3.2±0.9
	31830.00(S)	2.1±0.8
	31830.00(P)	4±1.9
	31501.22(S)	3.9±0.2
	27110.00(S)	3.2±0.8
	26330.00(S)	3.9±1
	23300.30(S)	3.4±1.5
	23099.87(S)	3.8±0.6
	23053.31(S)	3.1±0.8
	17327.88(S)	3.4±0.1
	14650.70(S)	2.9±0.2
M_w 3.3 Master event	79453.11(P)	7.8±2
	75584.00(P)	8.8+3.2
	67009.74(S)	6.2±2.4

	58540.71(S)	8.2±1.9
	4952.15(S)	7.1±3.8
	47586.00(P)	6.8±1.8
	46522.70(S)	8±1.5
	26801.10(S)	5.3±3.3
	26801.10(P)	5.8±2.9
M_w 3.1 Master event	23099.87(S)	10±3.7
	19549.42(S)	7±3.2
	17327.82(S)	8.9±2
	14650.70(S)	6.2±1.9
	14650.75(P)	6.3±2
	13384.09(S)	6±1.8
	58540.71(P)	7.5±1.2
M_w 2.8 master event	75584.48(S)	11±4
	13384.09(S)	10.1±3.2
M_w 2.5 master event	46522.70(S)	12.3±2.2
	13384.09(S)	14.1±1.9
M_w 2.3 master event	9268.34(S)	9.2±4.4
M_w 2.1 master event	13384.09(S)	13.8±4.3
M_w 2.0 master event	40540.23(S)	15.8±3.9
M_w 1.9 master event	32897.02(S)	11±2.3
	19549.42(S)	11.4±3.9
M_w 1.9 master event	502.68(S)	16.8±6

Text.A1 GPS time correction. Following the study Yu et al. (2019), we apply an ambient noise time correction to the four stations that were partially unlocked during the deployment period. The ambient noise approach is widely used to correct timing errors (e.g., Sens-Schönfelder, 2008; Hannemann et al., 2013), and reduced the clock error by an order of magnitude.

To calculate the time correction, we first compute the normalized daily cross correlation functions (CCFs) of continuous waveforms between two stations, and subsequently calculate the daily time drift by comparing the daily CCF to the stacked CCF for the same period. Here we use NBC5 as the reference station and compare its daily CCF to the four stations with timing error. We calculate the daily CCFs following the study of Bensen et al. (2017). We modified the open-source MATLAB package developed by Yao et al. (2011) to fit our data. Before calculating the CCFs, we apply a 1-5s band pass filter to the continuous waveforms to avoid the interference between the causal and acausal part of the CCFs (Lin et al., 2017). After the calibration process, the absolute time uncertainty decreases from ~1s to 0.1s

Text.A2 Combination of Grid search and iterative method to determine initial earthquake locations. The grid search method determines earthquake hypocentral locations and origin time by performing a search over all possible spatial and temporal points, and calculates the arrival time at each station. The method chooses the location based on the closest match to the observations (e.g., Sambridge and Kennett, 2001; Sambridge and Kennett, 1986 and 2001). Here, we use Eq. A1 below to find the minimum residual (RMS) between the observed and calculated travel times:

$$RMS = \sqrt{\frac{\sum_{i=1}^{n}(r_o - r_c)^2}{n}} \qquad (A1)$$

Where r_c is the calculated travel time, r_o is the observed travel time, and n is the number of phases from multiple stations used in the calculation. We use both P- and S-phases when calculating the minimum RMS value, and the velocity model plotted in Fig.4.2.

The grid spacing dictates the accuracy of the solution, however, the finer grid spacing, the more computational power is needed. To optimize the tradeoff between computation time and accuracy, we divide the hypocenter calculation into two processing steps. We use a coarse grid spacing of 5 km × 5 km × 5 km in the first step in the region shown in Fig.A.1 to reduce the area over which the finer grid spacing in the second calculation is needed. We then use the nonlinear programing solver function "fmincon" from MATLAB® to search for the point with minimum RMS value through iterative calculations on a 5 km × 5 km × 5 km grid centered on the grid point with the lowest misfit calculated from step one. Combining the grid search and iteration method instead of using only iteration method directly permits us to find a global minimum result and avoid regional minima in the search for a solution.

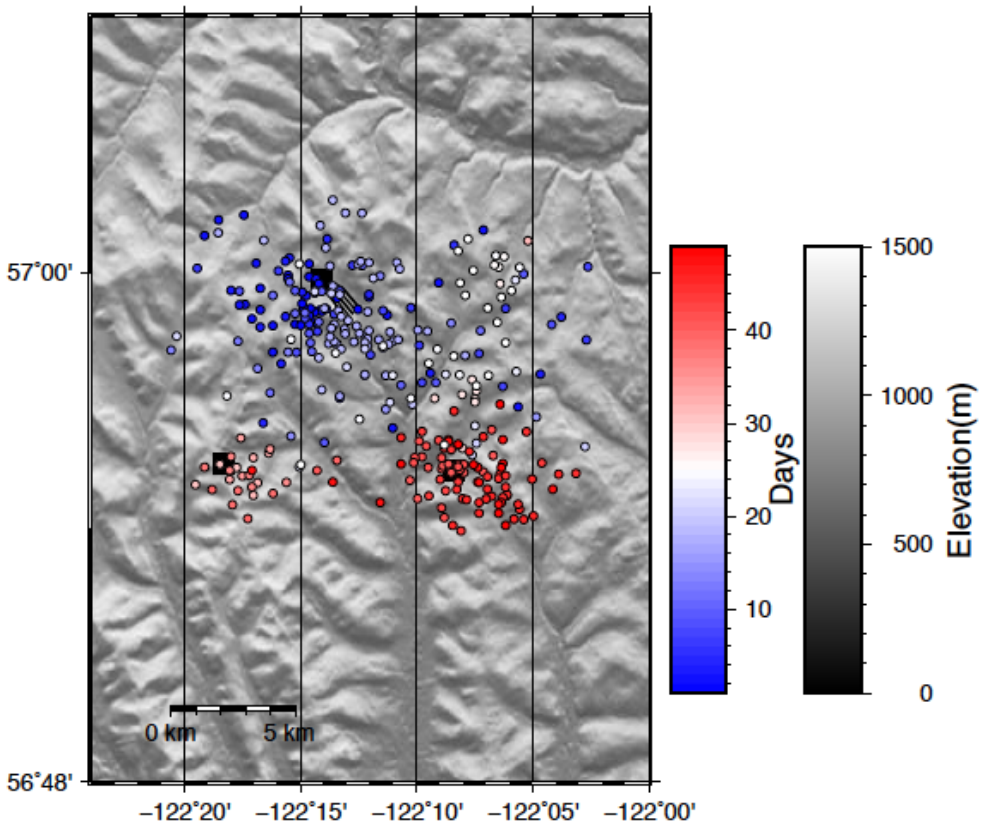

Fig.A.1 Map shows the earthquake initial locations from the two-step grid-search, iterative method. Colors denote the occurrence time since the first earthquake.

Text.A3 M_L, and *b*-value calculation. To calculate the M_L for the relocated events, we follow the approach from van der Elst et al. (2013), using Eq.A2 (e.g., Bullen and Bolt,1985)

$$M_L = log_{10}(A) + 2.56log_{10}(X) - 1.67 \qquad \text{(A2)}$$

where *A* is the peak amplitude within the 4 s after the S wave arrival, *X* is the epicentral distance.

We use the calculated M_L values with the maximum likelihood method to calculate the *b*-value and the enhanced catalog completeness related to W1 (e.g., Aki, 1965). Here, we get a *b*-value of 0.78 and catalog completeness of 1 as shown in Fig.4.8. A *b*-value < 1 could indicate the induced earthquakes happen on pre-existing fault systems (e.g., Skoumal et al. (2015)).

4.8 References for Chapter 4

Abercrombie, R. E. (1995). Earthquake source scaling relationships from 1 to 5 M_L using seismograms recorded at 2.5-km depth. *Journal of Geophysical Research: Solid Earth, 100*(B12), 24015-24036.

Abercrombie, R. E. (2013). Comparison of direct and coda wave stress drop measurements for the Wells, Nevada, earthquake sequence. *Journal of Geophysical Research: Solid Earth, 118*(4), 1458-1470.

Abercrombie, R. E. (2014). Stress drops of repeating earthquakes on the San Andreas fault at Parkfield. *Geophysical Research Letters, 41*(24), 8784-8791.

Abercrombie, R. E. (2015). Investigating uncertainties in empirical Green's function analysis of earthquake source parameters. *Journal of Geophysical Research: Solid Earth, 120*(6), 4263-4277.

Abercrombie, R. E., Poli, P., & Bannister, S. (2017). Earthquake directivity, orientation, and stress drop within the subducting plate at the Hikurangi margin, New Zealand. *Journal of Geophysical Research: Solid Earth,* 122, 10,176– 10,188. Doi: 10.1002/2017JB014935

Abercrombie, R. E., & Rice, J. R. (2005). Can observations of earthquake scaling constrain slip weakening? *Geophysical Journal International, 162*(2), 406-424.

Atkinson, G. M., Eaton, D. W., Ghofrani, H., Walker, D., Cheadle, B., Schultz, R., Shcherbakov, R., Tiampo, K., Gu, J., Harrington, R. M., Liu, Y. J., van der Baan, M., & Kao, H. (2016). Hydraulic Fracturing and Seismicity in the Western Canada Sedimentary Basin.

Seismological Research Letters, 87(3), 631-647. doi: 10.1785/0220150263

Basim, F., Harold, W., & Gary, A. (2004). Gas potential of selected shale formations in the Western Canadian Sedimentary Basin. *Canadian Resources, 10*(1), 21-25.

BC Ministry of Energy, Mines and Petroleum Resources (MEMPR). (2006). Northeast British Columbia's Ultimate Potential for Convertional Naturalk Gas, Retrieved from http://publications.gc.ca/collections/Collection/NE23-134-2006E.pdf, last accessed, 3.13.2019

Brune, J. N. (1970). Tectonic stress and the spectra of seismic shear waves from earthquakes. *Journal of Geophysical Research, 75*(26), 4997-5009.

Brune, J. N. (1971). Correction to tectonic stress and the spectra of seismic shear waves from earthquakes. *Journal of Geophysical Research, 76*(20), 5002-5002.

Clerc, F., Harrington, R. M., Liu, Y., & Gu, Y. J. (2016). Stress drop estimates and hypocenter relocations of induced seismicity near Crooked Lake, Alberta. *Geophysical Research Letters, 43*(13), 6942-6951. doi: 10.1002/2016GL069800

Commission, B. C. O. a. G. (2012). Investigation of observed seismicity in the Horn River basin. Technical Rept.

Edwards, D.E., J.E. Barclay, D.W. Gibson, G.E. Kvill, and E. Halton, E. 1994. Triassic strata of the Western Canada Sedimentary Basin, in Geological Atlas of the Western Canada Sedimentary Basin, G.D. Mossop and I. Shetson (compilers): *Canadian Society of Petroleum Geologists*, p. 257-275.

Efron, B., & Tibshirani, R. (1986). Bootstrap methods for standard errors, confidence intervals, and other measures of statistical accuracy. *Statistical science*, 54-75.

Gisela, V., E., A. R., & Won-Young, K. (2010). The 2002 M 5 Au Sable Forks, NY, earthquake sequence: Source scaling relationships and energy budget. *Journal of Geophysical Research: Solid Earth, 115*(B7). doi: 10.1029/2009JB006799

Goebel, T., Weingarten, M., Chen, X., Haffener, J., & Brodsky, E. (2017). The 2016 Mw5. 1 Fairview, Oklahoma earthquakes: Evidence for long-range poroelastic triggering at> 40 km from fluid disposal wells. *Earth and Planetary Science Letters, 472*, 50-61.

Hart, B. S. (2011). *Shale-gas production and sequence stratigraphy: What makes the best part of the best plays.* Paper presented at the Canadian Society of Petroleum Geologists and Canadian Well Logging Society, Conference.

Harrington, R. M., Kwiatek, G., & Moran, S. C. (2015). Self-similar rupture implied by scaling properties of volcanic earthquakes occurring during the 2004-2008 eruption of Mount St.

Helens, Washington. *Journal of Geophysical Research: Solid Earth, 120*(7), 4966-4982.

Huang, Y., Beroza, G. C., & Ellsworth, W. L. (2016). Stress drop estimates of potentially induced earthquakes in the Guy-Greenbrier sequence. *Journal of Geophysical Research: Solid Earth, 121*(9), 6597-6607.

Hough, S. E. (2014), Shaking from injection-induced earthquakes in the central and eastern United States, *Bull. Seismol. Soc. Am*., 104(5), 2619–2626, doi:10.1785/0120140099.

Keilis-Borok, V. (1960). Investigation of the mechanism of earthquakes. *Sov. Res. Geophys., 4*, 29.

Keranen, K., Weingarten, M., Abers, G., Bekins, B., & Ge, S. (2014). Sharp increase in central Oklahoma seismicity since 2008 induced by massive wastewater injection. *Science, 345*(6195), 448-451.

McGarr, A. (2014). Maximum magnitude earthquakes induced by fluid injection. *Journal of Geophysical Research: Solid Earth, 119*(2), 1008-1019.

Moslow, T. F. (2000). Reservoir architecture of a fine-grained turbidite system: Lower Triassic Montney Formation, Western Canada Sedimentary Basin. *Paper presented at the Deep-water Reservoirs of the World, Conference Proceedings,* Gulf Coast SEPM. P. Weimer, RM Slatt, J. Coleman, NC Rosen, H. Nelson, AH Bouma, MJ Styzen, and DT Lawrence (eds.).

Porter, J., Price, R., & McCrossan, R. (1982). The western Canada sedimentary basin. *Philosophical Transactions of the Royal Society of London. Series A, Mathematical and Physical Sciences, 305*(1489), 169-192.

Schultz, R., Atkinson, G., Eaton, D., Gu, Y., & Kao, H. (2018). Hydraulic fracturing volume is associated with induced earthquake productivity in the Duvernay play. *Science, 359*(6373), 304-308.

Skoumal, R. J., Brudzinski, M. R., & Currie, B. S. (2015). Earthquakes Induced by Hydraulic Fracturing in Poland Township, Ohio. *Bulletin of the Seismological Society of America*. 105.1 (2015): 189-197.

Thomson, D. J. (1982). Spectrum estimation and harmonic analysis. *Proceedings of the IEEE, 70*(9), 1055-1096.

van der Elst, N. J., Savage, H. M., Keranen, K. M., & Abers, G. A. (2013). Enhanced remote earthquake triggering at fluid-injection sites in the midwestern United States. *Science, 341*(6142), 164-167. doi: 10.1126/science.1238948

Van der Elst, N. J., Page, M. T., Weiser, D. A., Goebel, T. H., & Hosseini, S. M. (2016). Induced

earthquake magnitudes are as large as (statistically) expected. *Journal of Geophysical Research: Solid Earth, 121*(6), 4575-4590.

Waldhauser, F., & Ellsworth, W. L. (2000). A double-difference earthquake location algorithm: Method and application to the northern Hayward fault, California. *Bulletin of the Seismological Society of America, 90*(6), 1353-1368. doi: 10.1785/0120000006

Wang, B., Harrington, R. M., Liu, Y., Yu, H., Carey, A., & Elst, N. J. (2015). Isolated cases of remote dynamic triggering in Canada detected using cataloged earthquakes combined with a matched-filter approach. *Geophysical Research Letters, 42*(13), 5187-5196.

Wang, B., Harrington, R. M., Liu, Y., Kao, H., & Yu, H. (2018). Remote Dynamic Triggering of Earthquakes in Three Unconventional Canadian Hydrocarbon Regions Based on a Multiple-Station Matched-Filter Approach. *Bulletin of the Seismological Society of America, 109*(1), 372-386.

Weingarten, M., Ge, S., Godt, J. W., Bekins, B. A., & Rubinstein, J. L. (2015). High-rate injection is associated with the increase in US mid-continent seismicity. *Science, 348*(6241), 1336-1340.

Zhang, H., Eaton, D. W., Li, G., Liu, Y., & Harrington, R. M. (2016). Discriminating induced seismicity from natural earthquakes using moment tensors and source spectra. *Journal of Geophysical Research: Solid Earth, 121*(2), 972-993. doi: 10.1002/2015JB012603

Zhuang, J., Ogata, Y., & Vere-Jones, D. (2002). Stochastic declustering of space-time earthquake occurrences. *Journal of the American Statistical Association, 97*(458), 369-380.

Chapter 5

Investigating the roles of Coulomb stress changes caused by fracture opening and poroelastic stress transfer associated with the 17 August 2015 M_w 4.6 earthquake sequence in the Montney Basin, British Columbia, Canada

5.1 Introduction

Anthropogenic activities could induce earthquakes. In the US, wastewater injection through disposal wells is regarded as the main cause of the induced seismicity (e.g., Ellsworth, 2013; Keranen et al., 2014; Weingarten et al., 2015), while hydraulic fracturing (HF) could be the dominant factor for induced earthquakes in Western Canadian Sedimentary Basin (WCSB)(e.g., B.C. Oil and Gas Commission, 2012; Atkinson et al., 2016; Ali et al., 2017; Schultz et al., 2018). Several authors have investigated the potential triggering mechanisms for fluid injection induced earthquakes (e.g., Shapiro et al., 2005; Shapiro and Dinske, 2009; Keranen et al., 2014; Deng et al., 2016; Johann et al., 2018; Yu et al., 2019), and multiple possible mechanisms have been proposed (e.g., fluid-pore pressure migrations, solid matrix stress transfer, and reservoir-like impoundment by injected fluids). However, it is always difficult to establish a robust triggering mechanism for induced earthquakes in different cases due to, e.g., the complex fault geometries, unknown subsurface formations, lack of injection data from industries, and even the incompleteness of the induced earthquake catalog.

The WCSB is well known for the subsurface hydrocarbon resources associated with the thick sedimentary rocks (e.g., Porter et al., 1982), together with hydrocarbon volume to be on the order of 86 trillion cubit feet (e.g., Basim et al., 2004). Among all of the basins in the WCSB, the

Montney Formation is one of the primary focuses of gas reservoirs in the northeastern BC, due to large amount of shale gas and tight gas reserves. The Montney Formation is located at Fort St. John area (FSJ), mainly composed of turbidite siltstone and dark grey shale (Moslow, 2000), comprising less than 20% clays of the rock (Hart, 2011) and deposited on a westward prograding shelf of the pale-continental margin (Edwards et al., 1990). The conventional oil and gas exploration in the northeastern BC focused on thick sandstones of the Montney Formation along the subcrop edge in the FSJ region before the shale gas extraction (MEMPR, 2006). Around year 2011, industry activities are more shifting to unconventional reservoirs to the Montney Formation all around FSJ region (B.C. Oil and Gas Commission, 2012).

Chapter 4 investigates the characteristics of the HF induced seismicity sequences at Montney Basin from May to October, 2015, British Columbia, including earthquake location, distribution pattern, and static stress changes. The detected earthquakes and HF wells are shown in Fig.4.1. However, there are still remaining questions, e.g., what could be the triggering mechanisms for the M_w 4.6 induced earthquake? Why is the seismic response at two HF injection sites nearby (W2 and W3) much faster compared to the 5-day delay at W1 as shown in Fig.4.4? The motivation of this chapter is to address the following issues, 1) investigate the possible triggering mechanism for the M_w 4.6 earthquake, and 2) explore the potential reasons for the different time scales of triggering response at different HF injection sites. In this chapter, we first introduce the approaches used to investigate the M_w 4.6 earthquake in Section 5.2, and then we focus on the fast seismic responses at W2 and W3 in Section 5.3, followed by discussion and conclusion in Sections 5.4 and 5.5.

5.2 Triggering mechanisms for the M_w 4.6 earthquake

We first need to obtain a reliable focal depth and focal mechanism for the M_w 4.6 earthquake, as when we calculate the ΔCFS resolved on the specific receiver fault, the amplitude of the normal and shear stress is directly related to the location and orientation of the fault (e.g., Lin and Stein, 2004).

5.2.1 Focal mechanism solution

Here we use the generalized cut and paste (gCAP) method to synthesize the body and surface waves recorded by broadband seismometers shown in Fig.5.1a (Zhu and Helmeberger, 1996; Zhu and Ben-Zion, 2013), together with a first motion method as a confidence check.

The gCAP method estimates the full moment tensors through a grid search method on the strike, dip, and rake angles of the fault and slip orientation based on P and S-wave inversion simultaneously. Then the moment tensor can be decomposed into three source terms: isotropic (ISO), double-couple (DC) and compensated linear vector dipole (CLVD).

There are three steps to calculate the focal mechanism solution with gCAP, 1) compute Green's functions based on the 1-D local velocity model with the frequency-wavenumber integration approach (Aki and Richards, 2002; Zhu and Riverra, 2002) (The velocity model is shown in Fig.5.2, from Kao et al., 2012, we prefer this velocity model to calculate the focal mechanism instead of the one used in Chapter 4, as it gives us higher variance reduction from gCAP result and shows better consistency with the polarity check). 2) Filter the original seismograms; here we use the frequency bands 0.05-0.3 Hz and 0.02-0.1 Hz for P and S waves, respectively, and cut the three component records into five phase windows, including the radial and vertical components of P wave and all three S wave components (e.g. Yu et al 2016). 3) Calculate the misfit between the synthesized waveform with the filtered waveform to find the

best-fit result. The deviation between the earthquake location and the true values can also be adjusted by time shifting from gCAP, hence relying much less on the accuracy of the earthquake location result.

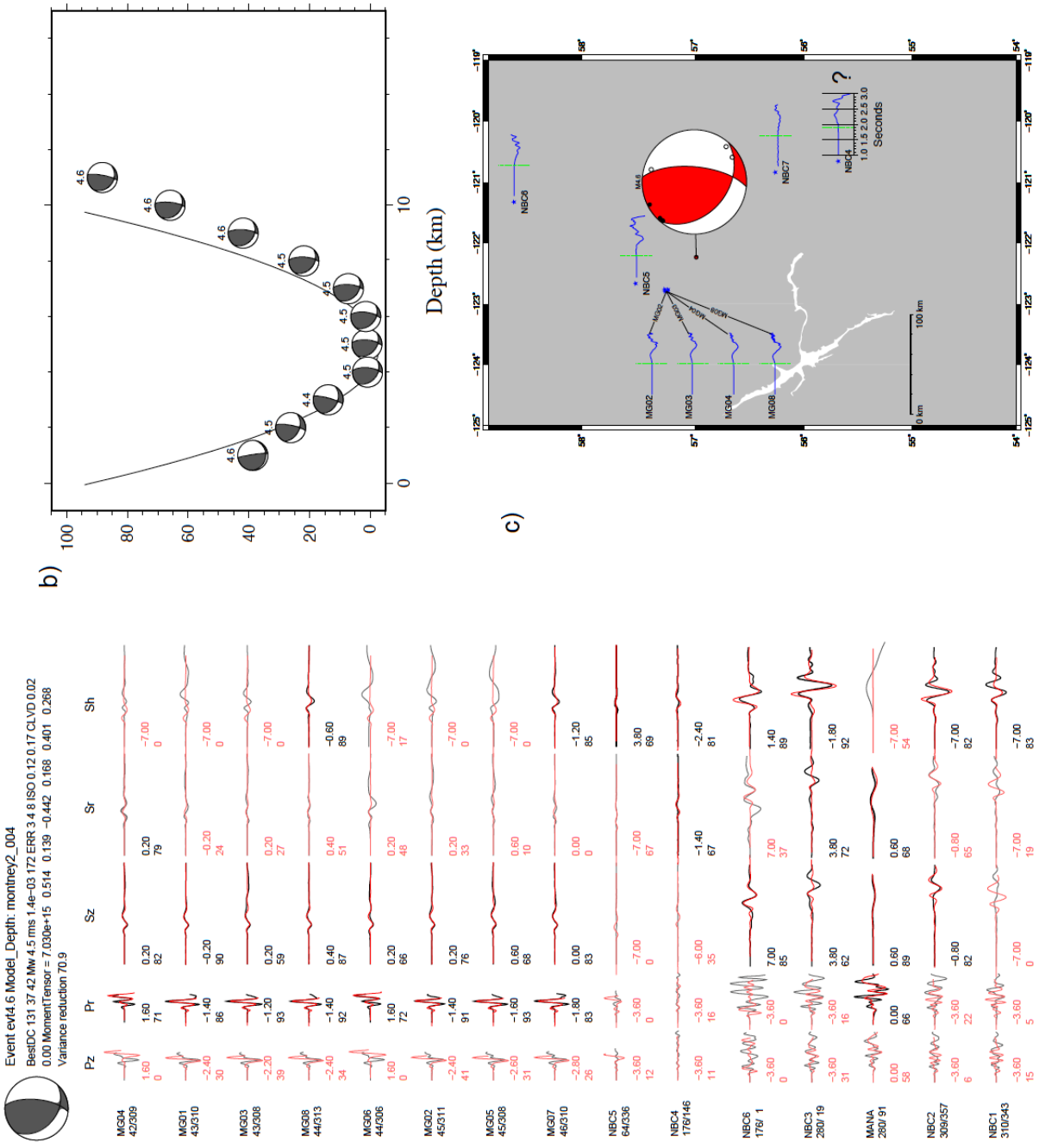

Fig.5.1 Focal mechanism solutions for the M_w 4.6 earthquake. a) synthetic and observed seismograms match at each station, which are plotted as dashed and solid lines, respectively. The lines with black numbers below show the used match in the inversion and lines with red numbers below are the discarded pairs. b) Misfit error of moment tensor inversion versus depth by gCAP method. c) The confidence check by the P-wave first motion method, where the black circles indicate stations with positive polarity (upward) and white circles indicate negative polarity (downward). The question mark at station NBC4 denotes that there is uncertainty for the polarity.

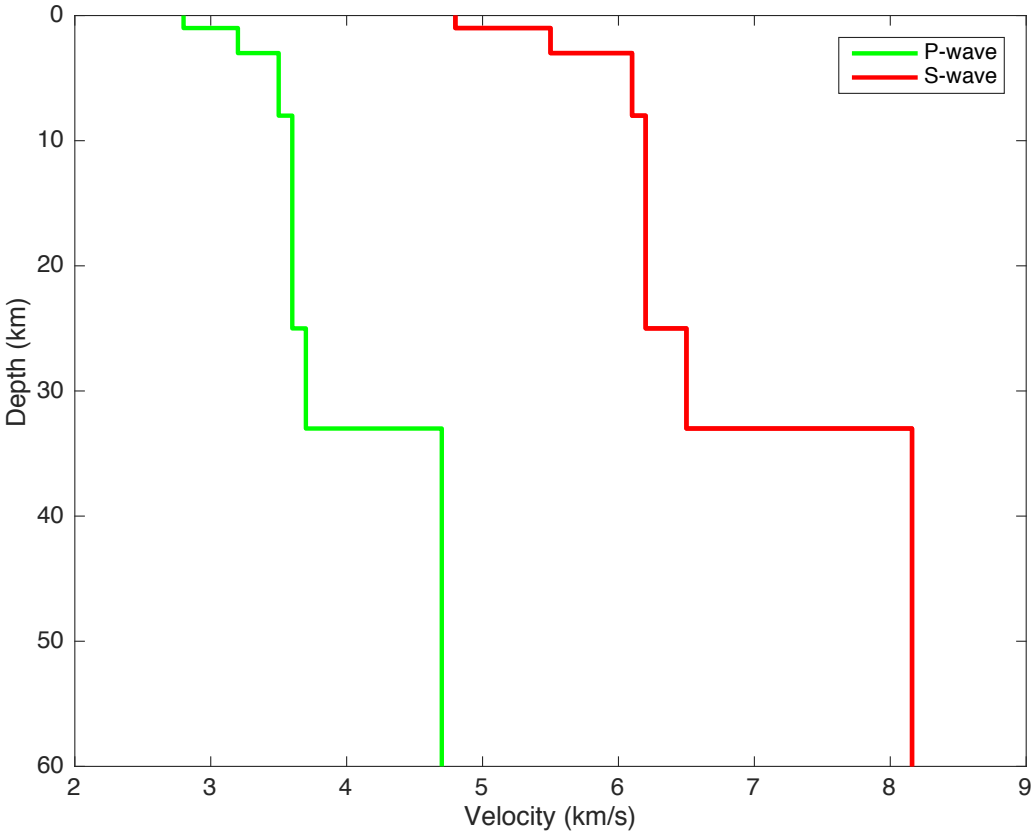

Fig.5.2 Velocity model used in the focal mechanism calculation from Kao et al. (2012).

We set the depth range for the grid search from 1-10 km, and we choose the 4 km depth as the best solution with the lowest overall misfit as shown in Fig.5.1b. The result corresponds to a thrust mechanism, and northwest-southeast nodal plane, which is also consistent with the earthquake distribution as shown in Fig.4.1b. As a confidence check, we use the first motion

method to test the reliability of the gCAP results, which is shown in Fig5.1c. Except for NBC4, for which the first motion polarity is difficult to obtain, all other stations exhibit consistent polarities with the gCAP focal mechanism solution.

5.2.2 Coulomb stress change caused by fracture opening

After we obtain the focal mechanism and depth, we use the Coulomb stress approach to study the relationship between fluid injections and earthquakes distribution. The change of Coulomb failure stress can be defined as follows

$$\Delta CFS = \Delta\tau + \mu(\Delta\sigma + \Delta p) \qquad (5.1)$$

where $\Delta\tau$ is the shear stress change and $\Delta\sigma$ is the normal stress change resolved onto a fault plane, μ is the friction coefficient and Δp is the pore pressure change. Positive ΔCFS will favor failure while, while negative ΔCFS will discourage failure (e.g., Harris, 1998; Stein, 1999).

To investigate the ΔCFS caused by fracture openings from HF operations, we first need to estimate the dimension of the fractures caused by fluid injection. It is important to note that the fracture opening by assumptions may not properly represent the realistic case, as the stress field around a fluid pressurized propagating mode-1 crack is different from static stress from a finite opening (without fluid). Fig.5.3 gives a schematic plot of the HF induced fracture openings from Fairhurst (2013). The shale layer's formation starts around 1.7 km depth and extends to 2.1 km depth (around 400 m thick). Due to the lack of information on the fractures, we assume a vertical 500 m × 30 m tensile fracture in length and depth, respectively, similar to the study by Bao and Eaton (2016), and that the opened fracture is parallel with the maximum horizontal stress (here, we assume 60° as S_{Hmax}, from Bell and Grasby, 2012), aligned along the horizontal well. Then we assume the width of each fracture to be 25 mm (e.g., Boroumand and Eaton, 2015; Bao and

Eaton, 2016), and we adjust the number of fractures and the size of the last fracture based on the total amount of fluids injected at each stage, so that the total volume between the fracture openings and fluids are equal. Then we use Coulomb 3.4 (Lin and Stein, 2004; Toda et al., 2005) to calculate the ΔCFS resolved onto the fault with the focal mechanism solution we obtained from Section 5.1, with friction coefficient of 0.6. We also calculate the ΔCFS at the depth range from 3 km and 5 km for the receiver fault with same focal mechanisms, due to the possible location error. The result of ΔCFS change from fracture openings is shown in Fig.5.4.

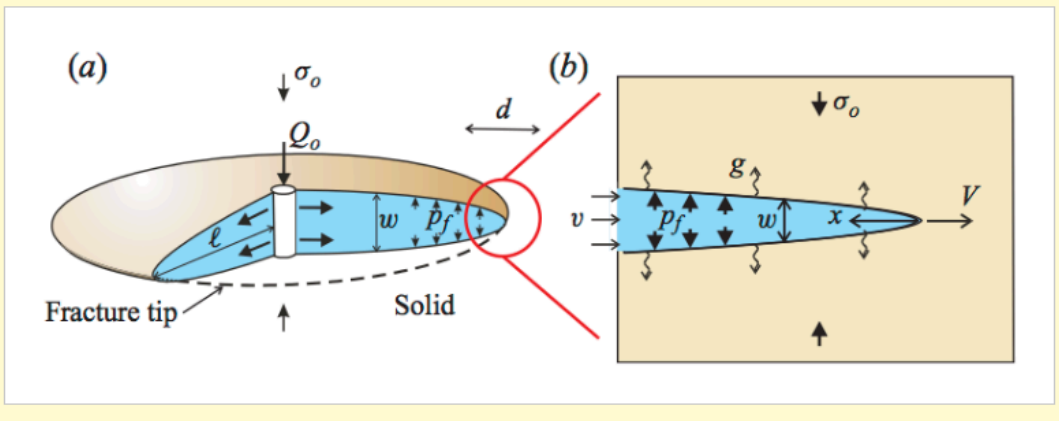

Fig.5.3 Radial model of symmetric flow and deformation associated with HF (from Fairhurst, 2013)

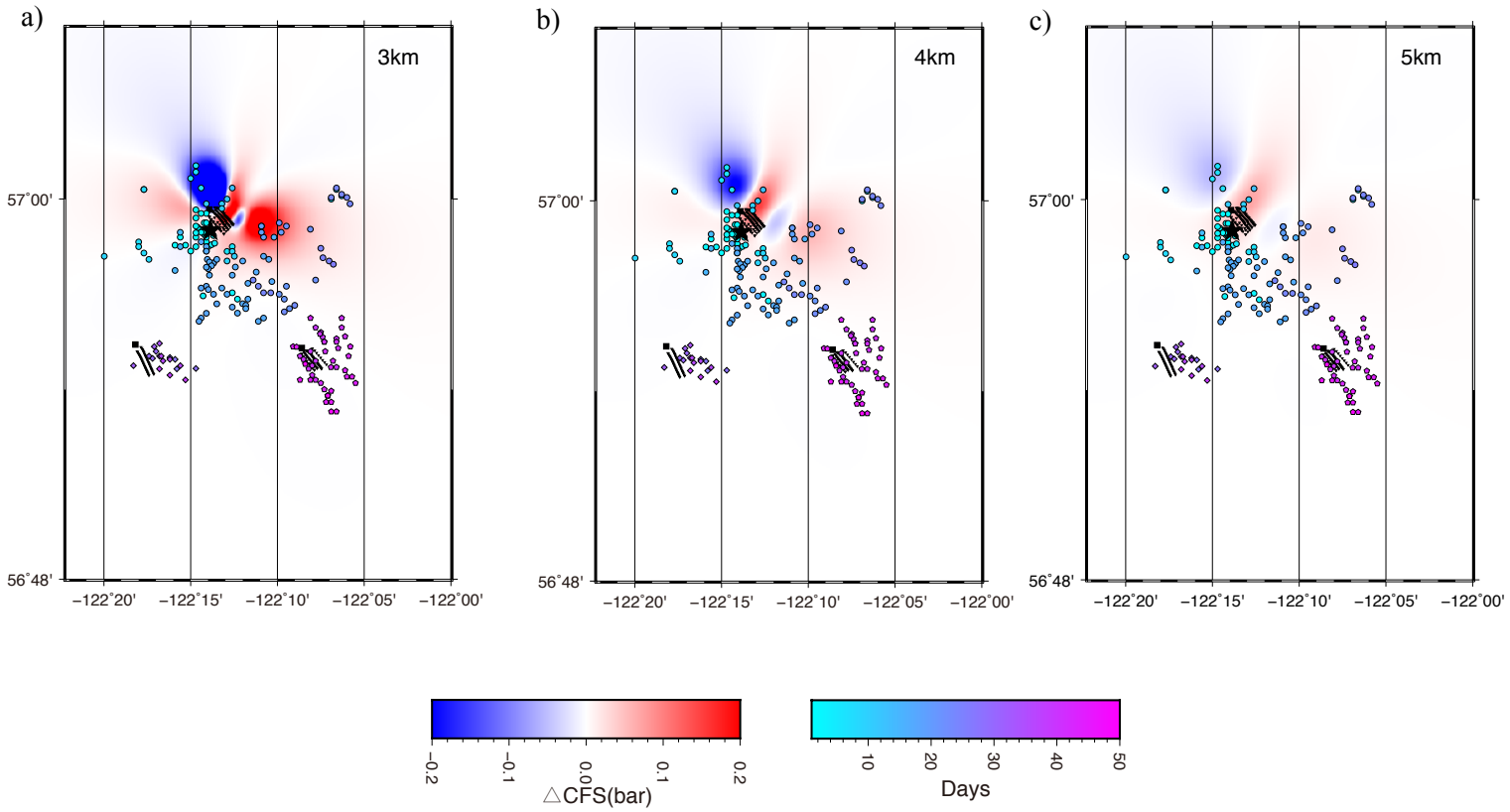

Fig.5.4 ΔCFS calculated with a depth range between 3 km and 5 km, caused by the elastic stress perturbations from the tensile fracture openings before the M_w 4.6 mainshock. The receiver fault kinematics are strike 131°, dip 37°, and rake 42°. The black star shows the location of the M_w 4.6 earthquake, the filled circles, diamonds and pentagons denote the relocated earthquakes related to W1, W2 and W3 respectively, and the color corresponds to the occurrence time (Fig.4.1). The small triangles denote different stages of HF operations.

5.2.3 Poroelastic models based on fluid injection

Analytic and numerical models have been widely used to study induced seismicity (e.g., Segall and Lu, 2015; Deng et al., 2016; Bao and Eaton, 2016; Goebel et al., 2017; Yu et al., 2019). Both the pore-fluid pressure diffusion and poroelastic stress perturbation could be the potential driving force. To investigate the potential triggering mechanisms in this M_w 4.6 earthquake case, here, we use the COMSOL Multiphysics® software 5.3a, which is based on a finite element algorithm, to model the pore-fluid pressure diffusion and poroelastic stress from

fluid-solid coupling simultaneously. We use the solid mechanism module and Darcy's fluid flow module to simulate the poroelastic coupling process.

If we assume an isotropic and homogeneous medium, then the pore-fluid pressure can be obtained by the solution of the coupled diffusion equation (similar equivalent forms of the equations can be found, e.g., Wang and Kumpel, 2003; Shapiro and Dinske,2009),

$$\rho S \frac{\partial p}{\partial t} - \nabla \cdot \left(\rho \frac{\kappa}{\mu} \nabla p\right) = Q_m(x,t) - \rho\alpha \frac{\partial \varepsilon_{vol}}{\partial t} \tag{5.2}$$

$$S = \chi_f \epsilon + \chi_p (1-\epsilon) \tag{5.3}$$

$$q = -\frac{\kappa}{\mu} \nabla p \tag{5.4}$$

where S is the linearized storage parameter, p is the fluid's pressure in the pore space, ε_{vol} is the volumetric strain of the porous matrix, κ is the permeability of the block, Q_m is the volumetric flow rate for a fluid source, α is the Biot-Willis coefficient, ρ is the fluid's density and μ is its dynamic viscosity, χ_f is the compressibility of the fluid, χ_p is the compressibility of the rock and q is the velocity variable which gives a volume flow rate per unit area of porous material. COMSOL uses S as the default parameter in Equation 5.2, while some studies use the Biot modulus M^{-1} instead of S, which can be calculated from the Young's modulus and Poisson's ratio (e.g., Rice and Cleary, 1976; Detournay and Cheng, 1993; Leake and Hsieh, 1997). Then with the governing equations for the poroelastic model:

$$-\nabla \cdot \sigma = F_v \tag{5.5}$$

$$\sigma_{ij} = \frac{2G\nu}{(1-2\nu)} \varepsilon \delta_{ij} + 2G\varepsilon_{ij} - \alpha p \delta_{ij} \tag{5.6}$$

$$\varepsilon = \frac{1}{2}((\nabla \boldsymbol{u})^T + \nabla \boldsymbol{u}) \tag{5.7}$$

where σ is the stress tensor, F_v is the volume force vector, and when gravity is the only driving force, $F_v = (\rho\theta + \rho_b)g$, where g is the acceleration of gravity, ρ is the fluid density, θ is the porosity, ρ_b is the bulk density, G is the shear modulus, and ν is the Poisson's ratio. The changes of stress tensor σ, porous matrix displacement $\boldsymbol{u}$ and pore pressure p based on the boundary conditions can be determined using the three equations above. Equation 5.5 defines static equilibrium, as the changes in the solid equilibrate much faster than the fluid flow, with no time dependent terms. Thus the time rate of strain change $\frac{\partial \varepsilon_{vol}}{\partial t}$ displays a coupling term in Darcy's Law as the solid equation becomes quasi-static if the time-dependent flow is solved simultaneously.

We build our approximate 3D model with 5 km × 5 km dimension in the x and y direction, with 5 km in depth. The geometries for the 3D model are the same as the Coulomb model of the fracture openings. We transform the well and fault locations from latitude and longitude into UTM system. Then we divide the model into four layers as shown in Fig.5.5, which includes the upper sedimentary layer, the shale layer where the HF occurs, the lower sedimentary layer, and crystalline basement. We use published data for solid and hydraulic mechanical properties of each layer in our model (e.g., Clauser, 1992; Neuzil, 1994; Rokosh et al., 2008; Rokosh et al., 2010; Laske et al., 2013; Dong et al., 2017; Vishkai et al., 2017; Cui and Nassichuk, 2018), and major properties used in the model are listed in Tab.5.1. The shale layer with HF operations has the lowest permeability compared to the confining layers, and we assume the fluid properties do not change versus depth or time. With the corner frequency estimated for the M_w 4.6 earthquake from Chapter 4, we assume a circular rupture with radius 400 m based on the study of Madariaga

(1977), with strike 131°, dip 37°, and rake 42°, and we assume a 1.5 km × 1.5 km fault patch in order to include this whole circular rupture.

	Layer 1	Layer 2	Layer 3	Layer 4
Depth	0-1.7 km	1.7 km-2.1 km	2.1 km-3 km	3 km-5 km
Biot-William	1	1	1	1
P-wave velocity	3600 m/s	4400 m/s	6300 m/s	7100 m/s
S-wave velocity	2080 m/s	2540 m/s	3630 m/s	3990 m/s
Density	2160 kg/m^3	2460 kg/m^3	2740 kg/m^3	3000 kg/m^3
Permeability	7.5×10^{-14} m^2	0.1×10^{-16} m^2	0.5×10^{-16} m^2	0.5×10^{-15} m^2
Porosity	0.1	0.05	0.05	0.08
Fluid density	1000 kg/m^3	1000 kg/m^3	1000 kg/m^3	1000 kg/m^3
Fluid compressibility	4.5×10^{-10} Pa^{-1}	4.5×10^{-10} Pa^{-1}	4.5×10^{-10} Pa^{-1}	4.5×10^{-10} Pa^{-1}
Fluid dynamic viscosity	0.79×10^{-3} Pa*s	0.79×10^{-3} Pa*s	0.79×10^{-3} Pa*s	0.79×10^{-3} Pa*s

Tab.5.1 Solid and fluid properties of each layer used in model one, two and three for the M_w 4.6 simulation shown in Fig.5.5, and for the two models for W2 and W3 shown in Fig.5.9. For the fracture zone in model two and three, the solid properties are the same as for Layer 2, and the permeability is 0.5×10^{-14} m^2. For the high permeability conduit, the solid properties at different depth are the same to the corresponding layer, and the permeability is 0.5×10^{-12} m^2. For the fault, its solid properties are the same for Layer 4, the permeability along the fault is 0.5×10^{-15} m^2, and the permeability perpendicular to the fault is 0.1×10^{-16} m^2.

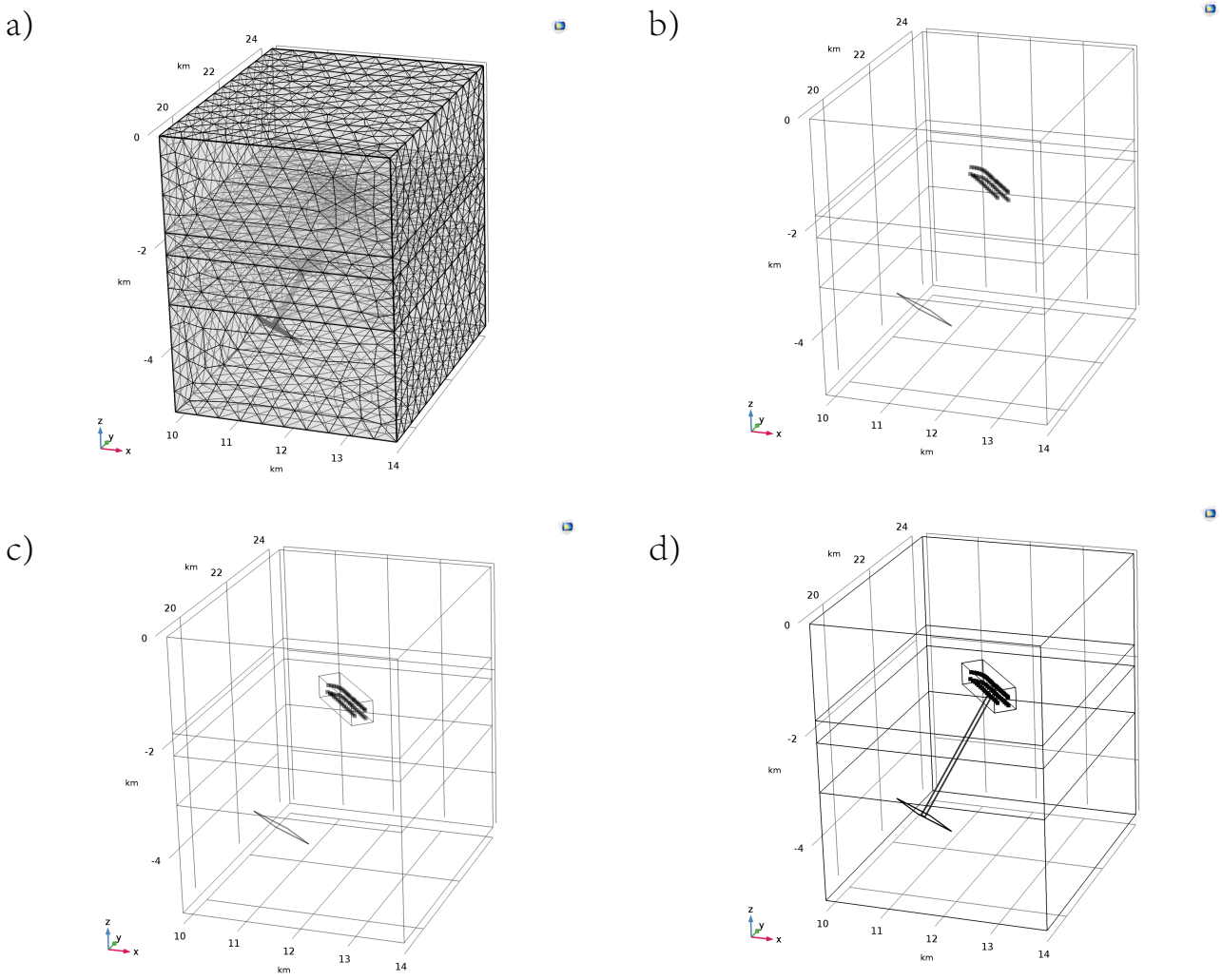

Fig.5.5 The four layer models built with COMSOL to simulate the triggering mechanisms of the M_w 4.6 earthquake, the square denotes the fault patch (fourth layer), the dashed points represent the injection points, the cube located at the second layer (shale) represents the fracture zone caused by HF operation and the vertical cylinder denotes the higher permeability conduit. a) shows the model's meshing grids, b), c) and d) denote Model 1, Model 2, and Model 3 respectively. The characteristics for each model can be found in the text.

Then we set the fluid-solid boundary and initial conditions in the numerical model. For the side and bottom solid boundaries, we use a so-called roller condition boundary, which implies no vertical movement for the solid material to the boundary. The fluid boundaries are set to no flow. At the top boundary we added a standard atmosphere pressure, and the pore pressure is set to 0

Pa. For the initial conditions, we include the gravity as the driven stress, and we assume a hydro-static conditions for all four layers. For this, we use a stationary model as our first study. Here we set the initial displacement u and initial pressure p to be 0, and only solve the stress field and pressure as a result of the gravity loading; the hydro-static result is shown in Fig.5.6 (Note that in the model, there are no time-depend variables). Then we add another time-dependent model with the poroelasticity multiphysics module, which uses the stress and pressure solutions from the stationary model as the initial condition, this two-step models can also help COMSOL stabilize the solutions.

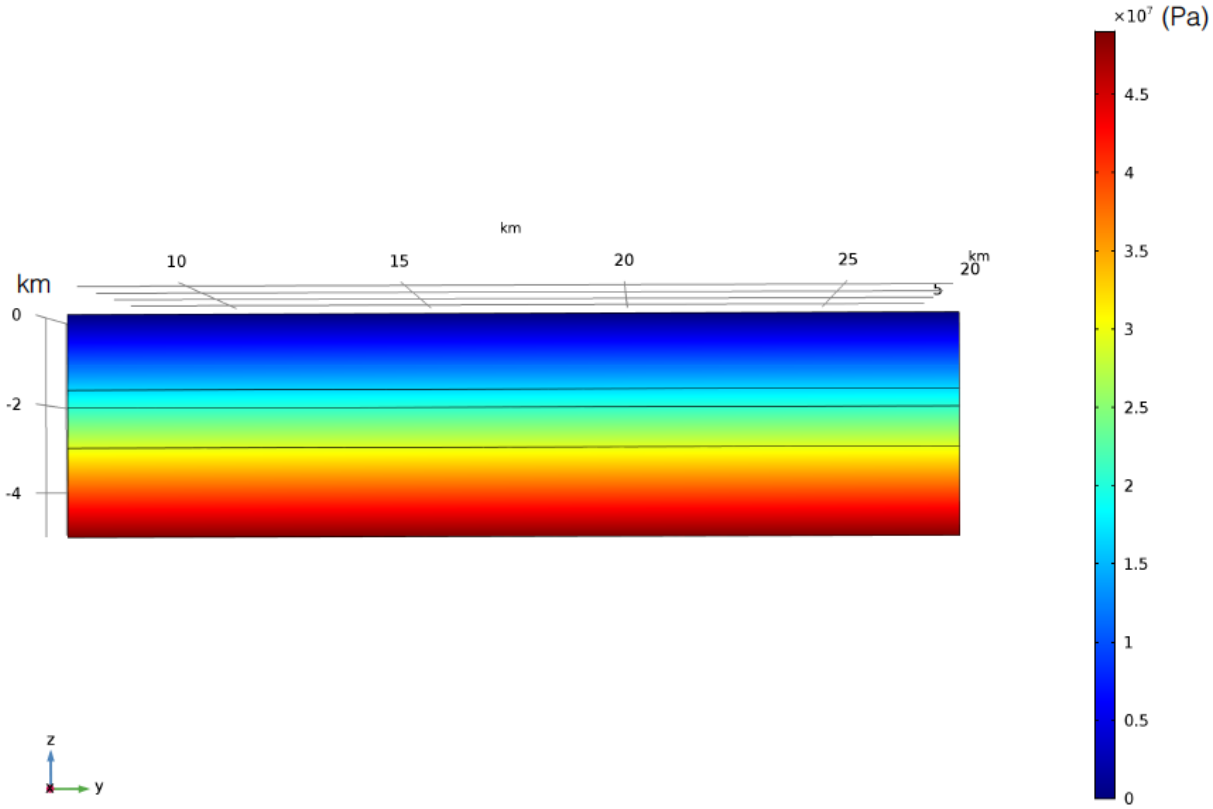

Fig.5.6 The hydro-static pore pressure result for each transient study, which is used as the initial value input for the time-dependent study.

With the boundary and initial conditions, we build three models with different hydrogeological formations (Fig.5.5). In model 1, we only simulate the fluid injection for each

stage without considering any potential fractures or conduits. In model 2, besides the injection points for each HF stage, we assume that the HF operations have created a fracture zone proximate to the horizontal wells, by increasing one order magnitude of permeability compared to shale formation. Finally in model 3, we add a conduit to connect the fracture zone and the pre-existing fault, by setting the conduit a two to three order magnitude of permeability increase to the shale formation, similar to the study of Deng et al. (2016). To simulate the multi-stage fluid injection process, we assume that at each stage, the fluid is injected at a single point that migrates along the well bore with daily injection activity (the location of each injection point is available at BCOGC database), however, we do lack the information on the exact time of when the injection starts for each stage. Hence we assume that the HF operation starts at 8:00 AM each day, and the stages should be done consecutively, but without time overlapping between different stages. The injection rate for each stage of the three wells is shown in Fig.5.7.

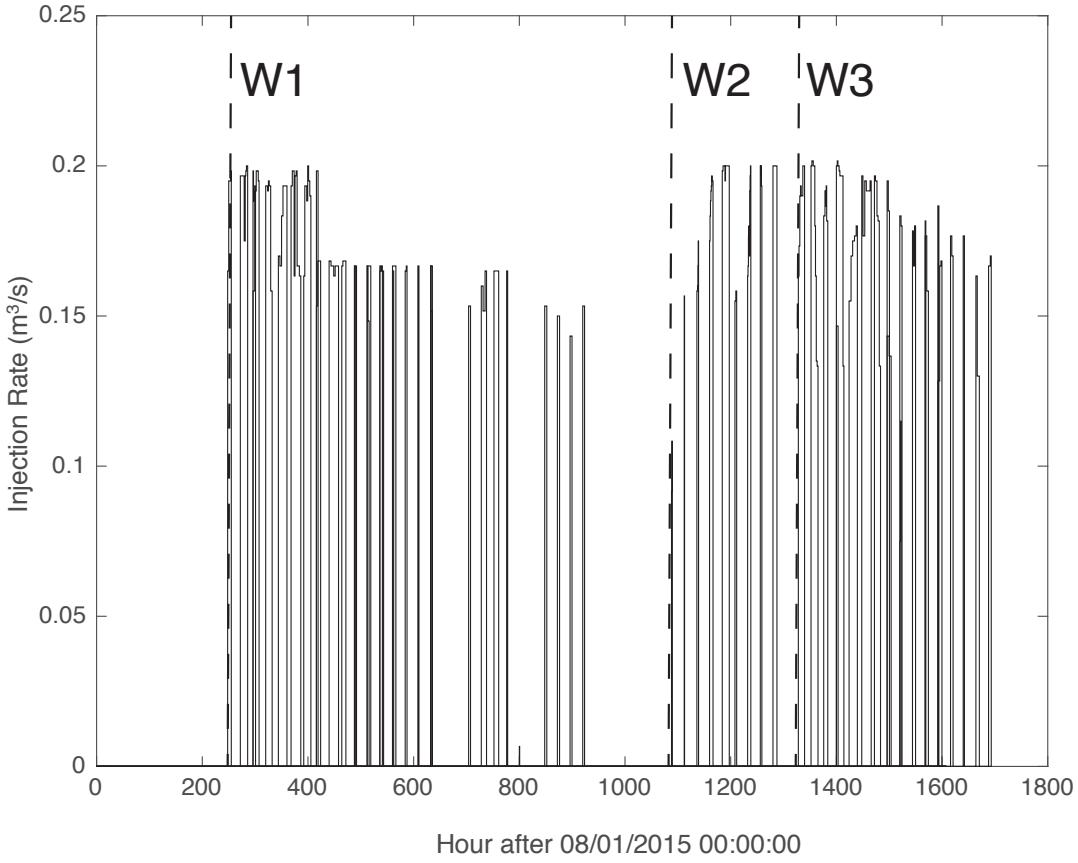

Fig.5.7 Injection rate of each stage for all three HF sites. Vertical dashed lines denotes the commencement of each injection site. Data is available through request from the BCOGC database (https://www.bcogc.ca/elibrary). We assume the injection for each stage in the same day should be operated consecutively.

With above assumptions, after running the models, we obtain the stress tensor and pore pressure change calculated by COMSOL for each time step. We then use the equation below to calculate the ΔCFS resolved on the fault when the nucleation occurs, following the studies of e.g., Xu et al. (2010):

$$\Delta CFS = \sin\lambda\left[-\frac{1}{2}sin^2\phi\, sin(2\delta)\,\sigma^{11} + \frac{1}{2}sin(2\phi)\, sin(2\delta)\,\sigma^{12} + sin\,\phi\, cos(2\delta)\,\sigma^{13} - \frac{1}{2}cos^2\phi\, sin(2\delta)\,\sigma^{22} - cos\phi\, sin(2\delta)\,\sigma^{23} + \frac{1}{2}sin(2\delta)\,\sigma^{33}\right] + cos\lambda\left[-\frac{1}{2}\sin(2\phi)\sin\delta\,\sigma^{11} + \cos(2\phi)\sin\delta\,\sigma^{12} + cos\phi\cos\delta\sigma^{13} + \frac{1}{2}\sin(2\phi)\sin\delta\,\sigma^{22} + sin\phi\cos\delta\sigma^{23}\right] +$$

$$\mu[sin^2\phi sin^2\delta\sigma^{11} - \sin(2\phi)\, sin^2\delta\sigma^{12} - \sin\phi\, \sin(2\delta)\, \sigma^{13} + cos^2\phi sin^2\delta\sigma^{22} +$$

$$cos\phi\, \sin(2\delta)\, \sigma^{23} + cos^2\phi\sigma^{33} + \Delta P] \quad (5.8)$$

where $\mu = 0.6$ is the friction coefficient, ϕ, δ, and λ are the strike, dip, and rake of the receiver fault, respectively, σ^{ij} where $i, j = 1,2,3$ are the components of the stress change tensor in Cartesian coordinate system, and ΔP is the pore pressure change. The ΔCFS and pore pressure change calculated on the hypocenter of the mainshock for the three models are shown in Fig.5.8.

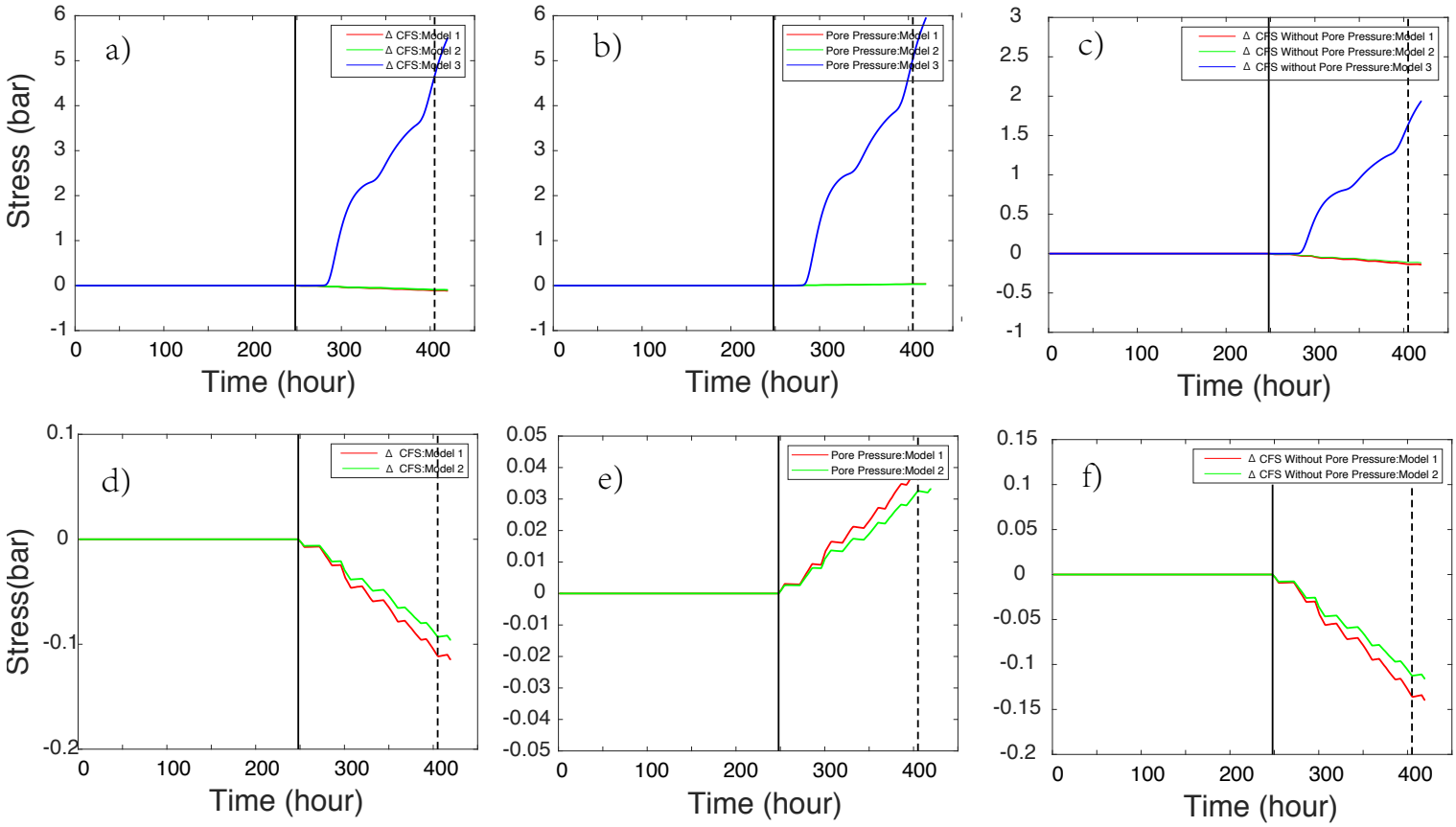

Fig.5.8 Results from the three poroelastic models. Top three panels denote the results for the three models, and bottom ones denote the zoomed in version for model 1 and model 2. a) and d) ΔCFS calculated using Equation 5.1. b) and e) Pore pressure changes only. c) and f) ΔCFS results, calculated with $\Delta CFS = \Delta\tau + \mu\Delta\sigma$, which represent the sole elastic stress perturbation. The solid vertical lines represent the starting time for HF operations, and the dashed vertical lines represent the occurrence time of the M_w 4.6 earthquake.

5.3 Possible mechanism for the immediate triggering (1-day)

After we obtain the ΔCFS results for the M_w 4.6 earthquake, we focus on the immediate seismic response related to the HF operations, here we refer to the 1-day seismic response as immediate triggering at W2 and W3, compared to the 5-day delayed triggering at W1. We follow the methods used in Section 2, where we calculate the ΔCFS imposed by fracture openings and the coupled progression of the elastic stress and pore pressure changes from the injected fluids.

We first calculate the ΔCFS due to fracture opening at W2 and W3 before the injection starts. When we calculate the ΔCFS imposed on receiver faults at W2 and W3, we use the optimal oriented thrust fault based on local stress field as the receiver fault orientation, as we do not have the focal solutions for the earthquakes at these two sites. We also consider the static stress change generated from the M_w 4.6 earthquake, thus the ΔCFS result is the combination of fracture openings and the mainshock (here we only use the M_w 4.6 earthquake for the ΔCFS calculation, due to the lack of focal solutions for the smaller aftershocks). In conclusion, when calculating the static stress change at W2 before the HF starts, we use the fracture openings caused by HF at W1, and for W3, we use the fracture openings at W1 and W2, and both superposed with the static stress perturbation from the M_w 4.6 earthquake.

Next, we use COMSOL to simulate the coupled progression of elastic stress and pore pressure at W2 and W3, following the same steps in Section 5.2, but with a 20 km × 20 km × 5 km scale as shown in Fig.5.9. Here we do not consider the fracture zone around the horizontal wells, as the scale of the fracture zone is much smaller compared to the modeling scale between the two injection sites. We also do not consider the potential conduits between injection sites,

due to the lack of the hydrogeological structure information.

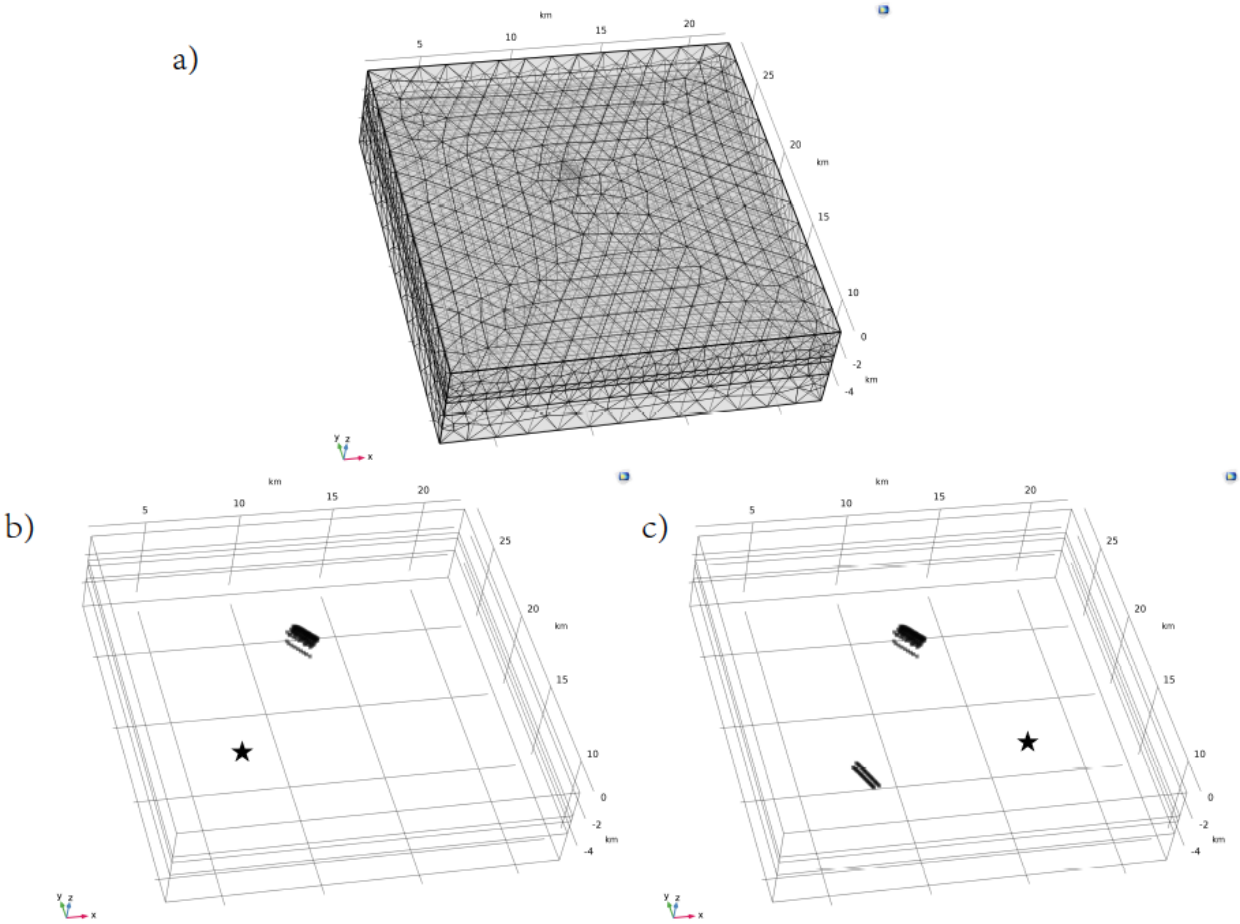

Fig.5.9 The 20 km × 20 km × 5 km models built with COMSOL to simulate the immediate seismic response at W2 and W3. a) The model's meshing scheme, b) the model used for W2, where the black star denotes the reference point for ΔCFS calculation, c) the model used for W3, where the black star denotes the reference point for ΔCFS calculation. The ΔCFS are calculated on the optimally oriented thrust faults at the reference points.

5.4 Discussion

As discussed in Chapter 4, the M_w 4.6 earthquake potentially occurred on a pre-existing fault system, instead of on the newly HF created fractures, the depth calculated from the focal mechanism solutions suggests this pre-existing fault could be within the crystalline basement. We calculate positive ΔCFS (0.02-0.08 bar) imposed by fracture opening on a pre-existing fault

at different depths (Fig.5.4). However, this number is small when compared to the 0.2 bar threshold suggested by previous authors (e.g., Reasenberg and Simpson, 1992; Stein, 1999). In the same time, as shown in Fig.5.8, the ΔCFS results calculated from poroelastic models for model one and model two, both indicate a negative value, which indeed discourage the earthquake from occurring. Instead, results from model three, which contain the simulated conduit, show a much higher ΔCFS value, ~5 bar, and highly encourage faulting. Based on the ΔCFS results from the fracture opening model and the COMSOL numerical models, this M_w 4.6 earthquake on a pre-existing fault is likely to be triggered from fluid migration and pore pressure diffusion through conduits with high permeability, leading to a failure of the pre-existing fault. It is important to note that although the existence of the highly-permeable conduit is by assumption (due to the lack of local seismic reflection data), studies do suggest that the extended faults and associated fracture zones extending from crystalline basement into overlying sedimentary layers may present as permeable pathways connecting the reservoir and Precambrian crystalline basement (e.g., Kozlowska et al., 2018).

Considering models one and two, the small ΔCFS imposed on the receiver fault (albeit the negative values), are caused by the small pore pressure change and poroelastic stress perturbation. The small pore pressure change is due to the low permeability of the shale formation, that it is difficult for the injected fluids to migrate and reach to this pre-existing fault system for a short time period, especially without the conduit-like hydrogeological structure. The small poroelastic stress perturbation is due to the relatively small amount of fluids injected into the shale formation when the M_w 4.6 earthquake occurs, causing less solid deformation. We can not rule out the possibility that the small ΔCFS (< 0.2 bar) from poroelastic stress transfer could

induce tectonic earthquakes even without conduits connecting the injection site and pre-existing fault system, if the pre-existing fault system is at a critically stressed state and preferably oriented. As suggested by other studies, stress perturbation with only several kPa could be enough to trigger local earthquakes from teleseismic events, when using dynamic triggering as a probe (e.g., van der elst et al., 2013; Wang et al., 2015; Wang et al., 2018). But in our case, as the ΔCFS is negative from model one and two, we do prefer the interpretation that the sole poroelastic stress transfer is not the triggering mechanism. Meanwhile, we also note that the errors for the earthquake location could be up to ~3 kilometers on horizontal and vertical directions. This means that we can not dismiss the possibility that even if the conduit does not exist, there is the potential that the pre-existing fault system could be more proximal to the wells or even directly intersect with the HF fracture zone, letting the fluids flow into the fault system much more easily. To test this hypothesis we model this interaction situation shown in Fig.5.10. The pre-existing fault directly cuts through the fracture zone, but without interacting with the horizontal wells. As shown in Fig.5.10, the ΔCFS at the receiver fault is much higher than in the other three models.

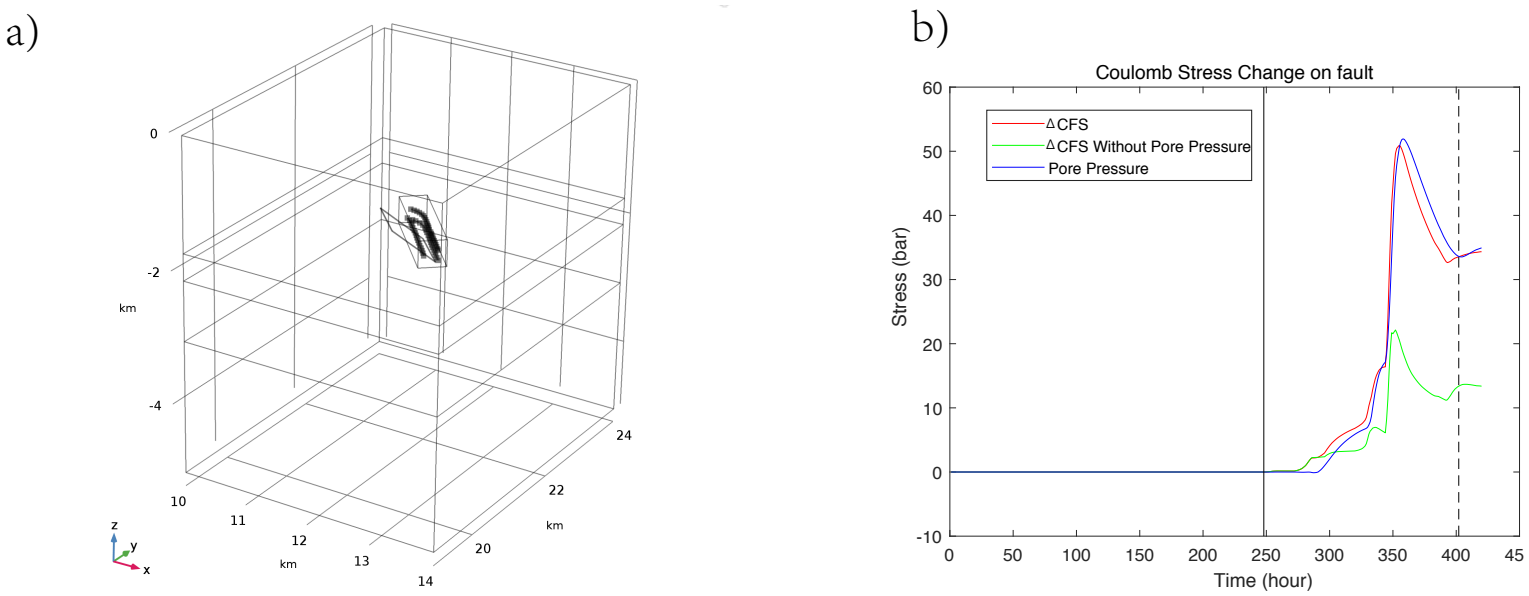

Fig.5.10 a) Model used for simulating the interaction situation between the fracture zone and the fault where the M_w 4.6 earthquake occurs, due to the potential location errors. b) The results for ΔCFS, ΔCFS calculated without pore pressure, and pore pressure are shown in red, green, blue, respectively. Solid line denotes the beginning time of the HF operation and the dashed vertical line denotes the occurrence time of the M_w 4.6 earthquake.

Deng et al. (2016) suggest that the elastic response of the solid matrix could be the dominant factor for earthquakes induced by hydraulic fracturing instead of pore pressure diffusion. However, we do not observe the same phenomenon, i.e., in our case, the elastic pressure perturbations for models one and two are small (even causing negative ΔCFS). There could be several possibilities causing the inconsistences between Deng et al. (2016) and our study. First, the orientation of the receiver fault could act as a important factor, directly related to the amplitude and polarity of ΔCFS as indicated by Equation 5.6 and some other studies (e.g., Segall and Lu, 2015; Lei et al., 2017; Postma and Jansen,2018). Second, we note that in the Deng et al. (2016) model, they do not specify the different layer properties, instead, they assume the horizontal permeability is 5 times larger than the vertical component, while we build a

4-layer model with different solid and fluid properties as shown in Fig.5.5 and Tab.5.1. Third, the injection depth at our study is much shallower than Deng et al. (2016) (1.89 km vs. 3.4 km), and with a less total injected volume for each stage (~1300 m^3 vs. 2700 m^3). Fourth, Deng et al. (2016) calculate the ΔCFS on a reference point shallower than the HF horizontal well as shown in their Fig.2, while we compute the ΔCFS at the nucleation point at 4 km depth, much deeper than the HF horizontal wells, and with a longer distance between the horizontal well and the reference point. All of these factors could contribute to the inconsistency of the results between the different models. In addition, our results also show a simultaneous response between the elastic stress change and pore pressure change as shown in Fig.5.8 and Fig.5.11, this is legitimate as we assume the models are fully coupled, that any solid deformation within the rock matrix should affect the pore pressure, and in turn, the pore pressure will also counter-affect the solid deformation. Finally, if our models one and two do reflect the real subsurface formation, we agree with Deng et al. (2016), that the poroelastic stress perturbation has a larger and immediate effect as the fluid can not reach the fault when the M_w 4.6 earthquake occur.

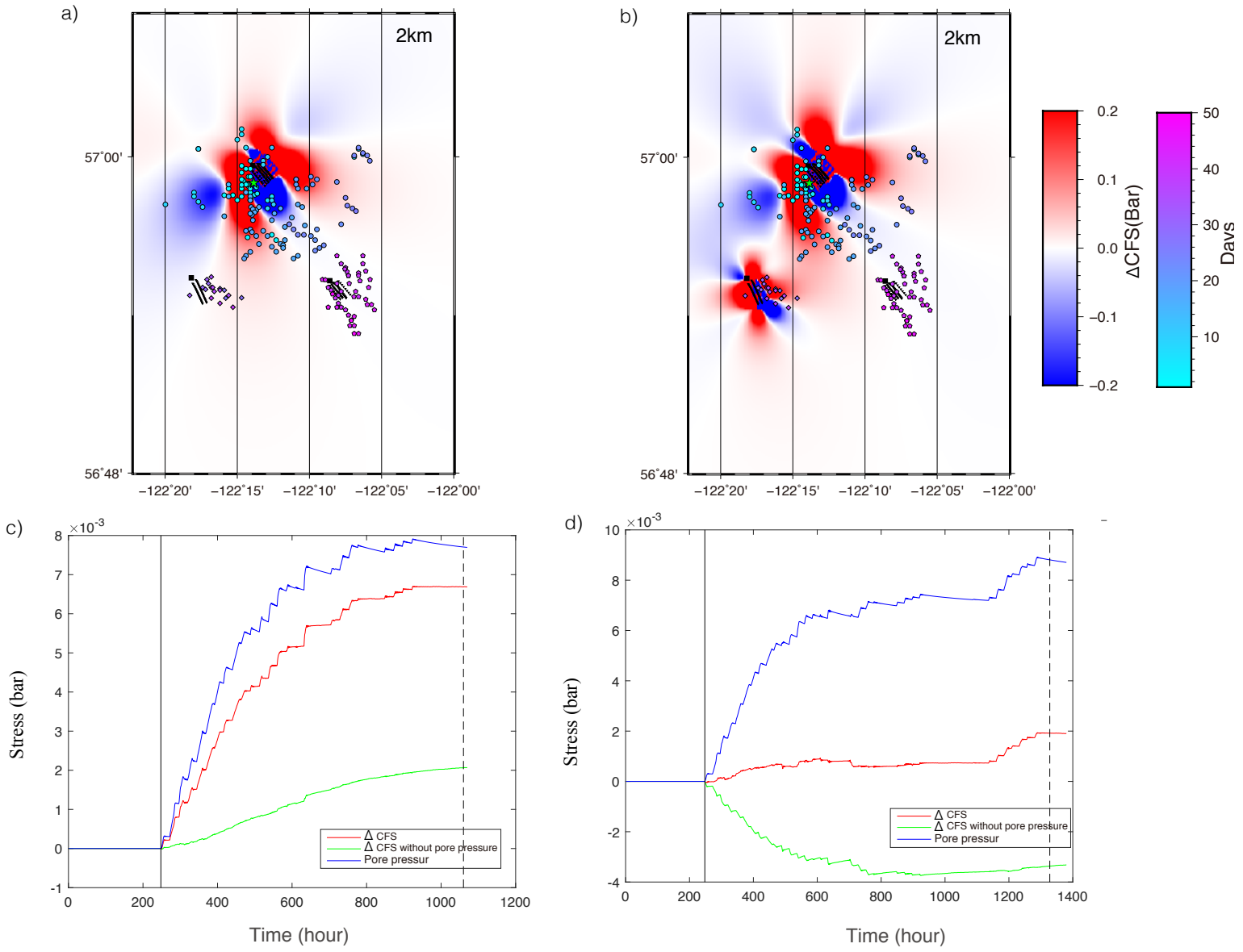

Fig.5.11 The ΔCFS results for the injection sites at W2 and W3. a) and b) the maps of ΔCFS calculated at 2 km depth, resulting from the elastic stress perturbations from the tensile fracture openings before the HF operation starts at W2 and W3, respectively, for the optimally oriented thrust faults. c) and d) denote the ΔCFS results at the reference points shown in Figs.5.8 from the poroelastic model for W2 and W3, respectively, together with the pore pressure change and ΔCFS without pore pressure. The symbols for the seismicity and HF stages are the same as in Fig.5.4.

For the immediate earthquake triggering response at W2 and W3, the static stress change caused by fracture opening together with the M_w 4.6 earthquake at 2 km depth reference points is

around ~0.01 bar, both with positive ΔCFS values as shown in Fig.5.11a and b. ΔCFS calculated on the same reference points but with depth range from 3-5 km are shown in Fig.5.12 and Fig.5.13 (The locations of the reference points are marked in Fig.5.9). ΔCFS for W2 and W3 at the same reference points calculated with the poroelastic model also have positive values as shown in Fig.5.11c and d. After summing the ΔCFS calculated from fracture openings, mainshock, and fluid injections, the positive ΔCFS values (~0.013 bar at W2 and ~0.011 bar at W3) favor the earthquake's occurrence, but note that the values are smaller than the 0.2 bar triggering threshold. Although our model does not include any conduit-like structures to avoid over interpreting the results from numerical models, we can not rule out the possibility that the fluid can diffuse much faster if a complex conduit system does exist between injection sites (e.g., Salah and Zhao (2003) suggest that high crack density may suggest a high-permeability pathway at a tectonic scales, or even a locally fault can act as a permeable pathway (Townsend and Zoback, 2000)), which can significantly increase the fluid migration rate or poroelastic stress transfer.

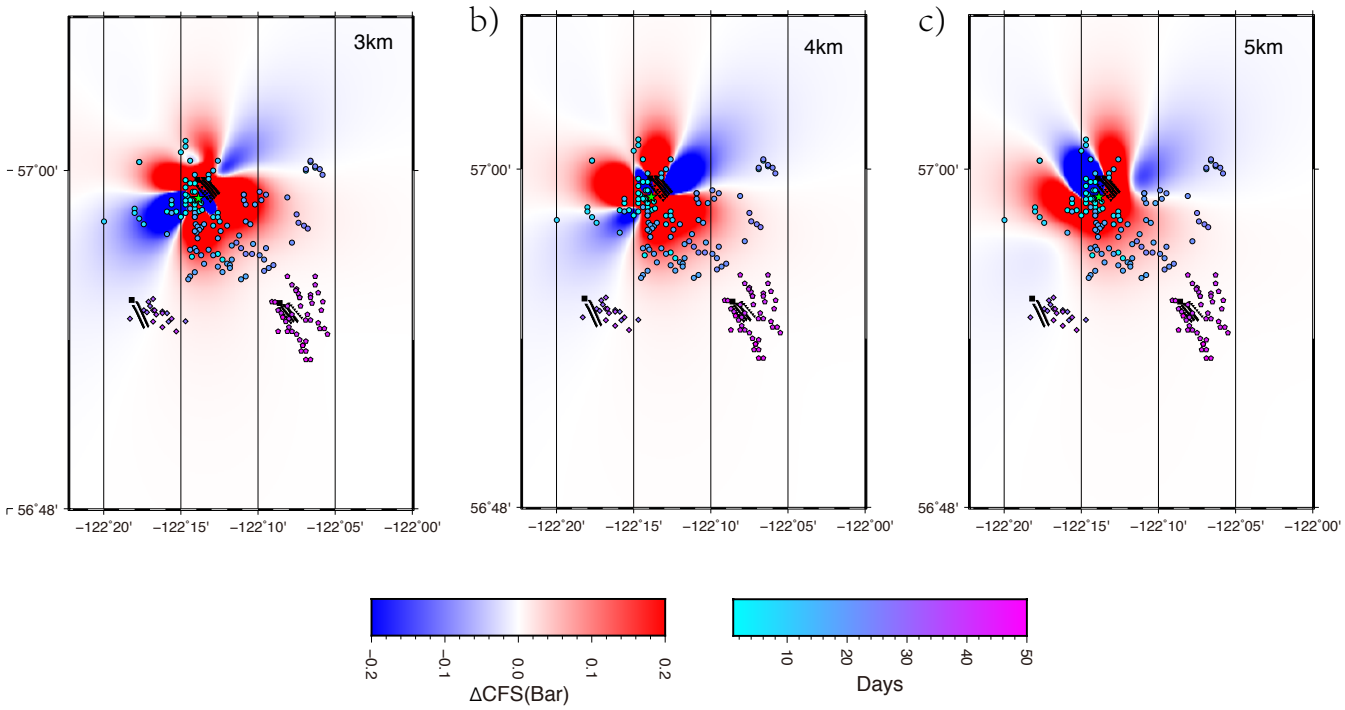

Fig.5.12 The ΔCFS results for the injection site at W2 with the depth range between 3 km and 5 km, calculated from the superposition of the elastic stress perturbations from the M_w 4.6 earthquake and tensile fracture openings before the HF operation starts at W2 for the optimally oriented thrust faults.

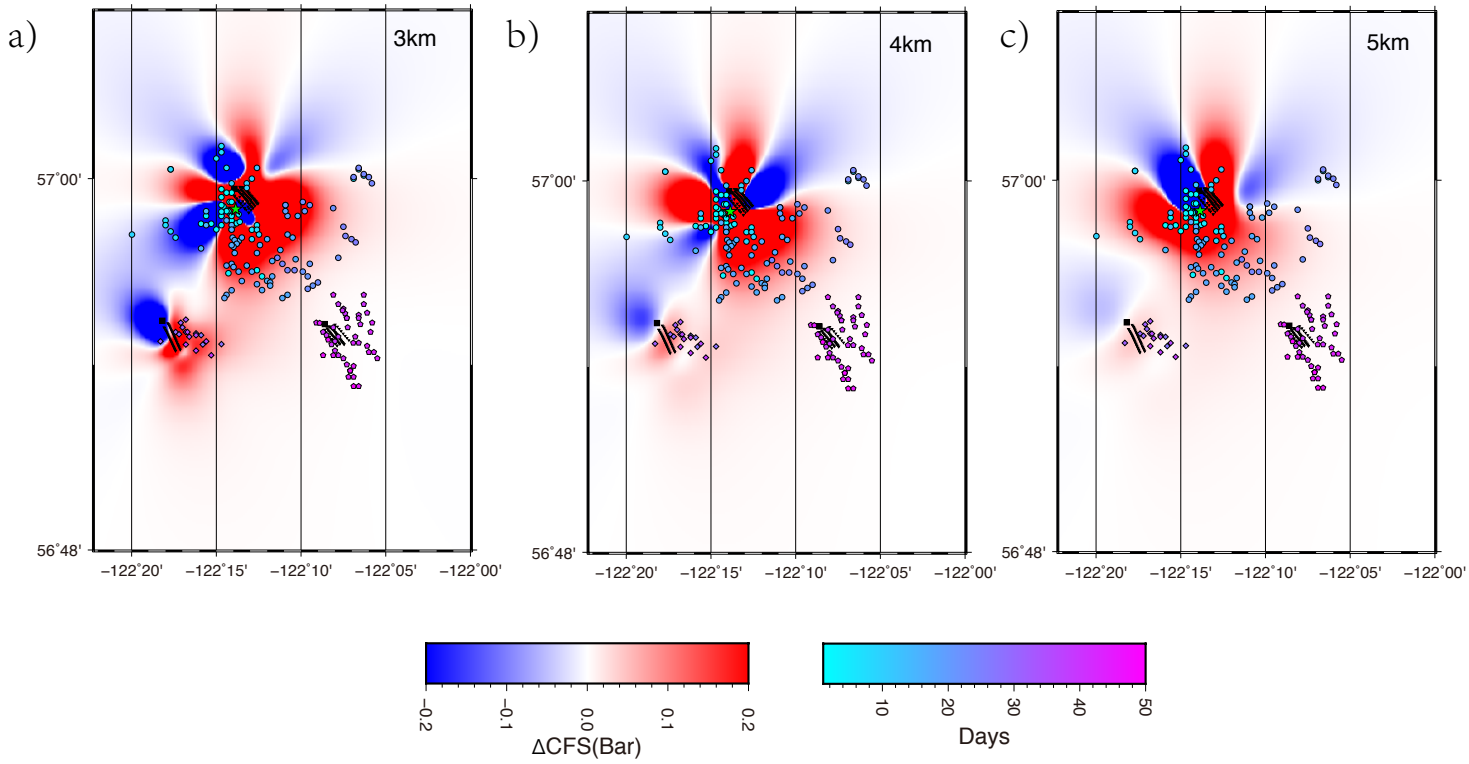

Fig.5.13 The ΔCFS results for the injection site at W3 with the depth range between 3 km and 5

km, calculated from the superposition of the elastic stress perturbations from the M_w 4.6 earthquake and tensile fracture openings before the HF operation starts at W3 for the optimally oriented thrust faults.

To explain the different delays of seismic response to HF injection at different fracturing sites, we need to consider each case separately, but the most fundamental idea is that the stress perturbation should be large enough to exceed the failure criteria. First, the stress gap between current stress state and the failure stress directly determines how large a stress perturbation is required. That is, under the framework of an undrained poroelastic model, a longer injection period/larger volume of injection fluid is able to accumulate a larger stress perturbation (W1 vs. W2 and W3). Second, assuming the initial stress states at the three wells are similar, stress fields at W2 and W3 could be altered by activities at W1, thus facilitating the seismicity response at W2 and W3. Several mechanisms would lead to different levels of stress perturbation, for example, the magnitude and orientation of nearby induced earthquakes result in different static response (in our case, the Coulomb stress change due to the M_w 4.6 thrust earthquake); the distance between the injection sites would not only influence the magnitude of stress perturbations, but also the diffusion time (i.e., the closer the two injection sites, the higher stress perturbation could be imposed by vicinity HF sites, as shown in Fig.5.14, the ΔCFS at midway between W1 and W2 has a larger value), and the possible existence of subsurface hydraulic conduit acting as a pathway could highly increase the fluid flow at a local scale.

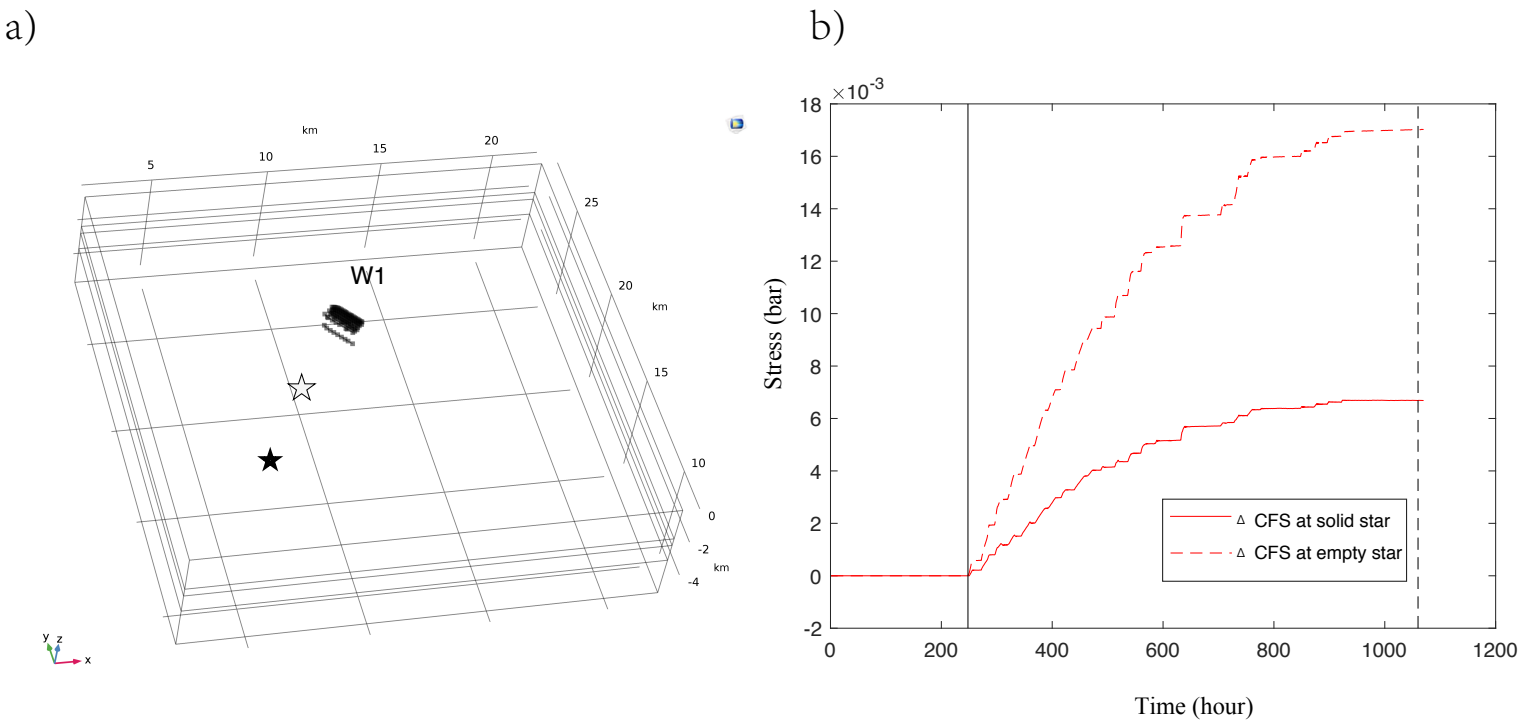

Fig.5.14 ΔCFS calculated for two reference points with different distance to HF sites W1. a) Lines with black dots denote the horizontal wells and HF stages, the stars represent the reference points where ΔCFS is calculated. b) ΔCFS results for the two reference points shown in a), caused by the HF fluid injection at W1.

Finally, we are aware of the fact that even though we have built several numerical models to simulate different hydrogeological structures, the models are still characterized by several oversimplifications. For instance, the size of the fracture zones, the orientation of the fault systems, the initial confined pressure in the shale layer, the tilt angles of different layers, the potential conduit systems, and the earthquake locations. All of these uncertainties could influence the results of the numerical simulations. However, the idealized geological formations used in the numerical simulations could provide some insights into the triggering mechanisms behind some of the observed phenomena. Hence, we believe that a more detailed knowledge of the underground formations could help increase the accuracy of the models.

5.5 Conclusions

In this chapter, we first investigate the triggering mechanisms for the M_w 4.6 earthquake by calculating the ΔCFS on the receiver fault with both a fracture opening model and numerical poroelastic models. The results suggest that pore-fluid pressure diffusion through an hypothetical high permeability conduit could be the most plausible reason for the triggering when compared to the small elastic stress change caused by fracture openings and fluid injection, but we can not rule out the possibility that this elastic stress change could also contribute to the occurrence of this M_w 4.6 earthquake due to the positive ΔCFS values. Then we focus on the immediate seismic response at two injection sites using the same approaches. Positive ΔCFS results do suggest HF activities and earthquakes at nearby injection sites could alter local stress field and encourage the earthquake to occur, thus two factors could contribute to the length of response times between the HF operations and induced earthquakes at different injection sites, 1) the fault's initial stress state, and 2) the stress perturbations generated by external forces.

5.6 References for Chapter 5

Atkinson, G. M., Eaton, D. W., Ghofrani, H., Walker, D., Cheadle, B., Schultz, R., Shcherbakov, R., Tiampo, K., Gu, J., Harrington, R. M., Liu, Y. J., van der Baan, M., & Kao, H. (2016). Hydraulic Fracturing and Seismicity in the Western Canada Sedimentary Basin. *Seismological Research Letters, 87*(3), 631-647. doi: 10.1785/0220150263

Bao, X., & Eaton, D. W. (2016). Fault activation by hydraulic fracturing in western Canada. *Science, 354*(6318), 1406-1409.

Bell, J., & Grasby, S. (2012). The stress regime of the Western Canadian sedimentary basin. *Geofluids, 12*(2), 150-165.

Boroumand, N., & Eaton, D. W. (2015). Energy-based hydraulic fracture numerical simulation: Parameter selection and model validation using microseismicity. *Geophysics, 80*(5), W33-W44.

Clauser, C. (1992). Permeability of crystalline rocks. *Eos, Transactions American Geophysical Union, 73*(21), 233-238.

Cui, X., & Nassichuk, B. (2018). Permeability of the Montney Formation in the Western Canada Sedimentary Basin: insights from different laboratory measurements. *Bulletin of Canadian Petroleum Geology, 66*(2), 394-424.

Deng, K., Liu, Y., & Harrington, R. M. (2016). Poroelastic Stress Triggering of the December 2013 Crooked Lake, Alberta, Induced Seismicity Sequence. *Geophysical Research Letters*, 43, 8482– 8491, . doi: 10.1002/2016GL070421

Dong, T., Harris, N. B., Ayranci, K., Twemlow, C. E., & Nassichuk, B. R. (2017). The impact of composition on pore throat size and permeability in high maturity shales: Middle and Upper Devonian Horn River Group, northeastern British Columbia, Canada. *Marine and Petroleum Geology, 81*, 220-236.

Fairhurst, C. (2013). *Fractures and fracturing: hydraulic fracturing in jointed rock.* Paper presented at the ISRM International Conference for Effective and Sustainable Hydraulic Fracturing.

Goebel, T., Weingarten, M., Chen, X., Haffener, J., & Brodsky, E. (2017). The 2016 M_w 5.1 Fairview, Oklahoma earthquakes: Evidence for long-range poroelastic triggering at >40 km from fluid disposal wells. *Earth and Planetary Science Letters, 472*, 50-61.

Laske, G., Masters, G., Ma, Z., & Pasyanos, M. (2013). *Update on CRUST1. 0—A 1-degree global model of Earth's crust.* 15, Abstract EGU2013-2658 (Paper presented at the EGU).

Leake, S., & Hsieh, P. A. (1995). *Simulation of deformation of sediments from decline of ground-water levels in an aquifer underlain by a bedrock step.* Paper presented at the US Geological Survey Subsidence Interest Group Conference, Proceedings of the Technical Meeting, Las Vegas, Nevada, February 14–16, 1995.

Lin, J., & Stein, R. S. (2004). Stress triggering in thrust and subduction earthquakes and stress interaction between the southern San Andreas and nearby thrust and strike-slip faults. *Journal of Geophysical Research: Solid Earth, 109*(B2). B02303, doi:10.1029/2003JB002607.

Madariaga, R. (1977). Implications of stress-drop models of earthquakes for the inversion of stress drop from seismic observations *Stress in the Earth* (pp. 301-316): Springer.

Neuzil, C. (1994). How permeable are clays and shales? *Water resources research, 30*(2), 145-150.

Reasenberg, P. A., & Simpson, R. W. (1992). Response of regional seismicity to the static stress change produced by the Loma Prieta earthquake. *Science, 255*(5052), 1687-1690. doi: 10.1126/science.255.5052.1687

Rice, J. R., & Cleary, M. P. (1976). Some basic stress diffusion solutions for fluid-saturated elastic porous media with compressible constituents. *Reviews of Geophysics, 14*(2), 227-241.

Rokosh, C., Pawlowicz, J., Berhane, H., Anderson, S., & Beaton, A. (2008). Geochemical and Sedimentological Investigation of Banff and Exshaw Formations for Shale Gas Potential; Initial Results. *Energy Resources Conservation Board, ERCB/AGS Open File Report, 10*, 46.

Rokosh, C. D., Anderson, S. D., Beaton, A. P., Berhane, M., & Pawlowicz, J. (2010). *Geochemical and geological characterization of the Duvernay and Muskwa Formation in Alberta.* Paper presented at the Canadian Unconventional Resources and International Petroleum Conference.

Salah, M. K., & Zhao, D. (2003). 3-D seismic structure of Kii Peninsula in southwest Japan: evidence for slab dehydration in the forearc. *Tectonophysics, 364*(3-4), 191-213.

Schultz, R., Atkinson, G., Eaton, D., Gu, Y., & Kao, H. (2018). Hydraulic fracturing volume is associated with induced earthquake productivity in the Duvernay play. *Science, 359*(6373), 304-308.

Segall, P., & Lu, S. (2015). Injection-induced seismicity: Poroelastic and earthquake nucleation effects. *Journal of Geophysical Research: Solid Earth, 120*(7), 5082-5103.

Shapiro, S., & Dinske, C. (2009). Fluid-induced seismicity: Pressure diffusion and hydraulic fracturing. *Geophysical Prospecting, 57*(2), 301-310.

Stein, R. S. (1999). The role of stress transfer in earthquake occurrence. *Nature, 402*(6762), 605.

Toda, S., Stein, R. S., Richards-Dinger, K., & Bozkurt, S. B. (2005). Forecasting the evolution of seismicity in southern California: Animations built on earthquake stress transfer. *Journal of Geophysical Research: Solid Earth, 110*(B5). B05S16, doi:10.1029/2004JB003415.

Townend, J., & Zoback, M. D. (2000). How faulting keeps the crust strong. *Geology, 28*(5), 399-402.

van der Elst, N. J., Savage, H. M., Keranen, K. M., & Abers, G. A. (2013). Enhanced remote earthquake triggering at fluid-injection sites in the midwestern United States. *Science, 341*(6142), 164-167. doi: 10.1126/science.1238948

Vishkai, M., Wang, J., Wong, R. C., Clarkson, C. R., & Gates, I. D. (2017). Modeling geomechanical properties in the montney formation, Alberta, Canada. *International Journal of Rock Mechanics and Mining Sciences, 96*, 94-105.

Wang, B., Harrington, R. M., Liu, Y., Kao, H., & Yu, H. (2018). Remote Dynamic Triggering of

Earthquakes in Three Unconventional Canadian Hydrocarbon Regions Based on a Multiple-Station Matched-Filter Approach. *Bulletin of the Seismological Society of America, 109*(1), 372-386.

Wang, B., Harrington, R. M., Liu, Y., Yu, H., Carey, A., & Elst, N. J. (2015). Isolated cases of remote dynamic triggering in Canada detected using cataloged earthquakes combined with a matched-filter approach. *Geophysical Research Letters, 42*(13), 5187-5196.

Wang, R., & Kümpel, H.-J. (2003). Poroelasticity: Efficient modeling of strongly coupled, slow deformation processes in a multilayered half-space. *Geophysics, 68*(2), 705-717.

Chapter 6

Conclusions

In this work, we first suggest that several regions in Canada are susceptible to dynamic triggering by searching through NRCan catalog following the occurrences of teleseismic events. These include Vancouver Island, the border of the Yukon and Northwest Territories, western Alberta, western Ontario, and the St. Lawrence paleorift system. The subsequent case studies in Alberta, British Columbia, Northwest Territories, and New Brunswick exhibit that sedimentary basins with fluid injection are susceptible to dynamic triggering, even though these regions may not have historically high seismicity level, indicating the faults in these regions are critically stressed. The findings in the first two chapters do help unraveling parts of the puzzles of dynamic triggering. 1) The stress perturbation needed for dynamic triggering near injection sites could be smaller than 1 kPa, comparable to tidal stresses, while 1 order of magnitude smaller than a 5-10 kPa range as previous studies suggested. 2) Low frequency shaking may be more efficient at triggering earthquakes, which could be possibly explained by the flow-driven mechanism of unclogging of fractures, that is, a low-frequency shaking has a longer cycling period that allows fractures to remain open compared to the quick opening and closure during high frequency shaking. 3) Anthropogenic activities could alter the fault's state to a critically stressed state, or even overcome the influence from the compressional tectonic regime, which has been widely regarded as discouraging the occurrence of dynamic triggering. 4) Regions with longer fluid injection history (thus larger volume of injected fluids) could have both immediate and delayed triggering, compared to

regions with shorter injection history which only have relatively immediate triggering response. The above differences suggest that the mechanisms for immediate versus delayed triggering response could result from stress transfer via the rock matrix and pore pressure perturbations, respectively, and providing a unifying mechanism that explains both types of triggering. In general, dynamic triggering provides us a natural probe that can lead us to a better understanding of the fault's stress state.

Next, after we study the HF induced earthquakes at Montney Basin, BC, several questions brought out in the first chapter could be answered. 1) Based on the spatiotemporal correlations between the 08/17/2015 M_w 4.6 earthquake and HF horizontal wells, the earthquake sequence is mostly induced by HF operations. 2) The static stress drop of these induced earthquakes in BC fall within the range of tectonic events, but relatively smaller than the values for induced earthquakes in other parts of the WCSB. 3) This M_w 4.6 earthquake most likely occurred on a pre-existing fault in the Precambrian basement, after calculating the focal depth, *b*-value and the maximum magnitude relation to the volume of injected fluid. 4) The numerical models suggest that if this pre-existing fault did not intersect directly with the HF fracture zone, a highly-permeable pathway may exist and connect between the fault surface and the fracture zone, elevating the pore-fluid pressure and triggering the earthquake. A sole poroelastic stress transfer has an immediate influence compared to fluid migration, but this elastic stress perturbation is too small to make a robust connection to the triggering mechanism. 5) Two factors contribute to the length of response times between the HF operations and induced earthquakes at different injection sites, 1) the fault's initial stress state, and 2) the stress perturbations generated by external forces.

No matter whether the earthquakes are triggered by teleseismic events, or by anthropogenic activities, they can all be regarded as 'induced' earthquakes; the difference is whether the external driving force is from nature or from human activities. Another difference between a naturally 'induced' earthquake and a human induced earthquake is that human activities can activate both critically stressed faults and faults far from failure with a much wider range of stress perturbations (from kPa to MPa), while the stress perturbation from teleseismic events usually range within several kPa, i.e., a fault far from failure can not be triggered by teleseismic events. But the triggering mechanisms for both phenomena can be explained by the Coulomb Failure criterion, i.e., elevating the pore pressure and shear stress, and decreasing the effective normal stress on the fault surface, thus destabilizing the fault. Why we study these two different phenomena together? As we can treat the dynamic triggering as the fault's stress state indicator, it can help the industry figure out whether the fault system is in a 'dangerous zone' for productions or not, and in an extreme case, if the production has already influenced the fault system. The observation of dynamic triggering can still help the well operators adjust the production strategy, which may help avoid the occurrences of destructive induced earthquakes.

In conclusion, to avoid destructive induced earthquakes, a detailed understanding and interpretation of the subsurface formations is a requirement, and using dynamic triggering as a tool to test the fault's stress state could also help to assess the risks from induced earthquakes. In addition, the collaboration among academic, industry, and regulator communities will be an effective way to elucidate the dominating factors behind the HF-induced earthquakes.